Technische Universität München
Fakultät für Elektrotechnik und Informationstechnik

Investigations on Current Filaments Limiting the Safe-Operating Area of High-Voltage Trench-Insulated-Gate Bipolar Transistors

Christopher Töchterle

Vollständiger Abdruck der von der Fakultät für Elektrotechnik und Informationstechnik der Technischen Universität München zur Erlangung des akademischen Grades eines

Doktors der Naturwissenschaften (Dr. rer. nat.)

genehmigten Dissertation.

Vorsitzender:		Prof. Dr. Alessio Gagliardi
Prüfer der Dissertation:	1.	Prof. Dr. Gerhard Wachutka
	2.	Prof. Dr. Marc Tornow
	3.	Prof. Dr.-Ing. Josef Lutz (TU Chemnitz)

Die Dissertation wurde am 18.11.2020 bei der Technischen Universität München eingereicht und durch die Fakultät für Elektrotechnik und Informationstechnik am 29.01.2022 angenommen.

Investigations on Current Filaments Limiting the Safe-Operating Area of High-Voltage Trench-Insulated-Gate Bipolar Transistors

Christopher Töchterle

Contents

Abstract

Current filaments limiting the safe-operating area of high-voltage trench-insulated-gate bipolar transistors (trench-IGBTs) are investigated in this thesis. These non-linear phenomena can lead to device failure due to the occurrence of latch-up and its subsequent thermal runaway. An improved understanding of the physical processes leading to the formation of current filaments and latch-up during the turn-off process of the device is the prerequisite for enhancing the robustness of the device. It was found that current filaments are inherently three-dimensional phenomena regardless of the chip topography. Therefore, the physical features of current filaments and their relation to device failure as a function of their geometry was investigated in the course of a self-consistent theoretical numerical analysis. Due to the complexity of this problem, a computationally efficient approximation of 3D-filamentation effects that limit the safe-operating area was done which makes use of a two-dimensional mapping of the real-chip geometry to two-dimensional Cartesian as well as cylindrical geometry. Special focus was put on on a quantitatively correct and, hence, predictive description of the initial current density threshold at which device failure occurs during the turn-off process. To this end, numerical calculations using large monolithically integrated IGBT-structures which are large enough to fully comprise current filaments, were conducted. It was found that the latch-up threshold of the device under investigation exhibits a strong dependence on the geometry of the current filament that causes latch-up. This geometry, in turn, derives from the geometry of the simulation structures that are used during the analysis. Using the novel approach presented in this thesis, it is possible to obtain results that are in good agreement with experimental data. Furthermore, the influence of chip-design variations on the safe-operating area with a view to improve the robustness of the device against latch-up were investigated using the same approach. In addition to the transient turn-off simulations, an alternative approach using a series of static characteristics of auxiliary simulation structures that model the filamentary turn-off behaviour was conducted, giving further insights into the physics of current filaments.

Kurzzusammenfassung

In der vorliegenden Arbeit werden Stromfilamente untersucht welche den sicheren Arbeitsbereich von hochvolt trench-IGBTs begrenzen können. Diese nichtlinearen Phänomene können zu einer Zerstörung des Bauteils aufgrund eines Einrastens des parasitären Thyristors mit anschließender thermischer Zerstörung führen. Ein besseres Verständnis jener physikalischen Vorgänge welche die Entstehung von Stromfilamenten und dem Einrasten des Thyristors während des Abschaltvorganges führen bilden die Grundlage für eine Verbesserung der Robustheit des Bauteils. Da Stromfilamente dreidimensionale Phänomene, welche unabhängig von der Topographie des Chips sind, wurde die Abhängigkeit der physikalischen Eigenschaften von Stromfilamenten von deren Geometrie mittels selbstkonsistenten theoretischen numerischen Methoden untersucht. Aufgrund der Komplexität dieses Problems und des großen rechnerischen Aufwandes die die Simulation solcher Phänomene bedeuten würde, wurden Näherungen in Form von zweidimensionalen Abbildungen der realen Struktur auf kartesische- sowie Zylinderkoordinaten durchgeführt. Besonderes Augenmerk lag hierbei auf einer quantitativ korrekten, prädiktiven Beschreibung derjenigen anfänglichen Stromdichte-Schwelle, bei der während des Abschaltvorganges ein Einrasten des parasitären Thyristors auftritt. Hierzu wurden numerische Simulationen von großen, monolithisch-integrierten Strukturen durchgeführt, welche aufgrund ihrer Ausdehnung in der Lage sind, Stromfilamente komplett zu beherbergen. Es wurde gezeigt, dass diese Latch-Up Schwelle stark von der Geometrie des Stromfilamentes abhängig ist, welche wiederum von der in der Simulation verwendeten Symmetrie vorgegeben wird. Mithilfe des neuartigen Ansatzes, welcher in dieser Arbeit beschrieben wird, ist es möglich eine quantitativ gut übereinstimmende Vorhersage mit experimentell ermittelten Werten zu erreichen. Des Weiteren wurde der Einfluss von Variationen der Chip-Geometrie auf den sicheren Arbeitsbereich des Bauteils untersucht. Zusätzlich zu den transienten Simulationen von Abschaltvorgängen wurde ein alternativer Ansatz, welcher auf der Simulation statischer Kennlinien von Hilfstrukturen basiert, durchgeführt. Mit diesem Ansatz ist es möglich, weitere Einblicke in die physikalischen Eigenschaften eines filamentären Stromflusses mit signifikant reduziertem Rechenaufwand zu erlangen.

1. Introduction

The theoretical description of physical phenomena occurring in power semiconductor devices beyond the safe-operating area is the main topic of this thesis. A better understanding of these phenomena along with a physics based simulation environment can help improve the design and thus the performance as well as the robustness of devices. The investigations presented in this thesis focus on high-voltage Insulated-Gate Bipolar Transistors (IGBTs).

Current inhomogeneities during over-current turn-off essentially limit the safe-operating area (SOA) of high-voltage trench-IGBTs because they may lead to device latch-up, i.e. the destruction of the device. The three dimensional cell geometry of the real IGBT chip leads to the formation of three dimensional current filaments. The simulation of the formation, evolution and physical properties of these phenomena poses a challenge, since a full transient, electro-thermally coupled three dimensional simulation is at present limited by hardware as well as software capabilities. Therefore, the generation of simulation structures that approximate the real-chip geometry while still giving a realistic picture of the critical phenomena using a simplified stripe or cylindrical geometry, is needed.

Current filaments are essentially three-dimensional phenomena, independent of the real-cell geometry, which can be either stripe-shaped or chessboard-shaped. For a quantitative analysis of the safe-operating area it is crucial to approximate the real geometry of a current filament itself as closely as possible in order to incorporate as many physical features as possible.

This thesis outlines several methods of approximating the real cell geometry by proposing different simulation symmetries as well as their advantages and shortcomings with respect to a numerical analysis of current filaments and their connection to device latch-up. An improved understanding of the physical processed leading to the formation of current filaments and latch-up in large arrays of monolithically integrated high-voltage trench-IGBT cells during the turn-off process of the device is the prerequisite for enhancing the robustness of the device.

This chapter is structured as follows: a short introduction to structure, working principle and variants of the metal-oxide-semiconductor field-effect transistor (MOSFET) is given, followed by a detailed introduction to the insulated-gate bipolar transistor (IGBT), which is the device of interest of this thesis. Special emphasis is laid on the description of the static current-voltage characteristics as well as the transient turn-off behaviour of the IGBT, as these features form the prerequisites for the analysis of the safe-operating area of the IGBT. The chapter concludes with a summary of the previous research that was conducted in this field.

1.1 The MOSFET

A common device in semiconductor technology is the so-called metal-oxide-semiconductor field-effect transistor (MOSFET). It has the function of an electrical switch and is used in several different applications across a wide voltage and current range and belongs to the class of field-effect transistors. Its basic structure and working principle is always the same as will be shown in the following. The generic structure of a lateral n-channel MOSFET is depicted in Fig. 1.1a along with its three main electrical contacts: source (S), gate (G) and drain (D) with an optional body (B) contact. Between the metal gate contact and the silicon of the device there is an oxide layer, i.e. a layer of electrically insulating material, which gives the device its name.

If the potential difference between the gate and the source contact, U_{GS}, is chosen to be positive, an electric field builds up in a way that electrons move towards the silicon-oxide interface whereas holes move away from it, forming an inversion layer consisting of electrons (in the case of an n-channel MOSFET inside of the p-substrate) where electrons are the minority carriers, just beneath the gate-oxide. This layer is called the MOS-channel and no current flow takes place through the gate-oxide to the metal gate contact due to the insulating oxide layer. In order for the device to conduct electrical current, the potential difference between the source and the drain contact, U_{SD}, has to be positive as well, causing an electrical field which in turn moves the electrons from the source to the drain contact. Additionally, the device does not become conducting unless U_{GS} is above a certain threshold-voltage U_{th} at which the inversion layer is sufficiently strong to conduct electrons. In short, the MOSFET is in the conducting state if both $U_{\mathrm{SD}} > 0$ and $U_{\mathrm{GS}} > U_{\mathrm{th}}$, respectively. Hence, its ability to conduct current between the source and the drain contact I_{D}, which consists entirely of electron current which makes the MOSFET

a so-called unipolar device, can be controlled by varying U_{GS}. The voltage drop U_{SD} is located in the space-charge regions which form around the *pn*-junctions, especially at the drain side. At a certain U_{SD}, the so-called pinch-off voltage, the space-charge region becomes large enough to limit the drain current, thus leading to a saturation of I_D: a further increase of U_{SD} does not lead to an increase of I_D any more. In an analogous way as described up to now, *p*-channel MOSFETs which have an *n*-doped substrate can be realized as well, having an inversion layer and thus a current flow that entirely consists of holes.

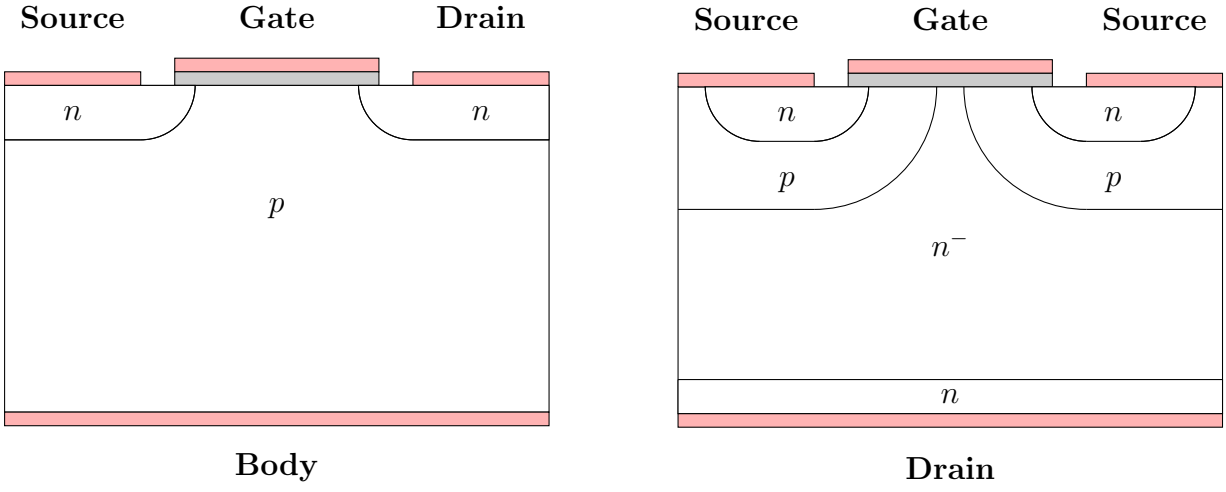

Figure 1.1: Basic structure and doping profile along with electrical contacts (source, gate and drain) of two different types of MOSFETs: (a) *n*-channel lateral MOSFET, (b) *n*-channel vertical MOSFET. The grey colored region indicates the oxide-layer whereas the light-red colored region indicates the electrical contacts (usually consisting of either metal or poly-silicon) [1].

Depending on the field of application, different types of MOSFETs are used. One specialization focusing on power applications, the power-MOSFET, shall be mentioned in the following. A depiction of the basic geometry and doping is depicted in Fig. 1.1b. Contrary to the lateral MOSFET described earlier, the current flow in such a device is located along the vertical direction, however directed from the source to the drain contact. Additional regions with *p*-doping are diffused into such a device, thus leading to the alternative name of double-diffused MOSFET (DMOS), along with an n^--doped base layer. This layer enables the device to sustain the high blocking voltages that are needed in power applications.

If the n-doped region at the drain side of the vertical power MOSFET is replaced by a p-doped region, the resulting device is a so-called insulated-gate bipolar transistor (IGBT). The basic working principle of this device will be described in the following section.

1.2 The Trench-IGBT

In high-power applications the IGBT has several advantages over the power-MOSFET. As already mentioned in the previous section, the IGBT is related to the vertical power-MOSFET and has an additional p-doping at the drain contact as can be seen in Fig. 1.2a, where its basic geometry and doping profile are show along with its three electrical contacts: collector (C), gate (G) and emitter (E). The naming of the contacts is somewhat confusing from a physical point of view as the collector contact is physically an emitter whereas the emitter contact is physically a collector. This originates from the contact names of a *pnp*-bipolar transistor which in combination with an n-channel MOSFET can be viewed as the building blocks of an IGBT. However, the naming as it is introduced at this point is commonly used in literature and will be used consistently throughout this thesis. The emitter contact of the IGBT corresponds to the source contact of the MOSFET whereas the collector contact of the IGBT corresponds to the drain contact of the MOSFET. The gate contact has the same function in both devices, playing the role of the main switching control of the device. However, the gate contact in this case has the shape of a vertical trench along which the MOS-channel is located. This part of the IGBT is commonly referred to as the MOS-part of the IGBT. Due to its applications in high-power devices, the IGBT has to exhibit high blocking capabilities which makes a lowly n^--doped base layer with large vertical extension necessary.
Taking a closer look at the doping profile, a parasitic thyristor, i.e. a *npnp*-structure which is not desired, is part of the IGBT as well. Latching of this thyristor leads to a point at which the current flow through the device can no longer be controlled by the MOS-channel and the entire IGBT is destroyed due to thermal runaway. In order to impede latching of the thyristor, the *pn*-junction between source and body is shorted rather effectively due to the design of the emitter contact and, additionally, a p^+-doping is located directly beneath the emitter contact. As with MOSFETs, several different types of IGBTs can be distinguished. For simplicity, only the IGBT which is investigated in this thesis will be described, i.e. a normally-off n-channel field-stop non-punch-through vertical high-voltage trench-IGBT as depicted in Fig. 1.2b.

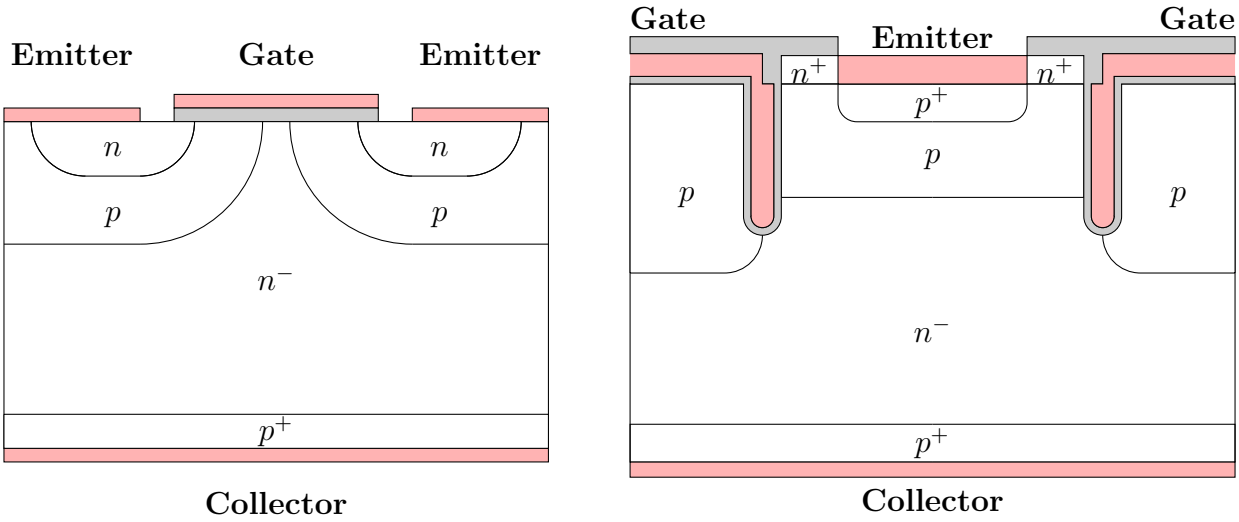

Figure 1.2: Basic structure and doping profile along with electrical contacts (source, gate and drain) of two different types of IGBTs: (a) n-channel planar IGBT, (b) n-channel trench-IGBT. The grey coloured region indicates the oxide-layer whereas the light-red coloured region indicates the electrical contacts (usually consisting of either metal or poly-silicon)

1.3 Static Current-Voltage Characteristics

In this section the dependence of the current through the device as a function of the applied voltages at the three different electrical contacts is described, i.e. a characterization of the static behaviour of a trench-IGBT by means of its current-voltage characteristics. As qualitative and quantitative aspects, respectively, play a crucial role in the characterization, the description of the behaviour is done for a single trench-IGBT chip which has a nominal current of 62.5A, a blocking voltage of 3.3kV, and a total active area of approximately 1cm^2 (thus the nominal current density j_{nom} amounts to 62.5A/cm^2). Such a chip consists of several thousand single cells, which are physically connected in parallel, i.e. monolithically integrated. However, the basic principle of operation can be reduced to a single cell as it is depicted in Fig. 1.2b.

For the IGBT to be conducting, the gate-emitter voltage U_{GE} has to be high enough to create an inversion layer at the interface between gate-oxide and silicon. This is where the MOS-channel, just as in the case of a MOSFET, is located. The inversion is high

enough if U_{GE} is larger or equal the threshold-voltage U_{th} and only in this case electrons can transit the MOS-channel and reach the base layer. Additionally, the collector-emitter voltage U_{CE} has to be positive and larger than the sum of the voltage drops at the *pn*-junction between *p*-emitter and n^--base, the voltage-drop inside of the MOS-channel and the voltage-drop inside of the base layer, which in turn strongly depends on the carrier concentration there. Only if these conditions on U_{GE} and U_{CE} are fulfilled, electrons can be injected into the device and move, according to the potential difference between emitter and collector contact, towards the back-side of the device, i.e. the collector-side, resulting in an injection of holes. These holes move from the back-side of the device across the reverse-biased *pn*-junction between body and drift region towards the front side, i.e. the emitter-side, making the IGBT a so-called bipolar device. Technically, the direction of current flow is from the collector to the emitter-side.

Inside the lowly-doped base layer, even a small amount of electrons drives the base into high injection which along with the injection of back-side holes leads to the formation of an electron-hole plasma. As a consequence, the conductivity rises and thus resistance and the voltage drop there decrease. This effect is often referred to as conductivity modulation and accounts for the low on-state losses during IGBT operation. As will be shown later on, the extraction of this electron-hole plasma can lead to difficulties during the turn-off process.

An increase of U_{CE} to larger positive values widens the space-charge region at the *pn*-junction between base and base layer, which in turn influences the inversion layer in the MOS-channel for high enough values of U_{CE}, leading to a pinch-off of the channel and a saturation of the electron current which can pass through. The result of this effect can be observed in the static current-voltage characteristics, the so-called output characteristics (Fig. 1.3a). This basically gives the collector-current as a function of the applied gate-emitter voltage, i.e. $I_{\mathrm{C}}(U_{\mathrm{CE}})$, at a fixed value for U_{GE} which in turn is above the threshold-voltage.

Additionally, another current-voltage characteristic, the so-called transfer characteristic (Fig. 1.3b) can be determined, which is especially useful for the determination of U_{th}. This characteristic gives $I_{\mathrm{C}}(U_{\mathrm{GE}})$ at a fixed value for U_{CE}.

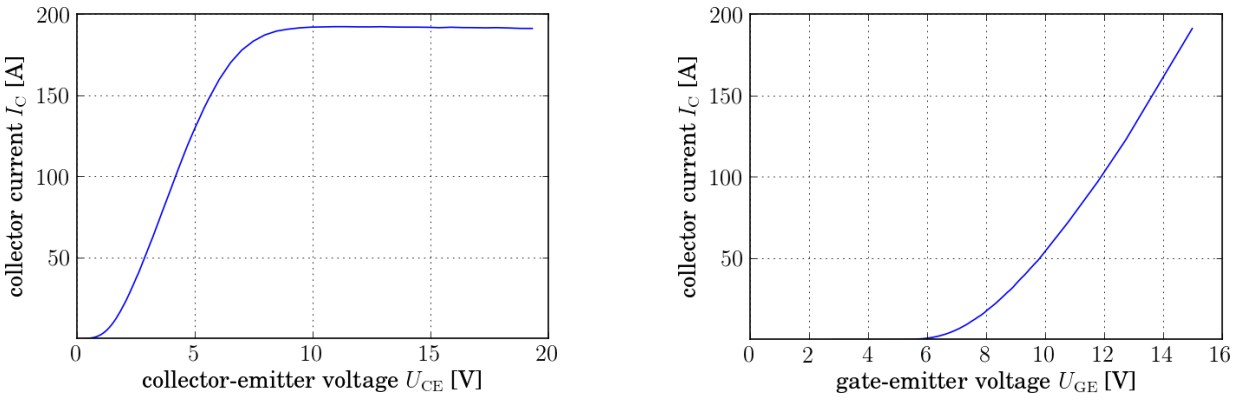

Figure 1.3: Measurement of static IGBT-characteristics at a homogeneous lattice temperature of 150°C. (a) IGBT output characteristics $I_C(U_{CE})$ at a fixed value for U_{GE} of 15V. (b) IGBT transfer characteristics $I_C(U_{GE})$ at a fixed value for U_{CE} of 20V.

1.4 Transient Characteristics: IGBT Turn-Off

As the destruction mechanism which is investigated in this thesis occurs during the turn-off process, a detailed physical description of the temporal behaviour of an IGBT is presented in this section. Device turn-off is described for a single simulation structure for a turn-off process within the safe-operating area, i.e. within the specified ratings of the device. This can be done since under such conditions each cell within the chip behaves the same and no phenomena with a lateral extension higher than the lateral extension of a single cell is present in the device. (This is no longer true for critical phenomena such as current filaments which potentially limit the safe-operating area and which are investigated in detail in this thesis in chapters 5 to 8.) The electrical circuit used for a turn-off process with inductive load is depicted in Fig. 1.4a, where along with the IGBT itself and the freewheeling diode D_F the DC-link voltage $U_{DC\text{-}link}$, the load current I_{load}, the stray-inductance L_σ and the gate resistance R_G a switch is visible. The turn-off process is triggered by a switch of the gate voltage from $U_{G,on} = 15V$ to $U_{G,off} = -15V$. Throughout this thesis, this switching will mark the initial time $t_0 = 0$, i.e. the beginning of the turn-off process.
At the beginning of turn-off, the IGBT is in the on-state, conducting the load current I_{load} which from a simulation point of view is a parameter which can be varied, especially such that the specified ratings are surpassed in the case of an over-current turn-off simulation. Initially, the current density distribution as well as the lattice temperature distribution

are homogeneous, the lattice temperature initially being at 423K across the entire device, which is the usual operating temperature of the device. Values for parameters such as stray-inductance and gate-resistance are determined by calibration (cf. chapter 3) according to measured data.
The transient behaviour of physical quantities such as $U_{\mathrm{GE}}(t)$, $I_{\mathrm{C}}(t)$ and $U_{\mathrm{CE}}(t)$ during the turn-off process determined by measurement are depicted in Figs. 3.3a, 3.3b and 3.4a. In the following, the physical processes leading to this behaviour will be described in chronological order.
As has already been mentioned, at $t = 0$ the IGBT is in the on-state, conducting the load current I_{load} when the switch from $U_{\mathrm{G,on}}$ to $U_{\mathrm{G,off}}$ is triggered. The collector-emitter voltage U_{CE} is low whereas the collector current I_{C} is at its maximum value. A discharging of the gate through the gate-resistance R_{G} takes place (the smaller the resistance, the faster the discharging) and hence U_{GE} decreases steadily (roughly exponentially where the time constant depends on the gate-collector capacitance C_{GC}). Decreasing U_{GE} leads to a decrease in the number of electrons which pass through the MOS-channel, i.e. a smaller number of electrons is injected into the device. The inductive load L_σ causes more holes to be extracted from the base layer in order to maintain the collector current I_{C}, thus carrier concentration in the base layer decreases.
The charge concentration at the *pn*-junction between base and base layer drops to zero followed by the formation of a space-charge region and thus an increase in U_{CE}. This process continues until U_{CE} reaches the DC-link voltage $U_{\mathrm{DC\text{-}link}}$, where the space-charge region cannot expand any more and I_{C} starts to decrease. The negative rate of change of I_{C} with respect to time induces a negative voltage in L_σ which leads to a forward-biasing of the freewheeling diode D_{F} which then starts to take the current. This in turn causes an overshoot voltage in U_{CE} (cf. Fig. 3.4a) which then leads to a further decrease in carrier concentration inside of the device until no free carriers are left and thus the device is turned-off. At the end of the turn-off process, $U_{\mathrm{CE}} = U_{\mathrm{DC\text{-}link}}$, $U_{\mathrm{GE}} = U_{\mathrm{G,off}}$ and, of course, $I_{\mathrm{C}} = 0$.
As can be seen from these physical processes, the IGBT turn-off process consists to a significant part of extracting the free carriers from the base layer. On the one hand, this process consumes a rather large amount of time which limits the IGBT's switching frequency. On the other hand, due to the high electric fields especially at the trench-bottoms phenomena such as current filamentation and latch-up may appear. These peaks in electric field strength increase in magnitude with higher initial current densities.

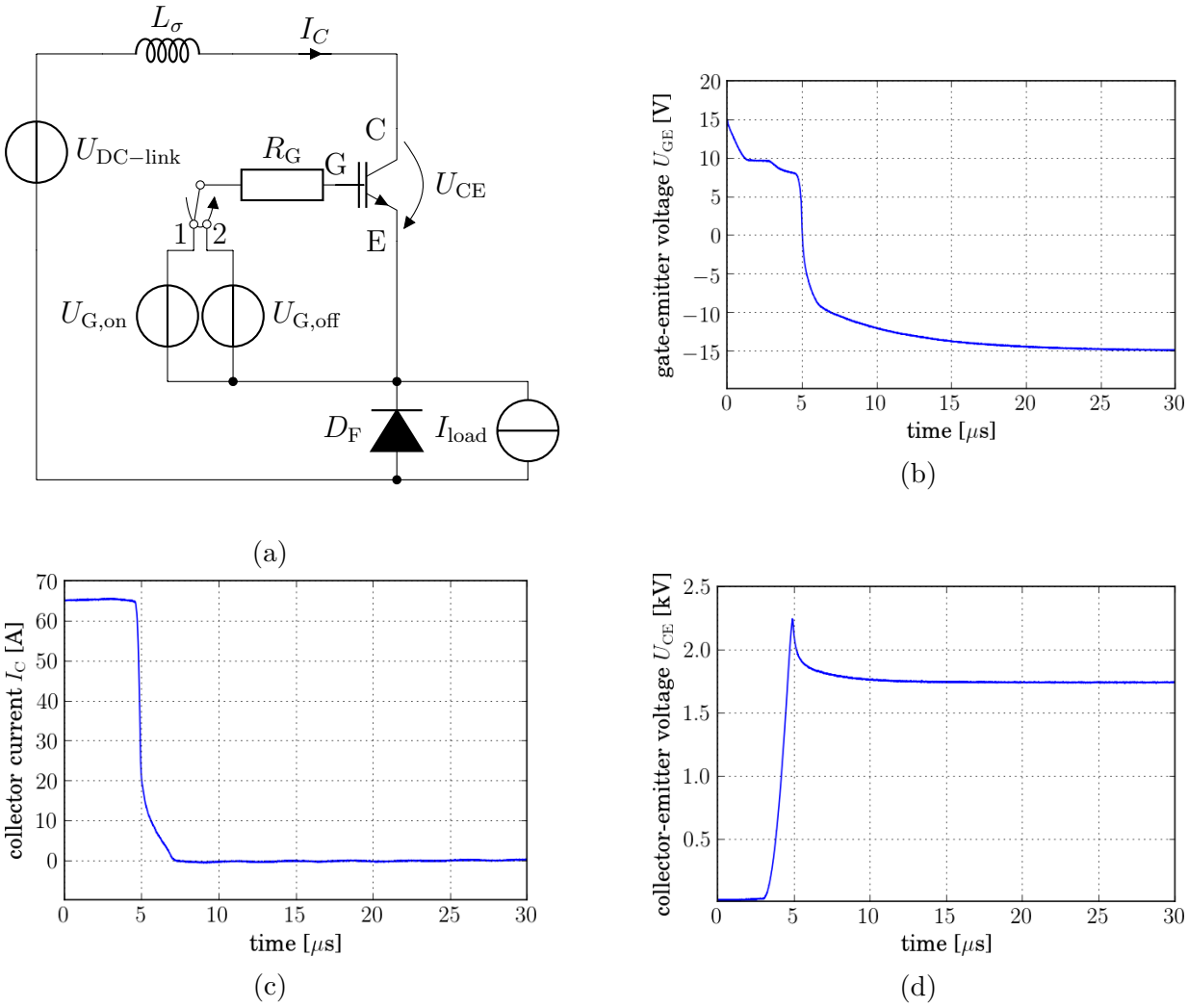

Figure 1.4: Measurement of transient curves during the turn-off process according to the circuit depicted in (a) for an initially homogeneous lattice temperature of 150 °C. The gate-resistance in this case amounts to 100 Ω. (b) The gate-emitter voltage U_GE as a function of time. The turn-off itself is defined as the switch from $U_{\mathrm{G,on}} = 15\mathrm{V}$ to $U_{\mathrm{G,off}} = -15\mathrm{V}$, as can be seen in this diagram. (c) The collector current I_C as a function of time during the same turn-off process. The initial current in this case amounts to the nominal current of a single IGBT-chip of 62.5A. (c) The collector-emitter voltage U_CE. The DC-link voltage in this case amounted to $U_{\text{DC-link}}$=1.8kV. [2]

1.5 Device Latch-Up

Latch-up of the IGBT is the main failure mechanism which is investigated in this thesis as it fundamentally limits its safe-operating area with respect to over-current turn-off capability. It can occur in every IGBT as a *npnp*-structure, the so-called parasitic thyristor, is always contained inside of the device and is thus not restricted to a certain IGBT-design such as trench-IGBTs, as can be seen in Figs. 1.2. The term latching/latch-up derives from the thyristor where it is used synonymously for the turn-on of the device. In the following, the physical processes inside an IGBT which lead to latch-up are described.
As was already described in the previous section, at a certain point during the turn-off process the gate-emitter voltage falls below the threshold voltage which leads to a closing of the MOS-channel, an extraction of carriers from the plasma and a build-up of a space-charge region, which leads to electric fields. During this process, a potentially high concentration of holes can be located at the emitter side, especially when an extraction of holes from the plasma towards the emitter contact takes place. The emitter contact itself is designed such that the *pn*-junction between source and body is shorted rather effectively (see Fig. 1.2b) and thus only a low voltage drop exists there. In case of an excessive amount of holes moving towards the emitter contact beneath this *pn*-junction, the voltage drop caused by the holes can be high enough to produce a forward biasing of this junction, i.e. electrons are injected into the device despite the fact that the MOS-channel is closed. The injection takes place only if a threshold in hole current density at the emitter side, is surpassed. As this happens during turn-off, the collector-emitter voltage at this point in time is still high so that the electrons can enter the device and cause a further injection of holes from the back-side of the device. If the amount of injected electrons is high enough it can cause the parasitic thyristor inside of the IGBT to latch, i.e. the parasitic thyristor is turned-on and the current flow through the IGBT can no longer be controlled by the gate-emitter voltage. Due to the high injection of electrons and, accordingly, the back-side injection of holes, the current rises steeply and the electric field at the front side of the device breaks down, i.e. a plasma channel forms in vertical direction. The high current densities lead to a steep increase in lattice temperature until the IGBT is thermally destructed. Latch-up of the IGBT always leads to a destruction of the device.
High initial current densities favour device latch-up during the turn-off process which derives from the fact that a larger amount of carriers are present inside of the base layer.

Also high temperatures and a fast device turn-off due to, i.e. small gate resistances, facilitate latch-up. Especially locally increased current densities at the front side of the device, as in the case of a current filament, can lead to latching of the parasitic thyristor, as will be discussed in detail in chapters 5 and 6. In order to reduce the possibility of latch-up within a chip, several design measures can be employed such as a short lateral extension of the n-source as well as an additional p^+-doping underneath contact hole (cf. Fig. 1.2b). In any case, device latch-up fundamentally limits the safe-operating area of the IGBT, which will be discussed in the following section.

1.6 The Safe-Operating Area

The safe-operating area (SOA), as it is treated in this thesis, is investigated with regard to over-current turn-off capability (cf. [2]). More specifically, the goal is to find the threshold in initial current density at which latch-up occurs at some point during the turn-off process. The SOA is a much wider field, as device failure can be restricted by other means such as over-heating, over-voltage, short-circuit, avalanche breakdown, cosmic radiation or several degradation effects as well. These scenarios, however, are not considered in this thesis as they were not subject of interest in this research.
More specifically, the analysis of the SOA is based on a single IGBT-chip only (an entire module may consists of 24 IGBT-chips which are connected in parallel) and thus does not incorporate possible destructive effects between different chips. On the chip itself, only cells that lie inside of the active area are investigated, i.e. no edge termination cells are considered. This is based on the device-specific experimental evidence that only non-edge termination cells run into the latch-up state during an over-current turn-off situation and that the exact location of a failure is distributed randomly across all these cells for a series of experiments. Latch-up of a single cell is synonymous for the destruction of the entire chip, the thermal destruction of the device being the main cause of failure. Even small differences in the fabrication process and the positions of the cells within the chip themselves lead to asymmetries, causing no two cells to behave exactly the same during the turn-off process. These differences can trigger a filamentary current flow, which becomes relevant during the turn-off process, as the SOA can be significantly limited when the current density distribution inside of the chip is inhomogeneous: the more inhomogeneous, the lower the threshold in initial current density for latch-up and, hence, the more restricted the SOA.

Quantitatively speaking, an exact prediction of the limits of the SOA along with an understanding of the qualitative physical processed leading to device failure are desirable in the development and improvement of power semiconductors. As requirements to IGBTs increase, the nominal current densities increase and filamentary behaviour of the device becomes more likely.

1.7 Previous Research on Current Instabilities in High-Voltage IGBTs

Previous research carried out in the field of current instabilities and restrictions to the safe-operating area in high-voltage IGBTs with respect to over-current turn-off include the PhD. theses by P. Rose [3], S. Milady [4] and A. Müller-Dauch [5] and the publications derived from them. These investigations, however, only partially use IGBTs with a trench-structure and additionally use IGBTs with lower blocking voltages as well, which stands in contrast to the present thesis. However, the main results deriving from these works can be used and applied to the structures in this work as well. Other research in this field to be mentioned here include [6, 7, 8].

2. Physical Models

In this chapter, a brief description of the physical models that were used for the device simulations is given. Emphasis is laid upon a physics-based modelling of the effects which occur in the device simulation, especially at the rim of the safe-operating area and beyond, where potentially destructive processes set in.
This chapter is structured as follows: the fundamental equations which describe the carrier transport due to drift- and diffusion processes inside of the device are given along with the continuity equations for both electrons and holes, respectively. Additionally, the physical models which describe the physical quantities within the drift-diffusion equations are given: these encompass processes of carrier generation and recombination, respectively, carrier mobility models, models describing bandgap narrowing as well as thermodynamic models which are needed in treating the lattice temperature as a dynamic variable. A good overview over these models is given in [9, 10], along with the original publications which are referenced in the respective sections. The main source of information on the physical models that are implemented in the software is the Sentaurus SDevice User Manual [11].

2.1 Fundamental Equations

Current transport in semiconductor devices arises due to drift and diffusion processes, both having gradients of physical quantities as their driving force: drift processes are caused by a gradient of the quasi-Fermi potential (i.e. the electric field as driving force) whereas diffusion processes arise due to a gradient in carrier concentration (i.e. a gradient in electron and/or hole concentration as driving force). The current transport itself is described by the electrical current densities of the respective carriers as a function of the

two respective driving forces in the so-called drift diffusion equations which are given by

$$\mathbf{j}_\mathrm{n} = -e_0 n \mu_\mathrm{n} \nabla\phi + k_\mathrm{B} T \mu_\mathrm{n} \nabla n \tag{2.1a}$$

$$\mathbf{j}_\mathrm{p} = -e_0 p \mu_\mathrm{p} \nabla\phi - k_\mathrm{B} T \mu_\mathrm{p} \nabla p \tag{2.1b}$$

with the electron (hole) density n (p), the electron (hole) mobility μ_n (μ_p), the quasi-Fermi potential ϕ and the lattice temperature T. These are accompanied by the elementary charge $e_0 = 1.602 \cdot 10^{-19}\mathrm{C}$ and the Boltzmann constant $k_\mathrm{B} = 1.381 \cdot 10^{-23}\mathrm{J/K}$ as fundamental physical constants. (The values of the physical constants were taken from [12]).
In addition to these two equations, the continuity equations for electrons and holes, respectively, are needed for the theoretical description of current transport in order to account for charge conservation and processes of carrier generation and recombination. These continuity equations are given by

$$\frac{\partial}{\partial t} n = \frac{1}{e_0} \nabla \cdot \mathbf{j}_\mathrm{n} + G_\mathrm{n} - R_\mathrm{n} + \frac{\partial}{\partial t} N_\mathrm{D}^+ \tag{2.2a}$$

$$\frac{\partial}{\partial t} p = -\frac{1}{e_0} \nabla \cdot \mathbf{j}_\mathrm{p} + G_\mathrm{p} - R_\mathrm{p} + \frac{\partial}{\partial t} N_\mathrm{A}^- \tag{2.2b}$$

with the carrier generation rate G_ν, the carrier recombination rate R_ν as well as the donor concentration N_D^+ and the acceptor concentration N_A^-. (Since in this thesis an initially homogeneous lattice temperature of 150°C or 423K in silicon is considered throughout, complete ionisation of these impurities can be assumed. Hence the last terms in equations 2.2 can be neglected.) In literature equations 2.1 are often re-written to include the diffusion constants D_ν using the Einstein-relations

$$D_\nu \equiv \frac{k_\mathrm{B} T \mu_\nu}{e_0} \tag{2.3}$$

with $\nu = \mathrm{n}$ for electrons and $\nu = \mathrm{p}$ for holes.

2.2 Carrier Generation and Recombination Models

This section gives a description of the physical processes considered in this thesis, that lead to carrier generation G_ν or recombination R_ν rates which enter the continuity equations (cf. Eqs. 2.2). It aims at presenting the fundamental physical dependencies as they enter the numeric calculations alongside the references of the original publications, on which this

introduction is based.

2.2.1 Auger Recombination

In regions inside of an IGBT exhibiting a high concentration of impurities, phonon-assisted band-to-band and trap-assisted Auger recombination can occur [13, 14, 15]. Trap-assisted Auger recombination processes can encompass four transitions if a two band model is assumed: recombination with excitation of a high-energy electron, recombination with excitation of a high-energy hole, generation by de-excitation of a high-energy electron, generation by de-excitation of a high-energy hole. The net Auger recombination rate $R^{\mathrm{net}}_{\mathrm{Auger}}$ is given by

$$R^{\mathrm{net}}_{\mathrm{Auger}}(T) = \left[C_{\mathrm{n}}(T)\cdot n + C_{\mathrm{p}}(T)\cdot p\right]\cdot\left[np - n^2_{\mathrm{i,eff}}(T)\right] \tag{2.4}$$

with temperature-dependent Auger coefficients

$$C_\nu(T) = \left[A_{\mathrm{A},\nu} + B_{\mathrm{A},\nu}\left(\frac{T}{300K}\right) + C_{\mathrm{A},\nu}\left(\frac{T}{300K}\right)^2\right]\cdot\left[1 + H_{\mathrm{A},\nu}\cdot\exp\left(-\frac{\nu}{N_{0,\nu}}\right)\right] \tag{2.5}$$

and the effective intrinsic density (i.e. the intrinsic density including effects of bandgap narrowing, cf. section 2.4)

$$n_{\mathrm{i,eff}}(T) = n_{\mathrm{i}}\cdot\exp\left(\frac{E_{\mathrm{G,BGN}}}{2k_{\mathrm{B}}T}\right) \tag{2.6}$$

parameter	$\nu = \mathrm{n}$	$\nu = \mathrm{p}$	unit
$A_{\mathrm{A},\nu}$	$6.7\cdot10^{-32}$	$7.2\cdot10^{-32}$	$\mathrm{cm^6{\cdot}s^{-1}}$
$B_{\mathrm{A},\nu}$	$2.54\cdot10^{-31}$	$4.5\cdot10^{-33}$	$\mathrm{cm^6{\cdot}s^{-1}}$
$C_{\mathrm{A},\nu}$	$-2.2\cdot10^{-32}$	$2.63\cdot10^{-32}$	$\mathrm{cm^6{\cdot}s^{-1}}$
$H_{\mathrm{A},\nu}$	3.46667	8.25688	1
$N_{0,\nu}$	$1\cdot10^{18}$	$1\cdot10^{18}$	$\mathrm{cm^{-3}}$

Table 2.1: Values of parameters used in describing the Auger coefficients [13, 14, 15, 11].

2.2.2 Carrier Generation Due to Impact Ionization

Especially important for understanding this thesis is the generation of free carriers during impact ionization processes originating from high electric field strengths. The former can occur in reverse-biased *pn*-junctions or in regions which exhibit high fields due to the cell design (as for example at the bottom of a trench in the IGBT cells used in this thesis). As impact ionization processes can produce a high number of carriers the terms avalanche generation and charge multiplication are commonly used for this physical effect as well. Physically speaking impact ionization is band-to-band Auger generation, which was introduced in the previous subsection. In the work for the present thesis, impact ionization is triggered by electrons and holes, respectively. It is not triggered by external means such as cosmic radiation, which can lead to avalanche generation as well. The electron-hole pair production requires a certain threshold in electric field strength as well as a minimum width of the space-charge region for the carriers to attain sufficient acceleration. More precisely, if the width of the space-charge-region is larger than the mean free path between two ionizing impacts, charge multiplication can be attained. The physical model used in this thesis was first published by Chynoweth [16] which along with the measurement results obtained by van Overstraeten and de Man [17] is summarized in the following. It is based on the so-called ionization coefficients $\alpha_\nu(E,T)$, which are the inverse of the mean free paths of the respective carriers and are dependent on the electric field strength as well as the lattice temperature. Using these coefficients, the impact-ionization rate G_{ii} can be written as

$$G_{\mathrm{ii}}(E,T) = \alpha_{\mathrm{n}}(E,T) n v_{\mathrm{n}} + \alpha_{\mathrm{p}}(E,T) p v_{\mathrm{p}} \tag{2.7}$$

multiplication factor M

$$M(U) = \frac{1}{1-(U/U_{\mathrm{B}})^n} \tag{2.8}$$

with U the applied voltage, U_{B} the breakdown voltage and a parameter n. The corresponding integral equations read

$$1 - \frac{1}{M} = \int_0^W \alpha_{\mathrm{n}} \exp\left[-\int_0^x (\alpha_{\mathrm{n}} - \alpha_{\mathrm{p}}) \mathrm{d}\xi\right] \mathrm{d}x \tag{2.9a}$$

$$1 - \frac{1}{M} = \int_0^W \alpha_{\mathrm{p}} \exp\left[-\int_x^W (\alpha_{\mathrm{n}} - \alpha_{\mathrm{p}}) \mathrm{d}\xi\right] \mathrm{d}x \tag{2.9b}$$

with coefficients

$$\alpha_\nu(E,T) = \begin{cases} a_\nu^{\text{low}}\gamma(T)\cdot\exp\left(-b_\nu^{\text{low}}\gamma(T)/E\right) & \text{if } 1.75\cdot10^5\text{V/cm} \le E < 4\cdot10^5\text{V/cm} \\ a_\nu^{\text{high}}\gamma(T)\cdot\exp\left(-b_\nu^{\text{high}}\gamma(T)/E\right) & \text{if } 4\cdot10^5\text{V/cm} \le E < 6\cdot10^5\text{V/cm} \end{cases} \tag{2.10}$$

where

$$\gamma(T) = \tanh\left(\frac{\hbar\omega_{\text{op}}}{2k_{\text{B}}T_0}\right)\cdot\left[\tanh\left(\frac{\hbar\omega_{\text{op}}}{2k_{\text{B}}T}\right)\right]^{-1} \tag{2.11}$$

with optical phonon energy $E_{\text{op}} = \hbar\omega_{\text{op}} = 63\text{meV}$.
It has to be pointed out, that the $\alpha_\nu(E,T)$ have a negative temperature coefficient, which leads to a decrease in carrier generation rates with increasing lattice temperature, making impact ionization a self-limiting process. This is due to the Joule-heating which increases quadratically with the respective carrier current densities. This effect will be of fundamental importance in the discussion of moving current filaments during device turn-off later on.

parameter	$\nu = \text{n}$	$\nu = \text{p}$	unit
$a_\nu^{(\text{low})}$	$7.03\cdot10^5$	$1.58\cdot10^6$	cm^{-1}
$a_\nu^{(\text{high})}$	$7.03\cdot10^5$	$6.71\cdot10^5$	cm^{-1}
$b_\nu^{(\text{low})}$	$1.231\cdot10^6$	$2.036\cdot10^6$	$\text{V}\cdot\text{cm}^{-1}$
$b_\nu^{(\text{high})}$	$1.231\cdot10^6$	$1.693\cdot10^6$	$\text{V}\cdot\text{cm}^{-1}$

Table 2.2: Values of parameters used in describing the impact ionization coefficients [16, 17, 11].

2.2.3 Trap-Assisted Recombination

The presence of impurities or defects, the so-called traps, which have energy levels between the valence band and the conduction band, can lead to recombination processes inside of the IGBT. The physical model published by Shockley, Read and Hall [18, 19] was chosen to describe these effects. The net Shockley-Read-Hall recombination rate is given by

$$R_{\text{net,SRH}} = \frac{np - n_{\text{i,eff}}^2}{\tau_{\text{p}}(n+n_1) + \tau_{\text{n}}(p+p_1)} \tag{2.12}$$

along with

$$n_{\mathrm{i,eff}} = n_{\mathrm{i}} \cdot \exp\left(\frac{E_{\mathrm{G,BGN}}}{2k_{\mathrm{B}}T}\right) \tag{2.13a}$$

$$n_1 = n_{\mathrm{i,eff}} \cdot \exp\left(\frac{E_{\mathrm{T}} - E_{\mathrm{F,i}}}{k_{\mathrm{B}}T}\right) \tag{2.13b}$$

$$p_1 = n_{\mathrm{i,eff}} \cdot \exp\left(-\frac{E_{\mathrm{T}} - E_{\mathrm{F,i}}}{k_{\mathrm{B}}T}\right) \tag{2.13c}$$

with the effective intrinsic density $n_{\mathrm{i,eff}}$, the effective bandgap $E_{\mathrm{G,BGN}}$, the lattice temperature T, the energy level of the trap (defect) E_{T} and the intrinsic Fermi energy $E_{\mathrm{F,i}}$. The doping-dependence of the lifetimes in Eq. 2.12 is implemented using the so-called Scharfetter-Relation [20, 21, 22] which reads

$$\tau_\nu = \tau_{0,\nu} \cdot \left[1 + \frac{N_{\mathrm{A}} + N_{\mathrm{D}}}{N_{\mathrm{ref}}}\right]^{-1} \tag{2.14}$$

with $\tau_{0,\mathrm{n}} = 1 \cdot 10^{-5}\mathrm{s}$, $\tau_{0,\mathrm{p}} = 3 \cdot 10^{-6}\mathrm{s}$ and $N_{\mathrm{ref,n}} = N_{\mathrm{ref,p}} = 1 \cdot 10^{16}\mathrm{cm}^{-3}$.

2.3 Carrier Mobility Models

This section contains a description of the carrier mobility models which are contained in the total mobilities μ_ν inside of the drift-diffusion equations (cf. Eqs 2.1). A short physical introduction into the models along with the formulas as well as parameter values describing the dependencies on several physical quantities such as lattice temperature, doping concentration, surface roughness and high electric fields are given.

2.3.1 High-Field Mobility

Carrier mobilities and their corresponding velocities inside of a power semiconductor device exhibit a strong dependence on the electric field as well as the lattice temperature inside of the device. During normal device operation, electric fields can attain high values inside of space-charge regions which can cause carriers to move at their maximum possible velocity, the so-called saturation velocity $v_{\mathrm{sat},\nu}$. A numerical fit of measurements of carrier drift velocities and their dependence on field strength has been conducted by Caughey and Thomas [23]. Additionally, the dependence of carrier mobilities on the lattice temperature has been done by Canali *et al.* [24]. The resulting equations which describe the high-field

mobilities along with the fit-parameters can be written as

$$\mu_\nu(E,T) = \mu_{\text{low},\nu} \cdot \left[1 + \left(\frac{\mu_{\text{low},\nu} E}{v_{\text{sat},\nu}(T)}\right)^{\beta_\nu}\right]^{-1/\beta_\nu} \tag{2.15}$$

with the temperature dependence of the respective saturation velocities

$$v_{\text{sat},\nu}(T) = v_{\text{sat},0,\nu} \left(\frac{300K}{T}\right)^{v_{\text{sat,exp},\nu}} \tag{2.16}$$

$$\beta_\nu = \beta_{0,\nu} \left(\frac{T}{300K}\right)^{\beta_{\text{exp},\nu}} \tag{2.17}$$

parameter	$\nu = \text{n}$	$\nu = \text{p}$	unit
$v_{\text{sat},0,\nu}$	$1.07 \cdot 10^7$	$8.37 \cdot 10^6$	$\text{cm}\cdot\text{s}^{-1}$
$v_{\text{sat,exp},\nu}$	0.87	0.52	1
$\beta_{0,\nu}$	1.109	1.213	1
$\beta_{\text{exp},\nu}$	0.66	0.17	1

Table 2.3: Values of parameters used in describing the high-field mobilities [23, 24, 11].

2.3.2 Reduction of Carrier Mobility at Interfaces

The mobilities of carriers inside an inversion layer, as is the case in the channel region of a MOSFET or the MOSFET-part of an IGBT, can be reduced due to physical scattering processes deriving from acoustic-phonon scattering (also termed surface-phonon scattering, ac) or scattering due to surface roughness (sr) at the material interface between silicon and gate-oxide. In this thesis, this reduction applies especially to electrons inside of an n-channel trench-IGBT (cf. chapter 1). The mobility degradation model presented by Lombardi *et al.* [25] is used in this work to incorporate these physical effects as a function of the electric field component perpendicular to the silicon-oxide interface $E_\perp$ along with the lattice temperature T, where the individual contributions are combined using Matthiessen's rule to give a total mobility. With increasing distance from the material-interface, the contributions of mobility-reducing effects diminish, leading the total mobility to attain the

values of the bulk mobility for sufficiently large distances. In this sense, the mobility model by Lombardi *et al.* can be viewed as a 'local' mobility model which is given by the following expressions

$$\mu_{\mathrm{ac},\nu}(E_\perp, T) = \frac{B_\nu}{E_\perp} + \frac{C_\nu}{\sqrt[3]{E_\perp} \cdot (T/300K)} \cdot (N_{\mathrm{A},0} + N_{\mathrm{D},0})^{\lambda_\nu} \tag{2.18a}$$

$$\mu_{\mathrm{sr},\nu}(E_\perp) = \left[\frac{1}{\delta_\nu} \left(\frac{E_\perp}{E_{\mathrm{ref}}} \right)^2 + \frac{E_\perp^3}{\eta_\nu} \right]^{-1} \tag{2.18b}$$

To arrive at the effective mobility μ_ν, these mobility contributions are combined with the bulk mobility $\mu_{\mathrm{b},\nu}$ using Matthiessen's rule, as has already been mentioned, to give

$$\mu_\nu = \left[\sum_{\xi=\mathrm{b,ac,sr}} \frac{1}{\mu_{\xi,\nu}} \right]^{-1} \tag{2.19}$$

As was pointed out by Lombardi *et al.*, this relationship is assumed for simplicity and is not theoretically justified, as a full thermodynamic treatment of the resulting total mobility would be required.

parameter	$\nu = \mathrm{n}$	$\nu = \mathrm{p}$	unit
B_ν	$4.75 \cdot 10^7$	$9.93 \cdot 10^6$	$\mathrm{cm \cdot s^{-1}}$
C_ν	$5.80 \cdot 10^2$	$2.95 \cdot 10^3$	$\mathrm{cm^{5/3} \cdot V^{-2/3} \cdot s^{-1}}$
λ_ν	0.1250	0.0317	1
δ_ν	$5.82 \cdot 10^{14}$	$2.05 \cdot 10^{14}$	$\mathrm{cm^2 \cdot (V \cdot s)^{-1}}$
η_ν	$5.82 \cdot 10^{30}$	$2.05 \cdot 10^{30}$	$\mathrm{V^2 \cdot (cm \cdot s)^{-1}}$

Table 2.4: Values of parameters used in describing the Lombardi-model mobilities [25, 11].

2.3.3 Klaassen Mobility Model (Philips Unified Mobility Model)

To account for physical effects that affect the bulk mobility of majority and minority carriers such as screening of the impurities by charge carriers, electron-hole scattering, clustering of impurities and their respective temperature dependencies, the unified mobility model introduced by Klaassen *et al.* [26, 27] was chosen. These four contributions causing

scattering processes will be described more precisely in the following.
The majority mobilities due to lattice scattering of the Klaassen-model is identical to the doping dependent mobility model by Masetti *et al.* [28] in the limit of low impurity concentrations and reads

$$\mu_{\mathrm{L},\nu}(T) = \mu_{\max,\nu}\left(\frac{T}{300K}\right)^{-\theta_\nu} \tag{2.20}$$

including its temperature dependence. The parameters for this model are given in Tables 2.5 and 2.6. The majority impurity scattering including screening encompasses the electron mobility due to donor scattering and the hole mobility due to acceptor scattering

$$\mu_{\mathrm{I},\nu} = \mu_{N,\nu}\cdot\frac{N_{\mathrm{sc},\nu}}{N_{\mathrm{sc,eff},\nu}}\left(\frac{N_{\mathrm{ref},\nu}}{N_{\mathrm{sc},\nu}}\right)^{\alpha_\nu} + \mu_{\mathrm{c},\nu}\cdot\frac{n+p}{N_{\mathrm{sc,eff},\nu}} \tag{2.21}$$

with temperature-dependent coefficients given by

$$\mu_{N,\nu}(T) = \frac{\mu_{\max,\nu}^2}{\mu_{\max,\nu}-\mu_{\min,\nu}}\left(\frac{T}{300K}\right)^{3(\alpha_\nu-1/2)} \tag{2.22a}$$

$$\mu_{\mathrm{c},\nu}(T) = \frac{\mu_{\max,\nu}\cdot\mu_{\min,\nu}}{\mu_{\max,\nu}-\mu_{\min,\nu}}\left(\frac{T}{300K}\right)^{1/2} \tag{2.22b}$$

and the effective concentrations if screening is taken into account

$$N_{\mathrm{sc,n}} = N_{\mathrm{D}}^* + N_{\mathrm{A}}^* + p \tag{2.23a}$$

$$N_{\mathrm{sc,eff,n}} = N_{\mathrm{D}}^* + G(P_{\mathrm{n}})N_{\mathrm{A}}^* + \frac{p}{F(P_{\mathrm{n}})} \tag{2.23b}$$

$$N_{\mathrm{sc,p}} = N_{\mathrm{D}}^* + N_{\mathrm{A}}^* + n \tag{2.23c}$$

$$N_{\mathrm{sc,eff,p}} = N_{\mathrm{A}}^* + G(P_{\mathrm{p}})N_{\mathrm{D}}^* + \frac{n}{F(P_{\mathrm{p}})} \tag{2.23d}$$

as well as

$$N_{\mathrm{D}}^* = N_{\mathrm{D,0}}\cdot\left(1+\frac{N_{\mathrm{D,0}}^2}{c_{\mathrm{D}}N_{\mathrm{D,0}}^2+N_{\mathrm{ref,D}}^2}\right) \tag{2.24a}$$

$$N_{\mathrm{A}}^* = N_{\mathrm{A,0}}\cdot\left(1+\frac{N_{\mathrm{A,0}}^2}{c_{\mathrm{A}}N_{\mathrm{A,0}}^2+N_{\mathrm{ref,A}}^2}\right) \tag{2.24b}$$

$F(P_\nu)$ and $G(P_\nu)$ are functions of the screening parameter P_ν which in turn is given by

$$F(P_\nu) = \frac{\kappa_1 P_\nu^{\kappa_2} + \kappa_3 + \kappa_4 \cdot (m_\nu^*/m_{\overline{\nu}}^*)}{P_\nu^{\kappa_2} + \kappa_5 - \kappa_6 \cdot (m_\nu^*/m_{\overline{\nu}}^*)} \tag{2.25a}$$

$$G(P_\nu) = 1 - a_\mathrm{g} \cdot \left[b_\mathrm{g} + P_\nu \cdot \left(\frac{m_0}{m_\nu^*} \frac{T}{300K} \right)^{\alpha_\mathrm{g}} \right]^{-\beta_\mathrm{g}} + c_\mathrm{g} \cdot \left[P_\nu \cdot \left(\frac{m_\nu^*}{m_0} \frac{300K}{T} \right)^{\alpha_\mathrm{g}'} \right]^{-\gamma_\mathrm{g}} \tag{2.25b}$$

with fit-parameters $\kappa_1 = 0.7643$, $\kappa_2 = 0.6478$, $\kappa_3 = 2.2999$, $\kappa_4 = 6.5502$, $\kappa_5 = 2.3670$, $\kappa_6 = 0.8552$. The screening parameter P_ν is given by

$$P_\nu = \left(\frac{f_\mathrm{CW}}{3.97 \cdot 10^{13} \mathrm{cm}^{-2} N_{\mathrm{sc},\nu}^{-2/3}} + \frac{f_\mathrm{BH} \cdot (n+p)}{1.36 \cdot 10^{20} \mathrm{cm}^{-3}} \frac{m_0}{m_\nu^*} \right)^{-1} \left(\frac{T}{300K} \right)^2 \tag{2.26}$$

The minority impurity scattering encompasses the contribution to the electron mobility due to acceptor scattering $\mu_{\mathrm{A,n}}$ and the contribution to the hole mobility due to donor scattering $\mu_{\mathrm{D,p}}$. Here, c denotes the free-carrier concentration $c = n + p$.

$$\mu_{\mathrm{A,n}}(N_\mathrm{A}^*, c) = \mu_{\mathrm{D,n}}(N_\mathrm{D}^* = N_\mathrm{A}^*, c) \cdot \frac{1}{G(P_\mathrm{n})} \tag{2.27a}$$

$$\mu_{\mathrm{D,p}}(N_\mathrm{D}^*, c) = \mu_{\mathrm{A,p}}(N_\mathrm{A}^* = N_\mathrm{D}^*, c) \cdot \frac{1}{G(P_\mathrm{p})} \tag{2.27b}$$

The electron-hole scattering encompasses the contribution to the electron mobility due to hole scattering $\mu_{\mathrm{n,p}}$ and the contribution to the hole mobility due to electron scattering $\mu_{\mathrm{p,n}}$.

$$\mu_{\mathrm{n,p}}(p, c) = \mu_{\mathrm{D,n}}(N_\mathrm{D}^* = p, c) \cdot F(P_\mathrm{n}) \tag{2.28a}$$

$$\mu_{\mathrm{p,n}}(n, c) = \mu_{\mathrm{A,p}}(N_\mathrm{A}^* = n, c) \cdot F(P_\mathrm{p}) \tag{2.28b}$$

The resulting bulk mobility $\mu_{\mathrm{b},\nu}$ for electrons and holes, respectively is then given by

$$\frac{1}{\mu_{\mathrm{b},\nu}} = \frac{1}{\mu_{\mathrm{L},\nu}} + \frac{1}{\mu_{\mathrm{I},\nu}} \tag{2.29}$$

using Mathiessen's rule once more.

parameter	$\nu = \mathrm{n}$	$\nu = \mathrm{p}$	unit
$\mu_{\max,\nu}$	1414	470.5	$\mathrm{cm}^2\cdot(\mathrm{V}\cdot\mathrm{s})^{-1}$
$\mu_{\min,\nu}$	68.5	44.9	$\mathrm{cm}^2\cdot(\mathrm{V}\cdot\mathrm{s})^{-1}$
θ_ν	2.285	2.247	1
$N_{\mathrm{ref},\nu}$	$9.20 \cdot 10^{16}$	$2.23 \cdot 10^{17}$	cm^{-3}
α_ν	0.711	0.719	1

Table 2.5: Values of parameters used in the Klaassen-model of mobilities [26, 27, 28, 11].

parameter	value	unit
a_g	0.89233	1
b_g	0.41372	1
c_g	0.005978	1
α_g	0.28227	1
α'_g	0.72169	1
β_g	0.19778	1
γ_g	1.80618	1

parameter	value	unit
m^*_n/m_0	1	1
m^*_p/m_0	1.258	1
f_CW	2.459	1
f_BH	3.828	1
c_D	0.21	1
c_A	0.50	1
$N_{\mathrm{ref,D}}$	$4.0 \cdot 10^{20}$	cm^{-3}
$N_{\mathrm{ref,A}}$	$7.2 \cdot 10^{20}$	cm^{-3}

Table 2.6: Klaassen parameter set for silicon [26, 27, 28, 11]. Note: the values for c_D and $N_{\mathrm{ref,D}}$ were determined for phosphorous-doped silicon whereas the values for c_A and $N_{\mathrm{ref,A}}$ were determined for boron-doped silicon.

2.4 Bandgap Narrowing

The bandgap E_G is defined as the difference in energy between the lowest energy level in the conduction band and the highest energy in the valence band. It exhibits a dependence on the impurity concentration for high doping levels: the bandgap becomes smaller in the case of high doping concentrations of around $10^{15}\mathrm{cm}^{-3}$. The model used for the description of bandgap narrowing in this thesis was introduced by Slotboom and de Graaff [29, 30, 31] and it assumes that the band edges of valence band and conduction band are shifted by $\Delta E_\mathrm{G}/2$, respectively, meaning that $E_{\mathrm{V,BGN}} = E_\mathrm{V} + \Delta E_\mathrm{G}/2$ and that $E_{\mathrm{C,BGN}} = E_\mathrm{C} - \Delta E_\mathrm{G}/2$. Furthermore Slotboom and de Graaff assume ΔE_G to be dependent on the total impurity

concentration N_{imp} only. The effect of bandgap narrowing is, as was already introducen in this chapter, taken into account in other physical models as well as in the effective intrinsic density (cf. Eq. 2.13a) and in the heat flow equation (cf. Eq. 2.31). The formula for bandgap narrowing as proposed in [29] reads

$$\Delta E_{\text{G}}(N_{\text{imp}}) = E_{\text{ref}} \left[\ln\left(\frac{N_{\text{imp}}}{N_{\text{ref}}}\right) + \sqrt{\left[\ln\left(\frac{N_{\text{imp}}}{N_{\text{ref}}}\right)\right]^2 + \frac{1}{2}} \right] \tag{2.30}$$

where $E_{\text{ref}} = 9 \cdot 10^{-3}\text{eV}$ and $N_{\text{ref}} = 1 \cdot 10^{17}\text{cm}^{-3}$ are constants.

2.5 Electro-Thermal Coupling

So far, the physical models describing effects of generation and recombination, scattering and bandgap narrowing have been presented. Most of these effects are dependent on the lattice temperature T, which up to now was assumed to be constant and furthermore, was not influenced by these physical effects. In other words, the electrical and the thermal domain were not considered to be coupled, leading to a non-self-consistent theoretical description which in turn does not account for temperature effects as the lattice temperature is bound to be homogeneous throughout the entire device and therefore effects of local heating, which can potentially lead to thermal destruction of the device, are neglected. In this section it will be shown how the electrical and the thermal simulation domain can be coupled, leading to a self-consistent thermodynamic model for the lattice temperature as has been introduced by [32, 33, 34, 35]. Here, the lattice temperature is treated as a dynamic variable, and effects of heat generation and temperature transport can be modelled. This enables the theoretical analysis to describe inhomogeneous temperature distributions due to inhomogeneous current densities, which can lead to local temperature hotspots and, in the case of destruction, thermal runaway of the device. Theoretically, the coupling of the electrical and the thermal domain is achieved by a system of coupled partial differential equations which are derived from a combination of Poisson's equation, the continuity equations (cf. Eqs. 2.2) and the heat flow equation (cf. Eqs. 2.31 and 2.33), which can be solved in a self-consistent way. The lattice temperature T is treated as a dynamic variable

and is computed from the heat flow equation

$$\begin{aligned} c_{\mathrm{L}}\frac{\partial}{\partial t}T - \nabla\cdot\kappa\nabla T = &-\nabla\left[\left(P_{\mathrm{n}}^{\mathrm{te}}T+\Phi_{\mathrm{n}}\right)\mathbf{j}_{\mathrm{n}}+\left(P_{\mathrm{p}}^{\mathrm{te}}T+\Phi_{\mathrm{p}}\right)\mathbf{j}_{\mathrm{p}}\right] \\ &-\left(E_{\mathrm{C}}+\frac{3}{2}k_{\mathrm{B}}T\right)\nabla\cdot\mathbf{j}_{\mathrm{n}}-\left(E_{\mathrm{V}}-\frac{3}{2}k_{\mathrm{B}}T\right)\nabla\cdot\mathbf{j}_{\mathrm{p}} \\ &+e_0(R-G)\left(E_{\mathrm{G,BGN}}+3k_{\mathrm{B}}T\right) \end{aligned} \tag{2.31}$$

with the lattice heat capacity c_{L}, the thermal conductivity of the material κ, the thermoelectric power (Seebeck coefficients) P_{ν}^{te}, the quasi-Fermi potential Φ_{ν}, the conduction (valence) band energy E_{C} (E_{V}), the net recombination rate R_{net} and the current densities $\mathbf{j}_{\nu}$ which are given by

$$\mathbf{j}_{\nu} = -\nu e_0\mu_{\nu}\left(\nabla\Phi_{\nu}+P_{\nu}^{\mathrm{te}}\nabla T\right) \tag{2.32}$$

Equation 2.31 can be rewritten as

$$c_{\mathrm{L}}\frac{\partial}{\partial t}T - \nabla\cdot\kappa\nabla T = H_{\mathrm{Joule}}+H_{\mathrm{rec}}+H_{\mathrm{Peltier}}+H_{\mathrm{trans}} \tag{2.33}$$

where the respective components are given by

$$H_{\mathrm{Joule}} = \frac{\mathbf{j}_{\mathrm{n}}^2}{e_0 n\mu_{\mathrm{n}}}+\frac{\mathbf{j}_{\mathrm{p}}^2}{e_0 p\mu_{\mathrm{p}}} \tag{2.34a}$$

$$H_{\mathrm{rec}} = e_0(R-G)\left(E_{\mathrm{G,BGN}}+3k_{\mathrm{B}}T\right) \tag{2.34b}$$

$$H_{\mathrm{Peltier}} = -T\left(\nabla P_{\mathrm{n}}^{\mathrm{te}}\cdot\mathbf{j}_{\mathrm{n}}+\nabla P_{\mathrm{p}}^{\mathrm{te}}\cdot\mathbf{j}_{\mathrm{p}}\right) \tag{2.34c}$$

$$H_{\mathrm{trans}} = -\left(E_{\mathrm{C}}+\frac{3}{2}k_{\mathrm{B}}T\right)\nabla\cdot\mathbf{j}_{\mathrm{n}}-\left(E_{\mathrm{V}}-\frac{3}{2}k_{\mathrm{B}}T\right)\nabla\cdot\mathbf{j}_{\mathrm{p}} \tag{2.34d}$$

which contribute to heating/cooling and are Joule heat, recombination heat, Peltier (Thomson) heat and an additional term which exists only in non-stationary cases and which accounts for non-homogeneous temperature distributions as well as for local variations of the bandgap.

3. Single IGBT Simulation Structure and Calibration

In this chapter the basic design of the simulation structure, as well as their calibration based on static and transient measurements, will be described. This calibration aims at reproducing experimental data obtained from measurements of a single IGBT chip during operation within the specified ratings, i.e. within the safe-operating area of the chip, for static as well as transient measurements. Successfully conducting the calibration forms the basis for qualitatively as well as quantitatively investigating the physical processes inside of the device, when used beyond the limits of the safe-operating area.
When performing the simulations necessary for the calibration of the simulation structure, it is sufficient to use a single simulation structure. This is justified since each cell within the chip behaves approximately the same, i.e. effects that may cause a significantly inhomogeneous current flow (regions with increased current density) do not occur. In other words, no physical effects inside of the device have a range which lies beyond the lateral extension of a single simulation structure.

3.1 Single Simulation Structure

In this section, a detailed description of the simulation structure used for the calibration process is given. The basic design of the simulation structure along with the working principles of the trench-IGBT were already introduced in chapter 1. As can be seen in Figure 3.1a, the three electrical contacts are the so-called emitter, gate and collector contact. The former two are located at the front side of the device whereas the latter one is located at the back-side. All these contacts are modelled to have no ohmic or thermal resistance.
The gate contact is modelled to have a work function (barrier) of -0.55eV for a better reproduction of the gate-emitter threshold voltage U_{th} (The reason being the work function of the n-doped polysilicon material of the gate electrode). Thermal boundary conditions

are not implemented due to the isothermal calculations in the calibration procedure. This is justified since pulsed measurements were performed in experiments, where self-heating can be neglected due to short duration of current conduction inside of the device under test.

Since the measurements were performed using an IGBT-chip with an active area of around 1cm^2, the simulation must adhere to this by simulating the same active area. In Figure 4.1a, a top view of the basic geometry of the real-chip can be seen. It is a two-dimensional array of quadratic cells that resembles a chess-board. In order to minimize the computational effort needed, the behaviour of the entire chip can be described by the behaviour of an "elementary cell" (elementary half-cell), as was already mentioned and justified in the introductory section to this chapter. The geometrical connection between real chip and simulation structure can be seen in Figure 3.1 as well.

A single simulation structure roughly measures 10μm in lateral direction and 400μm in vertical direction, which is due to the high blocking voltage of the device which amounts to 3.3kV. The inner part of the simulation structure is given by analytic profiles both what the basic geometry and the doping profiles are concerned. Among the main doping implantations are a highly n-doped source region, a p-doped body region, a p-doped anti-latch-up region, a floating p-doped region beneath the gate-oxide, a lowly doped n-region which is commonly referred to as the base material, an n-doped field stop region and a highly p-doped emitter region at the back-side of the device just before the collector contact.

The gate contact itself is, in the MOS part of the structure, surrounded by an oxide layer of 120nm thickness, which mainly follows the geometry of the trench. The bottom of the trench resembles a semi-circle, having a constant curvature. In real chips, the gate contact is filled with poly-silicon, whereas in the simulations conducted in the course of this thesis this is simply replaced by an electrode since its influence is secondary to the effects investigated. The boundary conditions at the non-contacted (left and right) edges of the structure are, as in all the calculations presented in this work, of the homogeneous Neumann type.

Of special importance are the distances (in a single simulation structure) between the left vertical edge of the structure and the beginning of the oxide layer at the emitter side, the lateral extension of the trench as well as the lateral distance between the right edge of the trench and the right edge of the simulation structure, as can be seen in Figure 3.1a. These have to resemble the real chip geometry in a way, that the areas that conduct current and the areas which do not have the same ratio in the respective simulation geometry that is

used, which can be stripe- or cylinder-shaped.
Employing this criterion to simulation structures with different geometries gives different values for the inner and the outer radius of the simulation structure under the assumption of a constant lateral extension of the trench.
The discretization of the structure is optimized with special regard to minimizing the amount of mesh-points with the constraints of smooth gradients in the doping profiles, good resolution of the MOS-channel and a local grid at the interface between silicon and oxide that is small enough to resolve the length scales required for the degradation of electron mobility due to surface roughness inside of the MOS-channel as described by the carrier mobility degradation model by Lombardi *et al.* [25] (see also [11]).

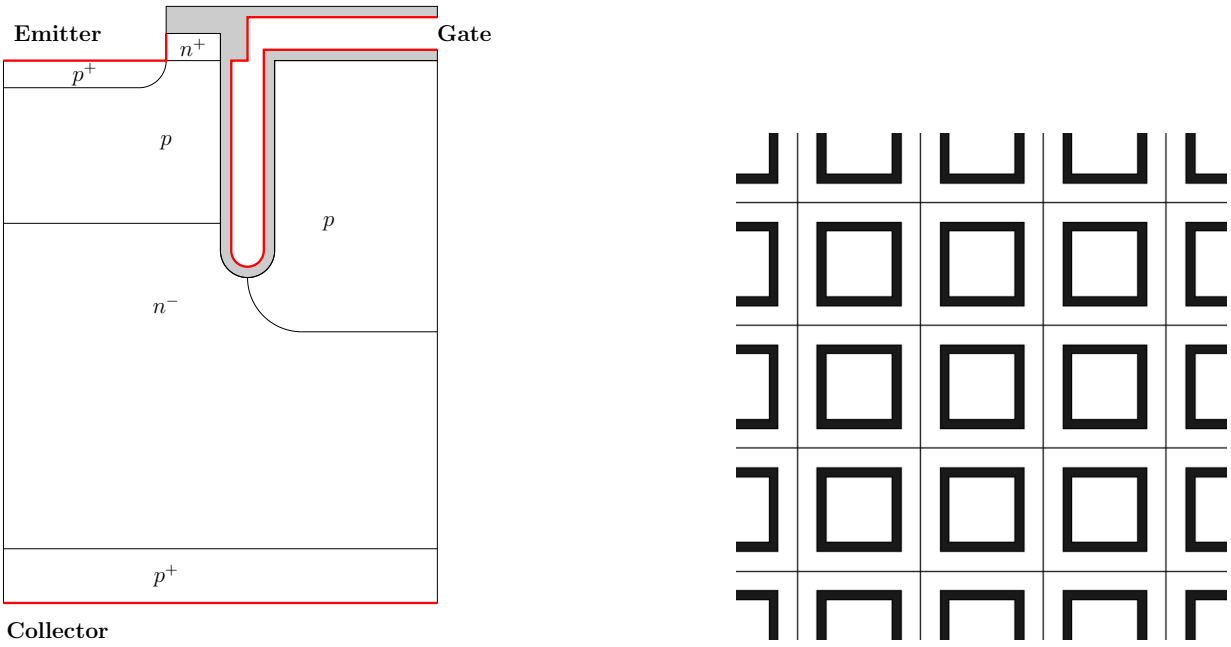

(a) (b)

Figure 3.1: (a) Depiction of the basic structure and doping profiles of the simulation structure used to conduct the calibration. This structure looks qualitatively the same for single-cell simulations in stripe- or cylindrical geometry. (b) Depiction of the layout of several cells within the same IGBT-chip. Within the safe-operating area the behaviour of the entire chip can be reproduced by the behaviour of a single cell.

3.2 Static Calibration

The first part of the calibration procedure aims to reproduce as closely as possible the static characteristics of the device with a special focus on the significant points such as the gate-emitter threshold voltage U_{th} and the collector-emitter saturation voltage as given by measurement (and data-sheet [2]). To this end the transfer characteristics (collector current as a function of the gate-emitter voltage $I_{\mathrm{C}}(U_{\mathrm{GE}})$ with collector emitter voltage U_{CE} held constant) and the output characteristics (collector current as a function of collector-emitter voltage $I_{\mathrm{C}}(U_{\mathrm{CE}})$ with gate-emitter voltage U_{GE} held constant), respectively, were reproduced theoretically. This was done for a homogeneous isothermal lattice temperature of 423K (150°C) just as in the experiment, which is the maximum allowed operating temperature for the device.

Among the parameters that were varied for the calibration are the effective electron mobility inside of the MOS-channel as well as the peak-concentrations of the relevant doping profiles. This was done for simulation structures exhibiting stripe geometry as well as for simulation structures exhibiting cylindrical geometry. The differences in their agreement with measured data is negligible for the respective best set of parameters (the effective channel mobility being higher in the cylindrical case). Furthermore it was found, that the agreement with experiment (based on the relative error) is not the same over the entire voltage range. Consequently a minimization of the relative error in transfer characteristics at the usual operating voltage of 15V was given priority. The best results that were obtained and were subsequently used in the simulations leading to the theoretical investigations presented in this thesis are depicted in Fig. 3.2 for both static characteristics. In the relevant parts, the simulations reproduce the measurements with a relative error of 1% whereas the relative error does no surpass the 5% mark anywhere in the entire voltage range. This is sufficiently exact since deviations deriving from the fabrication process are likely to have a larger impact on the characteristics.

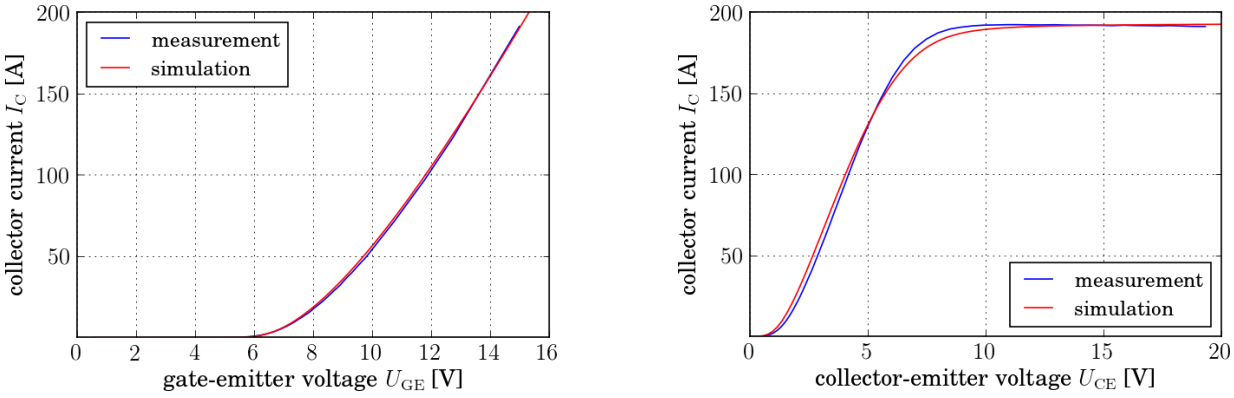

Figure 3.2: Comparison of measurement (blue) and simulated data (red) at a homogeneous lattice temperature of 150°C. (a) For the transfer characteristics $I_C(U_{GE})$ at a fixed value for U_{CE} of 20V. (b) For the output characteristics $I_C(U_{CE})$ at a fixed value for U_{GE} of 15V.

3.3 Transient Calibration

The second part of the calibration procedure focuses on finding the external parameters that govern the temporal behaviour of contact voltages and currents. The turn-off measurements for the characterization used an inductive load, the circuit for which is depicted in Fig. 3.4b.

The nominal current density of the device was chosen for the initial current density for the transient measurement, whereas the gate resistance which basically governs the duration of the turn-off process, was chosen to be 100Ω just as in the measurement itself. Fig. 3.4b also shows a freewheeling diode D_F implemented both as compact model as well as a fully simulated diode in a mixed-mode simulation. The difference between these is, for the present purposes, negligible and mainly lies in the behaviour of the collector-emitter voltage after reaching its peak value, shortly before dropping down to the DC-link voltage which amounts to 1.8kV for the calibration (cf. 3.4a). Accordingly, the compact model of the diode was used as it is faster and computationally more robust. Additionally, the transient simulations are isothermal as well, thus no thermal boundary conditions were applied to the edges of the structure.

Special focus lies on the temporal behaviour of the gate-emitter voltage $U_{GE}(t)$, collector current $I_C(t)$ and the collector-emitter voltage $U_{CE}(t)$, the results of which can be seen in Fig. 3.3 and 3.4a. The agreement is good and the parameters giving the smallest relative

errors were extracted and used for the theoretical analysis.

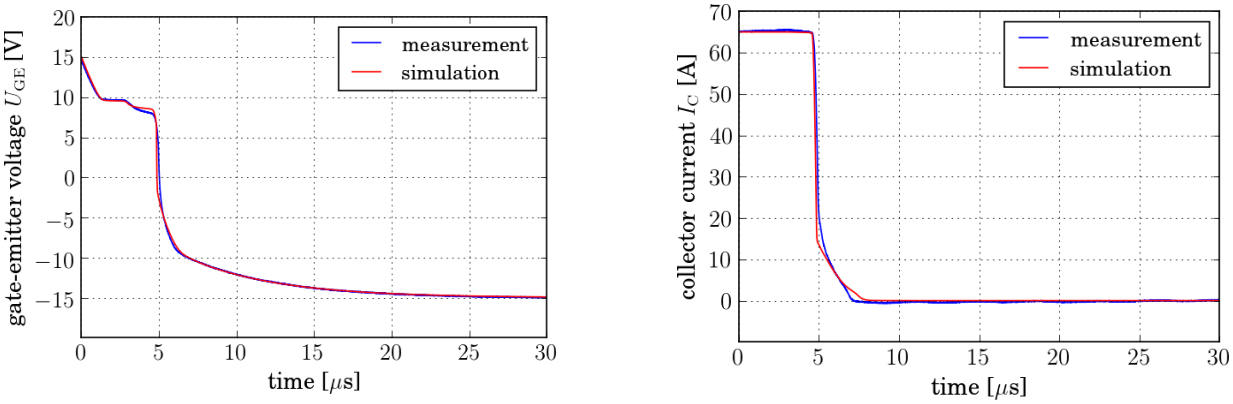

(a) (b)

Figure 3.3: Comparison of measurement (blue) and simulated data (red) for transient curves during the turn-off process for isothermal calculations at a homogeneous lattice temperature of 150°C. The gate-resistance in this case amounts to 100Ω. (a) The gate-emitter voltage U_{GE} as a function of time. The turn-off itself is defined as the switch from $U_{\mathrm{G,on}}$ =15V to $U_{\mathrm{G,off}}$ = −15V, as can be seen in this diagram. (b) The collector current I_{C} as a function of time during the same turn-off process. The initial current in this case amounts to the nominal current of a single IGBT-chip of 62.5A. The DC-link voltage was chosen to be $U_{\mathrm{DC\text{-}link}}$=1.8kV.

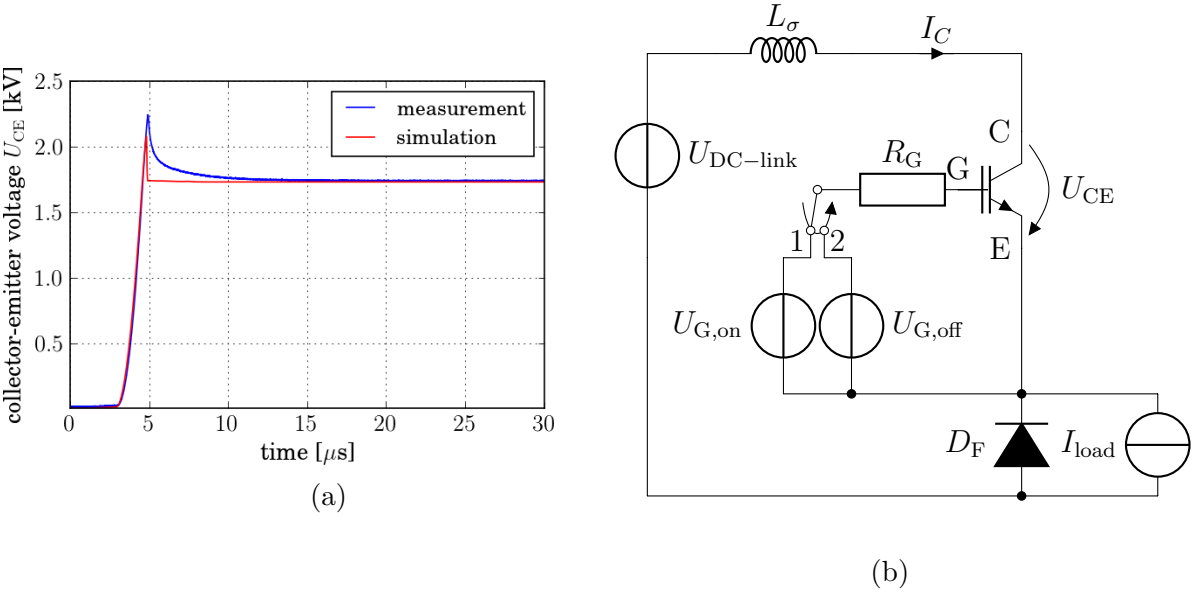

(a) (b)

Figure 3.4: (a) The collector-emitter voltage U_{CE} as a function of time. The DC-link voltage in this case amounts to 1.8kV. (b) Depiction of the electrical circuit used for calibration in the simulation of the turn-off process. Mainly the stray-inductance L_σ and the gate resistance R_{G} where varied in the course of the calibration. (Values were $R_{\mathrm{G}} = 100\Omega$ and $L_\sigma = 700\mathrm{nH}$.)

4. Monolithically Integrated IGBT Cell Arrays

In order to model non-linear physical effects like current filaments, that may occur beyond the limits of the safe-operating area, simulation structures with large lateral extensions are needed. This is due to the fact that the lateral range of these phenomena is significantly larger than the lateral extension of a single simulation structure. Hence, for a quantitatively sensible analysis of current filaments and the latch-up process it is mandatory to use physically connected cells that allow for electrical as well as thermal cross-talk, i.e. monolithically integrated simulation structures. Interaction across the external electrical circuit only, as in a parallel circuit of multiple individual cells, is thus not sufficient to model these effects that potentially limit the safe-operating area of the device.

For the generation of simulation structures the real cell geometry of the IGBT-chip itself is fundamentally important. It is a two-dimensional array of quadratic cells that resembles a checker-board (see Fig. 4.1a). (This stands in contrast to stripe-shaped cells in the real-chip geometry, which were not subject of investigation in this work.) As was already discussed in chapter 3, an approximation of the real-chip geometry is achieved by using suitable simulation geometries like two-dimensional Cartesian coordinates or cylindrical coordinates. This makes the simulation of large structures computationally accessible by state-of-the-art hardware and software.

This chapter describes how such large simulation structures can be generated in different simulation symmetries from a theoretical point of view in order to investigate current-crowding effects that can cause device failure as a function of the filament geometry. This in turn allows for an investigation of geometrical effects of current filaments on the safe-operating area.

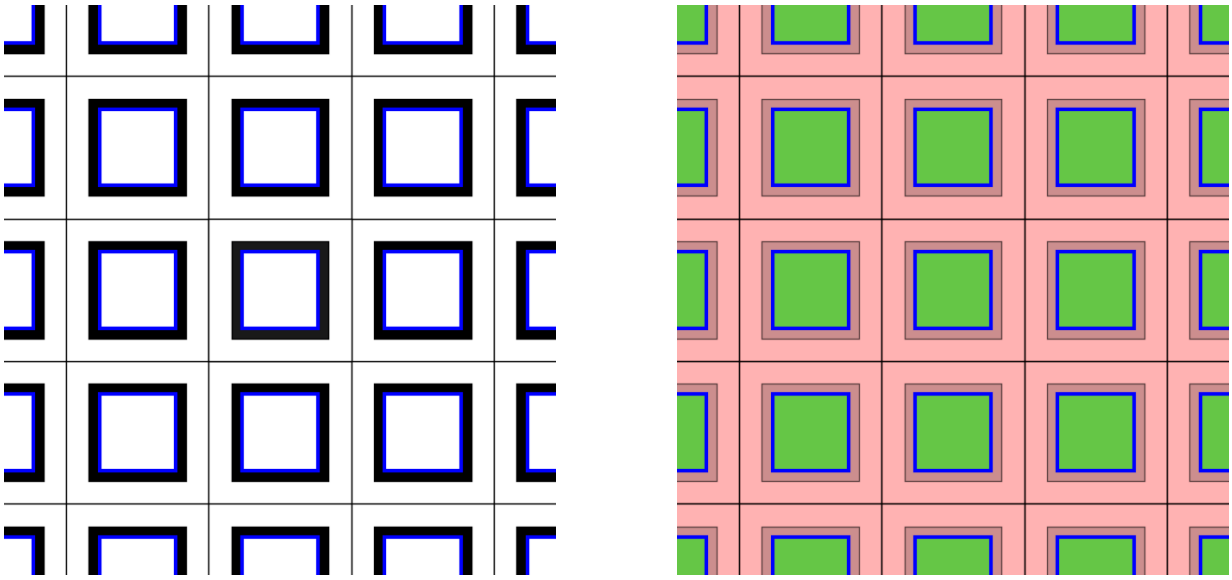

(a) (b)

Figure 4.1: (a) Sketch of the (top view) of an IGBT chip consisting of several quadratic cells. The black regions depict the poly-silicon trenches of each cell, whereas the solid black lines depict the borders of each cell. The blue coloured lines indicate the locations of the MOS-channels. (b) The same IGBT-chip divided into regions that are electrically contacted (green) and not-contacted (red). The back-side of the IGBT consisting of the collector only is contacted homogeneously across the entire area.

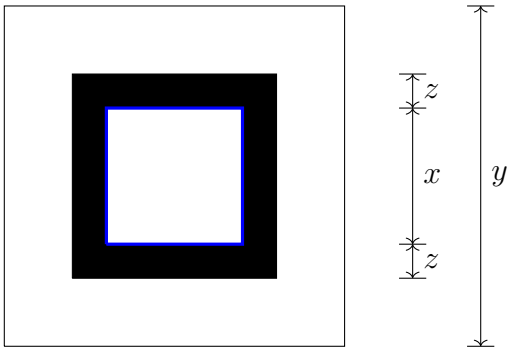

Figure 4.2: A single IGBT-cell and the geometrical measures as used in the calculations of this chapter. Note that z is defined for convenience purposes only.

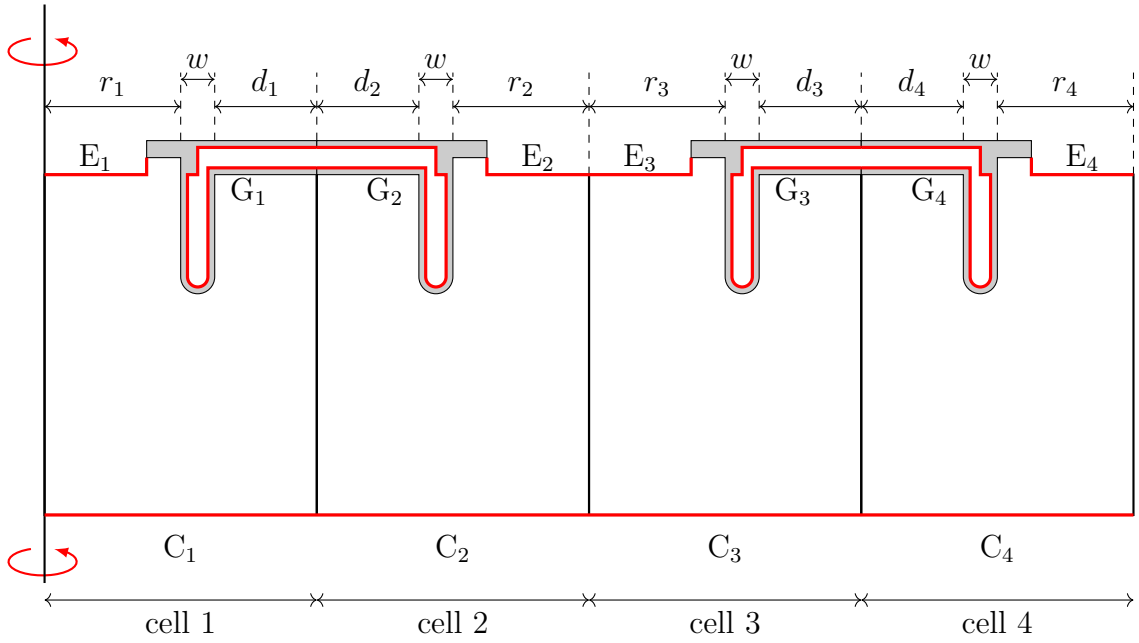

Figure 4.3: Sketch of a monolithically integrated simulation structure consisting of 4 cells. Emitter contacts (E_k), gate contacts (G_k) and collector contacts (C_k). w_{tr} is held constant. In case of stripe symmetry: $r_k = r$ and $d_k = d \;\; \forall k \in N$.

4.1 Approach

The aim of this approach is to generate sufficiently large simulation structures for the investigation of far-ranging non-linear physical effects on the basis of the real-cell geometry. As a criterion for the mapping from the real-chip geometry to the simulation structure, the ratio between electrically contacted areas and non-contacted areas (see Fig. 4.1b) within one chip was chosen to be constant. This constraint can be applied to any simulation structure invariant of its geometry.
The first approximation to the real-chip geometry used is stripe geometry. Here the geometry is adapted by extracting a stripe-shaped 'slice' of the chip that does not exhibit any dependence on the third spatial dimension (cf. Fig 4.4a). The condition for conversion mentioned above is met automatically and the similarities to the real-chip are obvious. However, this approach leads to a severe limitation of the geometry a filament can attain as it develops inside of the simulation structure: filaments are bound to have a stripe-shaped geometry and no dependency on the third spatial dimension whatsoever.
This limitation can be avoided by applying a different mapping to the real-chip geometry which uses cylindrical symmetry for the generation of simulation structures (cf. Fig. 4.4b). A justification for the cylindrical approach will be given in chapter 6, based on the simulation results obtained by transient turn-off simulations of stripe structures which will be discussed in detail in chapter 5.
Common to both simulation approaches is that a significant redistribution of current inside of the device itself can take place in case of symmetry-breaking. This is not possible in simulation structures which consist of a single cell only as their restricted space massively restricts phenomena with a large lateral extension.
Generally speaking, in structures with larger lateral extension and, hence, a multitude of trenches where current filaments can originate, more possibilities for current redistribution exist which in turn lead to a potentially stronger current crowding and regions with increased current density.

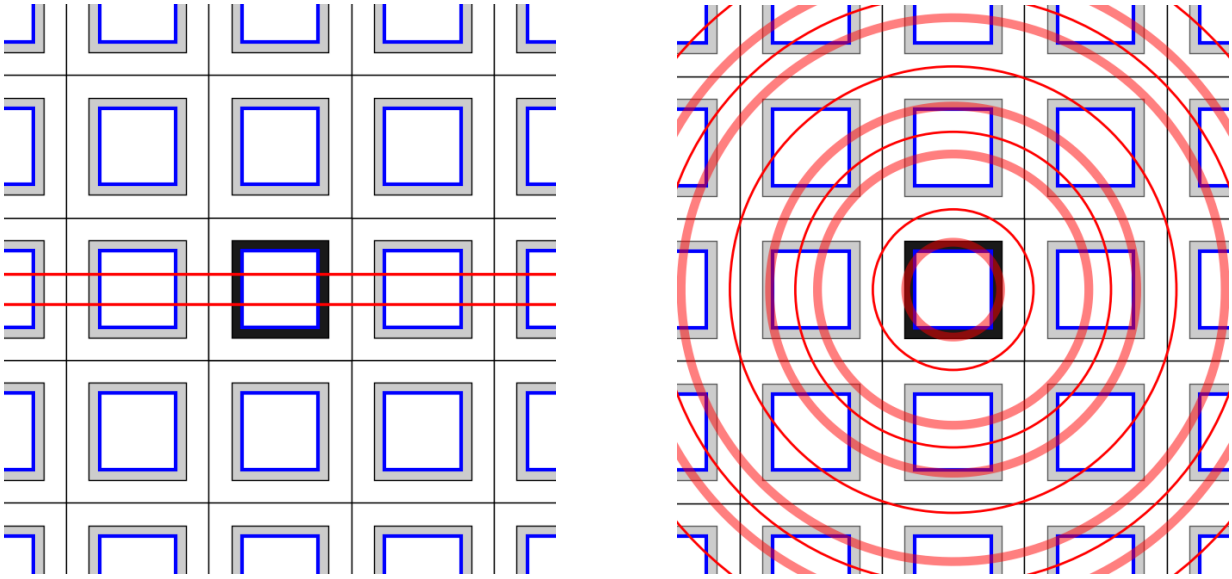

(a) (b)

Figure 4.4: Comparison between real-chip geometry and two-dimensional Cartesian coordinates (a) and cylindrical coordinates (b).

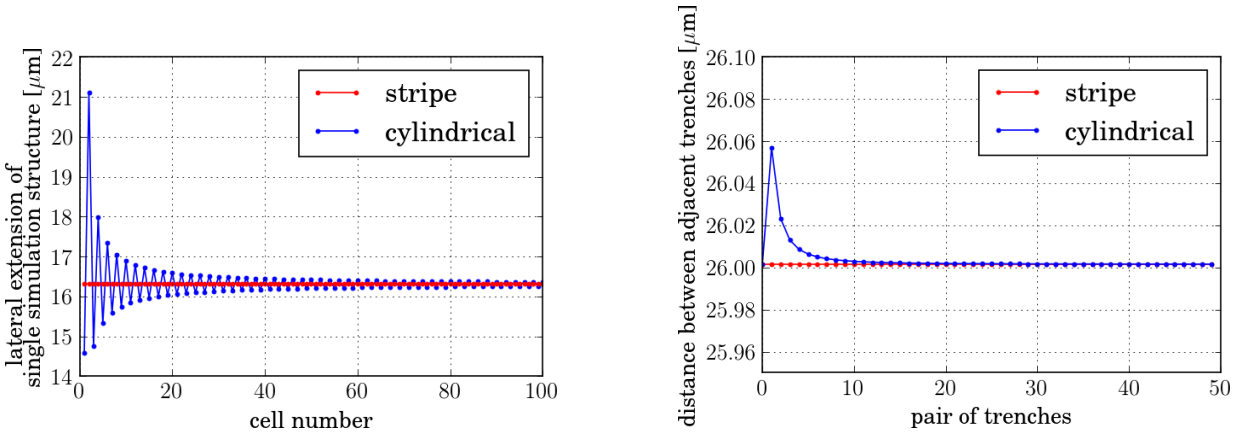

(a) (b)

Figure 4.5: (a) Comparison of lateral extensions of each cell of a monolithically integrated stripe structures (red) and monolithically integrated cylindrical structures (blue). Note that for large structures the cell dimensions approach the same lateral extensions. In both cases, the lateral extension of the trench itself is held constant. (b) The lateral distance between two adjacent trenches in both geometries. As can be seen the differences are at most 60nm and are thus negligible.

4.2 Stripe Geometry

The generation of monolithically integrated simulation structures in two-dimensional Cartesian geometry is based on the extension of a single simulation structure in this geometry. As was already mentioned in chapter 3, a single simulation structure can be viewed as an 'elementary cell' of the entire IGBT chip as long as every cell behaves the same. Beyond the limits of the safe-operating area this does not necessarily have to be the case any more, thus a redistribution of current density inside of the device has to be allowed for. In this geometry it can be achieved by consecutively mirroring a single simulation structure which basically leads to the situation depicted in Figs. 4.4a and 4.5a. The highest degree of homogeneity in the simulation can be achieved by consecutively mirroring not only the cell geometry itself but by mirroring the mesh as well. This, of course, includes doping profiles, electrical contacts, gate-resistances and work-functions inside of the gate-contact and leads to a 'best case' scenario in the simulation since no inhomogeneities are present in the simulation structure. (Thus, no inhomogeneities deriving from the fabrication process are considered.)
Furthermore, in the case of consecutive mirroring, no preferred direction of triangular-shaped discretisation elements is achieved. These measures reduce inhomogeneities inside of the device to the solver's level of numerical precision. In the course of mesh generation, special care is needed in the discretisation of the trench bottoms, since these regions exhibit a large curvature of the contacts which in turn can give rise to peaks in the electric field strength and, consequently, high impact ionization rates. A small mesh is also needed in the MOS-channel regions due to surface scattering at the interface between the bulk silicon and the oxide layer (degradation of electron mobility), as well as due to the small lateral extensions of the MOS-channels where a high gradient in electron current density is present in lateral direction.
The physical connection between the cells allows for electrical as well as thermal cross-talk and provides enough space for a filament in this geometry to fit inside of the simulation structure entirely as well as being a prerequisite for the movement of current filaments.
In addition to the monolithically integrated simulation structure and the discretisation itself, the boundary conditions which are imposed at the left and right edges are of importance in the numerical analysis. These boundary conditions were chosen to be of the homogeneous Neumann type. (Reference simulations show that choosing periodic boundary conditions has no influence on the limits of the safe-operating area as predicted by

simulation. Generally speaking, the influence of boundary conditions on the internal dynamics of carriers diminishes with increasing lateral extension of the simulation structure.)

4.3 Cylindrical Geometry

The generation of simulation structures in cylindrical geometry is, analogously to the generation of those in stripe symmetry, based on the constant ratio of contact areas and non-contact areas on the front-side of a single IGBT cell. In cylindrical symmetry, however, the generation of large simulation structures that consist of multiple IGBT cells, where each cell obeys the mapping criterion, makes it necessary to define the dimensions of each cell individually by an iterative process, which will now be described. Looking at Fig. 4.4b the following areas can be distinguished

$$A_{\mathrm{I,Chip}} = x^2 \tag{4.1}$$

$$A_{\mathrm{T,Chip}} = (x + 2z)^2 \tag{4.2}$$

$$A_{\mathrm{t,Chip}} = (2z + x)^2 - x^2 \tag{4.3}$$

$$A_{\mathrm{O,Chip}} = y^2 - (x + 2z)^2 \tag{4.4}$$

Here $A_{\mathrm{I,Chip}}$ denotes the 'inner' area enclosed by the trench-structure (not including the area of the trench itself), $A_{\mathrm{T,Chip}}$ denotes the area enclosed by the outer borders of the trench structure (i.e. including the area of the trench-structure). Furthermore $A_{\mathrm{t,Chip}}$ denotes the area of the trench-structure itself and $A_{\mathrm{O,Chip}}$ denotes the 'outer' area of the cell (i.e. the chip area between the trench-structure and the outer limits of the cell) of the real chip geometry. For odd-numbered cylindrical cells ($i = 1, 3, 5, 7, ...$) with

$$\alpha_n \equiv \sum_{k=1}^{n} (r_k + w + d_k) \tag{4.5}$$

(note that $\alpha_0 \equiv 0$). The general expressions for the respective areas are

$$A^{(i)}_{\mathrm{I,Sim}} = \pi \cdot \left[(\alpha_{i-1} + r_i)^2 - \alpha_{i-1}^2\right] \tag{4.6}$$

$$A^{(i)}_{\mathrm{T,Sim}} = \pi \cdot \left[(\alpha_{i-1} + r_i + w)^2 - \alpha_{i-1}^2\right] \tag{4.7}$$

$$A^{(i)}_{\mathrm{t,Sim}} = \pi \cdot \left[(\alpha_{i-1} + r_i + w)^2 - (\alpha_{i-1} + r_i)^2\right] \tag{4.8}$$

$$A^{(i)}_{\mathrm{O,Sim}} = \pi \cdot \left[\alpha_i^2 - (\alpha_{i-1} + r_i + w)^2\right] \tag{4.9}$$

For even-numbered cylindrical cells ($i = 2, 4, 6, 8, ...$) the general expressions for the respective areas are given by

$$A^{(i)}_{\mathrm{I,Sim}} = \pi \cdot \left[\alpha_i^2 - (\alpha_{i-1} + w + d_i)^2\right] \tag{4.10}$$

$$A^{(i)}_{\mathrm{T,Sim}} = \pi \cdot \left[\alpha_i^2 - (\alpha_{i-1} + d_i)^2\right] \tag{4.11}$$

$$A^{(i)}_{\mathrm{t,Sim}} = \pi \cdot \left[(\alpha_{i-1} + d_i + w)^2 - (\alpha_{i-1} + d_i)^2\right] \tag{4.12}$$

$$A^{(i)}_{\mathrm{O,Sim}} = \pi \cdot \left[(\alpha_{i-1} + d_i)^2 - \alpha_{i-1}^2\right] \tag{4.13}$$

This leads to the measures of a simulation structure for odd-numbered cells:

$$r_i = -\alpha_{i-1} + \beta + \sqrt{\beta\,(\beta + w) + \alpha_{i-1}^2} \tag{4.14}$$

$$d_i = -\left(\alpha_{i-1} + w + r_i\right) + \sqrt{\gamma\left[(\alpha_{i-1} + r_i)^2 - \alpha_{i-1}^2\right] + (\alpha_{i-1} + r_i + w)^2} \tag{4.15}$$

where for convenience β and γ are defined as

$$\beta \equiv \frac{w A_{\mathrm{I,Chip}}}{A_{\mathrm{T,Chip}} - A_{\mathrm{I,Chip}}} \tag{4.16}$$

$$\gamma \equiv \frac{A_{\mathrm{O,Chip}}}{A_{\mathrm{I,Chip}}} \tag{4.17}$$

The measures of the simulation structure for even-numbered cells are given by

$$d_i = -\alpha_{i-1} + \delta + \sqrt{\delta\,(w + \delta) + \alpha_{i-1}^2} \tag{4.18}$$

$$r_i = -\left(\alpha_{i-1} + w + d_i\right) + \sqrt{\epsilon\left[(\alpha_{i-1} + d_i)^2 - \alpha_{i-1}^2\right] + (\alpha_{i-1} + d_i + w)^2} \tag{4.19}$$

where δ and ϵ are defined as

$$\delta \equiv \frac{w A_{\mathrm{O,Chip}}}{A_{\mathrm{t,Chip}}} \tag{4.20}$$

$$\epsilon \equiv \frac{A_{\mathrm{I,Chip}}}{A_{\mathrm{O,Chip}}} \tag{4.21}$$

With this approach simulation structures consisting of any number of individual cells can be generated, enabling the investigation of large phenomena like current filaments and their relation to device latch-up. The practical realization of this approach was done using a self-developed tool written in the Python programming language [36].
The exact lateral extensions of each simulation structure within the monolithically inte-

grated cell is depicted in Fig. 4.5 along with a comparison of the measures of the stripe structure. As can be expected, both approaches give similar results for structures that consist of a high enough number of individual cells. Notably, the distance between two neighbouring trenches is nearly the same in both approaches, differing at most by about 60 nanometers which can be seen in Fig. 4.5b.
A comparison of the real chip layout and the simulation structure in the respective geometry is given in Fig. 4.4. From this it is obvious that under certain circumstances a cylindrical structure can give a quasi-3D and, hence, more realistic approximation of the filamentary current flow and the resulting critical phenomena in real-world IGBT-chips, which provides the basis for the quantitative numerical analysis of the latch-up threshold. For ease of comparison, the overall total active area of the simulation structure is held constant. Consequently, these structures only differ by their number of individual cells as well as by their lateral extension. Both features, on the one hand, facilitate a more pronounced redistribution of the current densities and, on the other hand, provide a structure that is large enough to fully comprise a single current filament, regardless of the symmetry type of the simulation domain. A justification and detailed explanation of this approach will be given in chapters 5 and 6, where the transient turn-off process in both simulation geometries will be discussed.

4.4 Calculation of Current Densities at Contacts

In order to compare the simulation results with experimental data, a criterion for the calculation of electrical current densities, which is independent of the simulation symmetry, is needed. To this end, physical quantities, which are accessible in both experiment and simulations, are needed. The current through the entire chip can be measured experimentally and the active area of the chip is known. Both can be combined to give a mean current density at the collector contact of the entire device. Especially the initial current density of the IGBT before the turn-off process can be determined this way in experiment and in the simulation alike. This mean current density forms the basis for the quantitative analysis of the over-current turn-off capability and thus the investigations of the safe-operating area of the device. Furthermore, this criterion is independent of the simulation geometry in use, and gives a universal quantity for the comparison of theory and experiment.
In the simulation itself a more sophisticated view of the current density distribution inside of the device is accessible as the currents through each individual cell can be determined.

The mean current density of each cell can be calculated which in turn opens a wider range of possibilities for the investigations of the relevant physical effects as local current densities can be considerably higher than the mean current densities at the contacts in the case of a filamentary current flow. This becomes especially relevant in determining the threshold current densities at the individual emitter contacts in case of an emitter side injection of electrons.
The geometrical mapping procedure described in this chapter assures a homogeneous current density distribution in the case of cylindrical symmetry, which is fundamental in the case of transient turn-off simulations. This ensures that the initial current density before device turn-off is homogeneous.

5. Simulation of Transient Turn-Off Process: Stripe Geometry

This chapter aims at investigating the latch-up effect in IGBTs which may occur during a turn-off process and leads to device failure eventually. Hence, this effect poses restrictions on the safe-operating area, especially what the device's capability to turn-off high current loads is concerned, which is the central point of investigation in this thesis. High current loads refers to an initial current through the device-chip that is above the nominal current. For power semiconductor devices that have, like IGBTs, a high on-state conductivity, the turn-off process is critical due to the extraction of the electron-hole plasma located inside of the base layer.
In the present work, the focus lies on the investigation of the latch-up process by means of a physics based numerical analysis that aims at approximating the real-world phenomena by simulating the turn-off process by means of a transient mixed-mode calculation.
The latch-up effect itself is closely linked to the effect of current filamentation during device turn-off, since only these filaments can exhibit current densities that are high enough to trigger this failure mechanism. Hence, a simulation that approximates the current densities inside a current filament as closely as possible is desired to reproduce measured data of device failure.
Current filamentation is directly linked to the latch-up effect: device latch-up is always preceded by current filamentation whereas current filaments do not necessarily trigger device latch-up as was discovered in [6, 37, 7, 38, 39, 8] as well. This chapter is based on [40].

5.1 Simulation Approach

The main goal of this section is to describe how processes that lead to the limitation of the safe-operating area can be simulated, aiming to reproduce the real situation in three

dimensional IGBT cells as closely as possible. The focus lies on the temporal behaviour of current densities inside of the device. To this end, a closer look at physical quantities like current densities, electric fields, carrier densities, lattice temperature and impact ionization, which govern the current transport inside of the device, is taken.
Special focus lies on the approximation of the real three dimensional current densities by using stripe symmetry. Investigating the turn-off processes lays the foundation for the analysis of this physical effect.
For simulating the transient turn-off behaviour, the simulation approach that is described in the following was chosen. The simulation features a turn-off process from a certain load current that can be chosen according to the investigations conducted. In addition to the current load, a DC-link voltage U_{DC}, a stray inductance L_σ, a free-wheeling diode D_{F} and gate resistances R_{G}, $R_{\mathrm{G},2}$ are contained within the electrical circuit depicted in Fig. 5.1 for the mixed-mode simulations. The IGBT chip being tested here is considered as a parallel

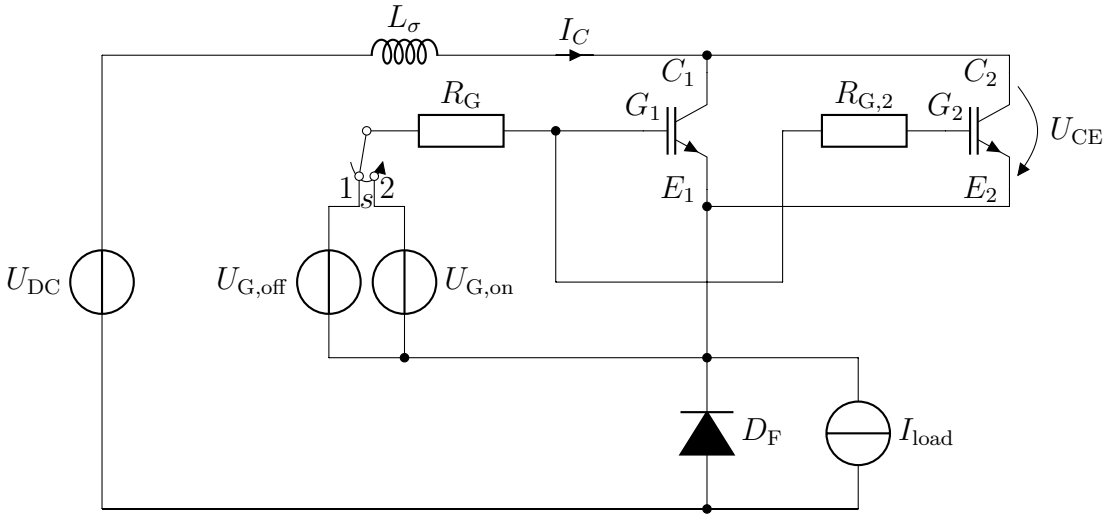

Figure 5.1: Sketch of electric circuit used in transient turn-off simulations. The entire IGBT chip is regarded as a parallel circuit of two separate simulation structures that are largely asymmetric in their active areas. Furthermore, the IGBT having the smaller active area is a monolithically integrated structure which potentially exhibits a filamentary current flow. Note, that in each simulation this ratio in active areas is held constant, independent of the number of individual cells forming the simulation structure. (This sketch is based on the one given in [1].)

circuit of two individual IGBT arrays which have a high asymmetry in their respective active areas. The larger structure has 99% of the total area and is formed by a single cell

in stripe geometry whereas the smaller structure has 1% of the total area and is the part of interest on the chip. This can be viewed as a zoom-in on the one percent of the total chip area that turns off last and exhibits current filamentation. Furthermore, the smaller structure is modelled as a monolithically integrated structure which consists of a multitude of cells. The generation of these structures was already described in chapter 4.
The approach of viewing a single IGBT chip as a parallel circuit was chosen for two reasons: first in order to simulate current crowding and fast transfer of current from the big to the small structure. And Second to be able to put an additional gate resistance in front of the small structure in order to simulate an additional asymmetry, i.e. an additional delay in the closing of the MOS-channels of the small structure, thus favouring current filamentation.
In isothermal simulations the lattice temperature is held constant across the entire device, thus neglecting local heating effects due to Joule or recombination heating. Hence, a gradient in temperature can not exist in this type of simulations. In electro-thermally coupled simulations the lattice temperature is regarded as a dynamical variable, evaluated at each point in time and every grid point. Thus a local change in temperature due to heating effects can occur and, as a consequence, effects that arise due to a non-homogeneous temperature distribution can exist. Furthermore, thermal boundary conditions are applied at the back-side (collector-side) of the device which are specified by an initial lattice temperature (which was always chosen to be the initially homogeneous device temperature of $T = 423\text{K}$) as well as a thermal resistance chosen according to values taken from the IGBT data sheet [2].
The duration of the turn-off process itself is mainly determined by the large structure which is the same in each simulation and allows for better comparability of the results. In order to investigate device latch-up, the operating conditions are chosen such that this effect is favoured, i.e. high lattice temperatures and small gate resistances.
The boundary conditions at the vertical edges of the simulation structures are chosen to be of the homogeneous Neumann type.

5.2 The Turn-Off Process

The initial conditions for the IGBT before the beginning of turn-off are characterized as follows: the DC-link voltage source is at 1.8kV and the current source at the desired load current for the respective turn-off simulation. The gate-emitter voltage is high enough

to fully conduct the load current which is identical to the sum of the collector currents of the large structure (IGBT 1) and the small structure (IGBT 2). Usually this voltage amounts to 15V in the conducting state for currents below the nominal current. For the investigation of over-current phenomena gate-voltages of up to $U_{\mathrm{GE,on}} = 90\mathrm{V}$ were needed. Furthermore, it is known from experiment that the initial state has to have a homogeneous distribution of current density, as well as of lattice temperature. These conditions have to be fulfilled in each simulation.

The turn-off is defined as the switch in gate-emitter voltage from +90V (in any case high enough to conduct the load current) to -15V (see Figs. 5.1).

During the first part of turn-off the gate-emitter voltage falls steadily. At one point in time, the gate-emitter voltage drops below the threshold voltage of the MOS-channels, which subsequently stop conducting. (Due to the additional gate resistance in front of the smaller structure, the closure of the MOS channels is slightly delayed, leading to more pronounced current crowding.) The current transport inside of the IGBT now derives from an extraction of the electron-hole plasma which is located in the intrinsic layer of the device, leading to a space-charge region which starts to develop on the trench-side. An electrical field exists inside of this region which increases in strength as the extraction of the electron-hole plasma continues. Originating from the build-up of a space-charge region, the collector-emitter voltage starts to rise. At one point, the field gets high enough to trigger impact-ionization at the trench bottoms. This phenomenon is commonly referred to as dynamical avalanche, and is at first the same for each cell within a monolithically integrated stripe structure. Due to the cell design the current density distribution at that point is slightly inhomogeneous, yet periodic. These inhomogeneities are restricted to the upper part of the structure and do not extend into the electron-hole plasma (cf. Fig. 5.2). Then, symmetry breaking occurs and (one or more) current filaments are formed, having a highly pronounced current density and, in electro-thermally coupled simulations, leading to a considerable increase of lattice temperature locally due to Joule heating. This symmetry breaking depends on the size of the simulation structure because in larger structures current densities can be distributed in more ways than in smaller structures. No differences in isothermal and electro-thermally coupled simulations are present up to that point.

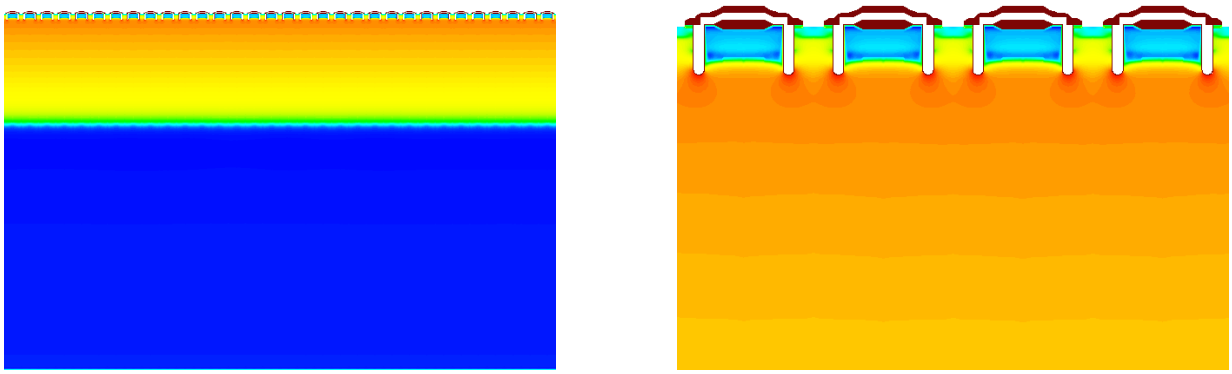

(a) (b)

Figure 5.2: Electric field strength (logarithmic scaling) in the entire device and in a detailed view. A locally increased field strength at each trench bottom is clearly visible. In these regions, impact ionization takes places which leads to the formation of current filaments. (a) view of the entire structure, the space-charge region is clearly visible; (b) detailed view of the front side of the simulation structure. The color-range extends from blue (10V/cm) to red ($5{\cdot}10^5$ V/cm).

5.3 Origin of Current Filaments

At the instance of symmetry-breaking during turn-off, one or several current filaments (depending on the number of cells within an integrated simulation structure) may originate from the impact ionization at the trench bottoms. The location of their origins depends on the homogeneity of the simulation structure itself. For the analysis of the transient turn-off behaviour, the simulation structures used were, from a simulation point of view, made as homogeneous as possible (see chapter 4). For the determination of the limits of the safe-operating are, this can be considered as a best-case scenario, since no latch-up due to severe inhomogeneities inside of the chip occurs. Hence, these current filaments arise purely from numerical errors of the solver that was used in the transient calculations. This leads to a statistical rather than a systematic distribution of filaments.
The connection to real-world filaments inside an IGBT chip can be drawn by the obvious assumption that no IGBT chip is perfect in a sense that each cell within an array of several hundred-thousand cells resembles every other cell exactly. Deviations among the cells will always exist due to an imperfect fabrication process. In a 'best-case' scenario, however, cells may be nearly the same. However any difference distinguishes one cell from the others and leads to an asymmetry which can trigger the nucleation of an inhomogeneity in current

density, i.e. a current filament. Among the features that distinguish the cells are different gate resistances, doping inhomogeneities, different work functions at the gate contacts, differences in gate-oxide thickness or variations in gate contact curvatures. Any of these features can cause one cell to be the 'weakest' cell which turns-off last, thus gathering a high amount of current which leads to local current inhomogeneities.
For completeness: in simulations filaments can be triggered by placing inhomogeneities in a cell, which dominate over numerical inhomogeneities arising from the solver used in transient simulations. Even small irregularities in, i.e. gate-resistance, work function or doping concentrations, are sufficient to get the desired effect. The physical features of the filaments are the same, independent of what causes them. In cases where a severe inhomogeneity is placed in the simulation structure, this inhomogeneity might be large enough to hold the filament at the same place until the device fails. This is not the case for filaments that are triggered numerically in a simulation structure where each cell resembles the other cell exactly within the same structure. In experiments, a reasonable homogeneity of the cells inside a chip can be assumed: if one or several cells within the same chip are significantly weaker than the other cells, the chip itself would be weaker than other similar chips and would not be able to withstand the same over-current turn-off processes.
The geometric shape of the lower part of the gate contact, which is close to a semi-circle, leads to a high peak in field strength (see Fig. 5.2). During turn-off the *pn*-junction between *p*-body and the n^--epitaxial layer is reverse biased and can hence exhibit high field peaks and impact ionization as well. Compared to the impact ionization rate which is located at the trench bottoms, this only plays a minor role. Furthermore, filaments do not originate from this junction.

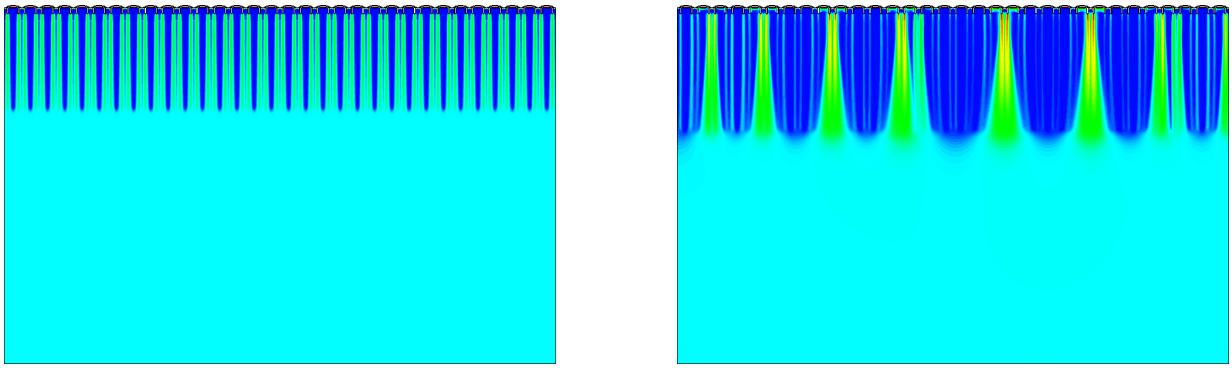

(a) (b)

Figure 5.3: Distribution of electrical current density during the turn-off process of a simulation structure consisting of 64 cells. The origination of current filaments is shown shortly before (a) and after (b) symmetry breaking. A statistical distribution of nearly equidistant current filaments with increased current densities is visible. The vertical extension of the filaments is equal to the vertical extension of the space-charge region. The time difference between instances (a) and (b) amounts to 120ns.

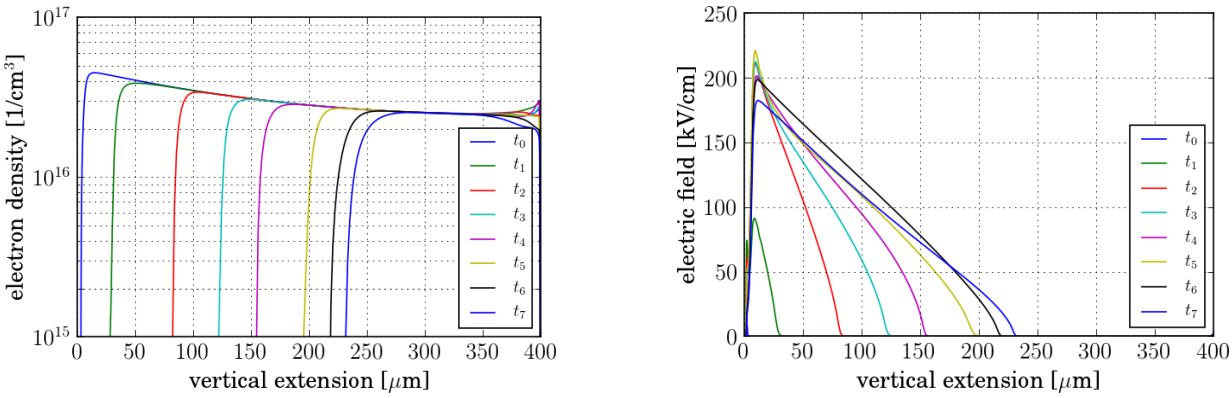

(a) (b)

Figure 5.4: Vertical extension of the electron-hole plasma as well as the space-charge region as a function of vertical extension and time inside a simulation structure consisting of 64 cells for electro-thermally coupled calculations. Electron density (a), strength of electric field (b) along the same cut-line.

5.4 Evolution of Current Filaments

After origination, a single current filament collects nearly the entire current of its ten nearest neighbours, leading to a pattern of approximately equidistant filaments for large simulation structures that can host multiple filaments. In vertical direction, at each point in time the length of the filaments is the same, since filaments evolve due to high electric fields in the space-charge region which itself has the same vertical extension over the entire simulation structure. As the space-charge region expands, the electron-hole plasma gets extracted and the vertical extension increases in the course of the turn-off process. In this way, the vertical extension of the current filaments is related to the collector-emitter voltage, which will be used in chapter 7 to investigate the features of current filaments by replacing the transient turn-off behaviour by a series of static IV-characteristics. As the filament grows, it gathers an increasing amount of charge carriers, which move at their respective saturation velocities due to the high electrical field in vertical direction. The distribution of carriers is spatially inhomogeneous. Hence, it gives rise to an electric field in lateral direction which is proportional to the carrier densities inside the filament. As the filament grows the basic composition of current densities remains qualitatively the same: electrons enter the filament from the front side due to dynamical avalanche at the trench bottoms (holes generated there move to the emitter due to the electric fields present in the device) and holes get extracted from the plasma. The major part of holes move to the emitter inside the filament(s) due to the high electric field, however, a minor amount of holes also moves across the space charge region towards the emitter. The lateral extension of a filament increases with larger vertical extensions due to diffusion processes, resulting in a focusing of holes on their way to the emitter and a de-focusing of electrons on their way to the collector. This leads to a trapezoidal shape in two dimensions.
At the emitter side, a current filament has a lateral extension of approximately the distance between two adjacent trenches, whereas at the collector-facing end the lateral extension of the filament increases during turn off, thereby leading to a more pronounced extraction of holes from the plasma. The filament itself reaches inside of the electron-hole plasma to a minor extent, leading to a small deformation of the plasma in the region of the filament. A small lateral component of the electric field is also present inside of the plasma directly beneath the filament, which collects holes and is directed towards the center of the filament.
The presence of filaments, however, does not lead to a significantly inhomogeneous current

flow at the back-side of the IGBT, since the plasma buffers the inhomogeneities deriving from filaments.

This evolution process is the same for isothermal and electro-thermally coupled simulations. In the latter case, however, temperature effects significantly influence the temporal behaviour of filaments during the turn-off process, leading to the occurrence of moving filaments. A closer description of the dynamics of filaments will be given in the following section.

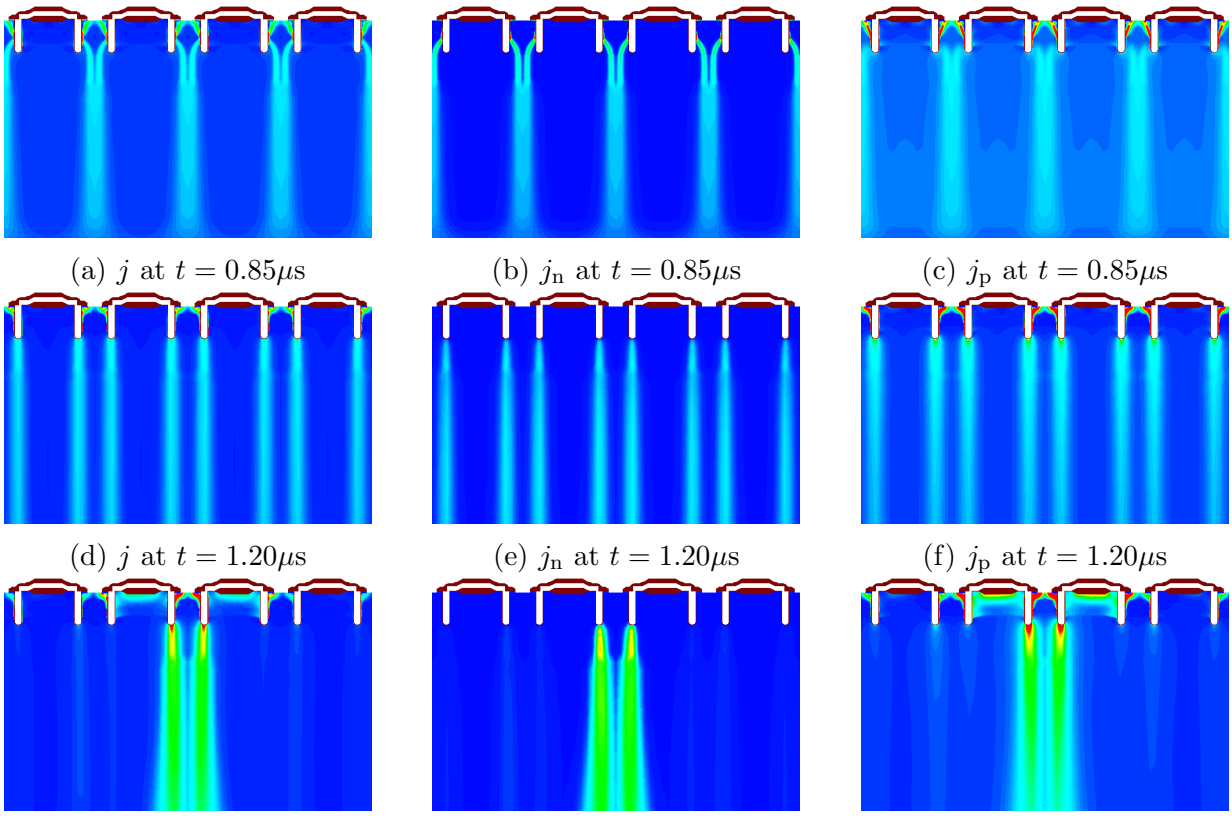

(a) j at $t = 0.85\mu$s (b) j_n at $t = 0.85\mu$s (c) j_p at $t = 0.85\mu$s

(d) j at $t = 1.20\mu$s (e) j_n at $t = 1.20\mu$s (f) j_p at $t = 1.20\mu$s

(g) j at $t = 1.26\mu$s (h) j_n at $t = 1.26\mu$s (i) j_p at $t = 1.26\mu$s

Figure 5.5: (a, d, g) total current density j, (b, e, h) electron current density j_n, (c, f, i) hole current density j_p at three different points in time (0.85μs, 1.20μs, 1.26μs) during the turn-off process. The transition from closing of MOS-channels to onset of dynamic avalanche and the formation of an individual current filament is visible. Detailed view of filament in 64 cell simulation structure from electro-thermally coupled calculations.

5.5 Dynamics of Current Filaments

Impact ionization at the bottom of each trench and especially at the bottoms of the two trenches where a filament originates is the driving force for filament growth. Yet, the high current densities cause, in electro-thermally coupled simulations, a local increase in lattice temperature which influences the impact ionization rate. As was already described in the physical models in chapter 2, the impact ionization rate decreases with increasing lattice temperature, which makes current filamentation a self-limiting process.
At the beginning of each electro-thermally coupled turn-off simulation, a start with a homogeneous temperature distribution at a specified initial value of 423K is chosen. The process then continues as described in the previous section up to the point at which the locally increased temperature reduces the impact ionization rate. As a consequence, the current densities inside a filament start decreasing because less electrons enter the filament from the trench-bottoms and less holes get extracted from the plasma. This is due to the diminished electrical field strength. This continues up to the point where the filament disappears entirely, leaving behind a locally restricted region beneath the trenches with higher temperature.
Due to the inductive load the overall current through the simulation structure does not drop instantly and new current filaments begin to form at trenches which have the lowest lattice temperature. 'Moving' is usually used to describe the dynamics that current filaments follow, yet it is a general term that does not precisely describe the dynamics. A more exact terminology for the dynamics would be: current inhomogeneities with restricted lifetime which can occur at different times at different places inside of the device for monolithically integrated IGBT simulation structures that consist of a multitude of single cells (cf. Figs. 5.6).
Obviously, the distribution of lattice temperature plays a crucial role in determining the dynamics of current filaments. A comparison of the lattice temperature distribution and the current densities along a lateral cut-line beneath the trenches can be seen in Fig. 5.7. Due to the initially homogeneous temperature distribution and the uniform heating at each trench the current densities at each emitter contact follow a nearly periodic behaviour at first. Periodicity gets lost with the occurrence of symmetry-breaking: every asymmetry that arises during the turn-off process is caused by the symmetry breaking of the electrical current density and the resulting filamentary current flow due to Joule heating. Thermal boundary conditions in electro-thermally coupled calculations are, as was already described

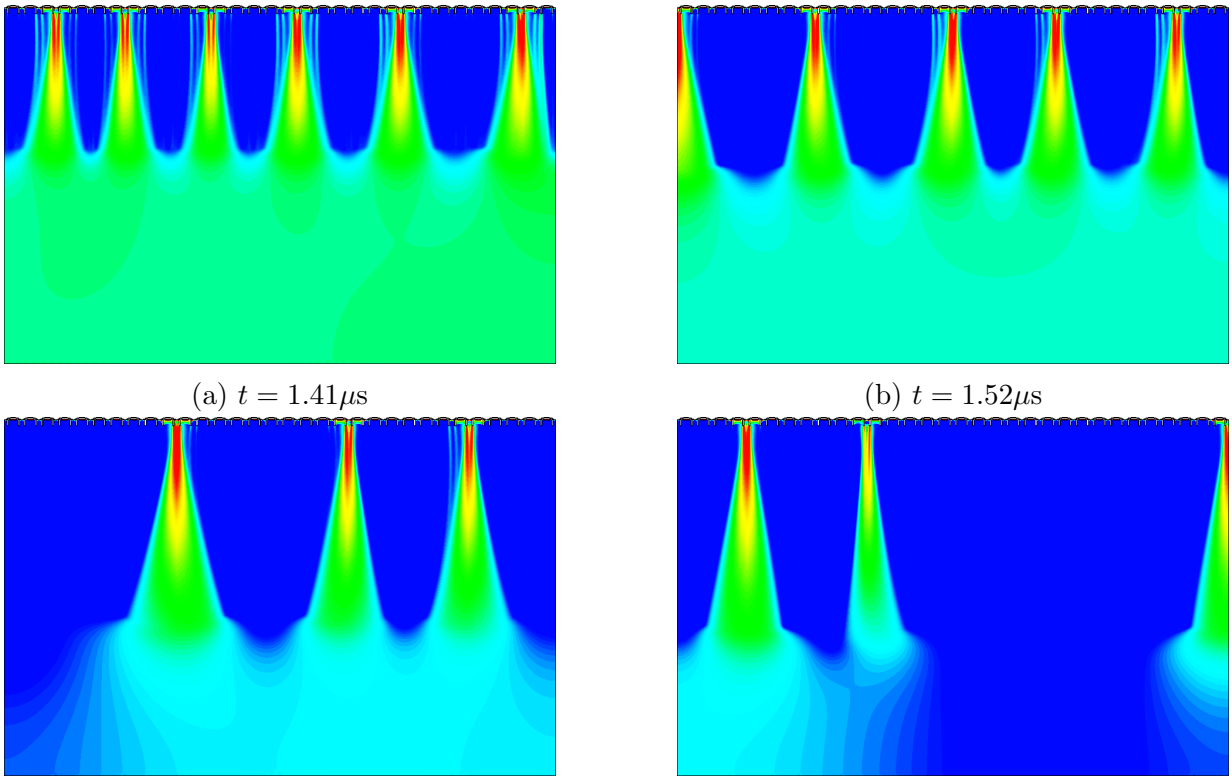

(a) $t = 1.41\mu$s (b) $t = 1.52\mu$s

(c) $t = 1.83\mu$s (d) $t = 1.97\mu$s

Figure 5.6: Two-dimensional view of the electric current density distribution in a monolithically integrated structure consisting of 64 cells. The pictures (a)-(d) give four different points in time during the same turn-off process for electro-thermally coupled calculations. The dynamics of the current filaments is clearly visible.

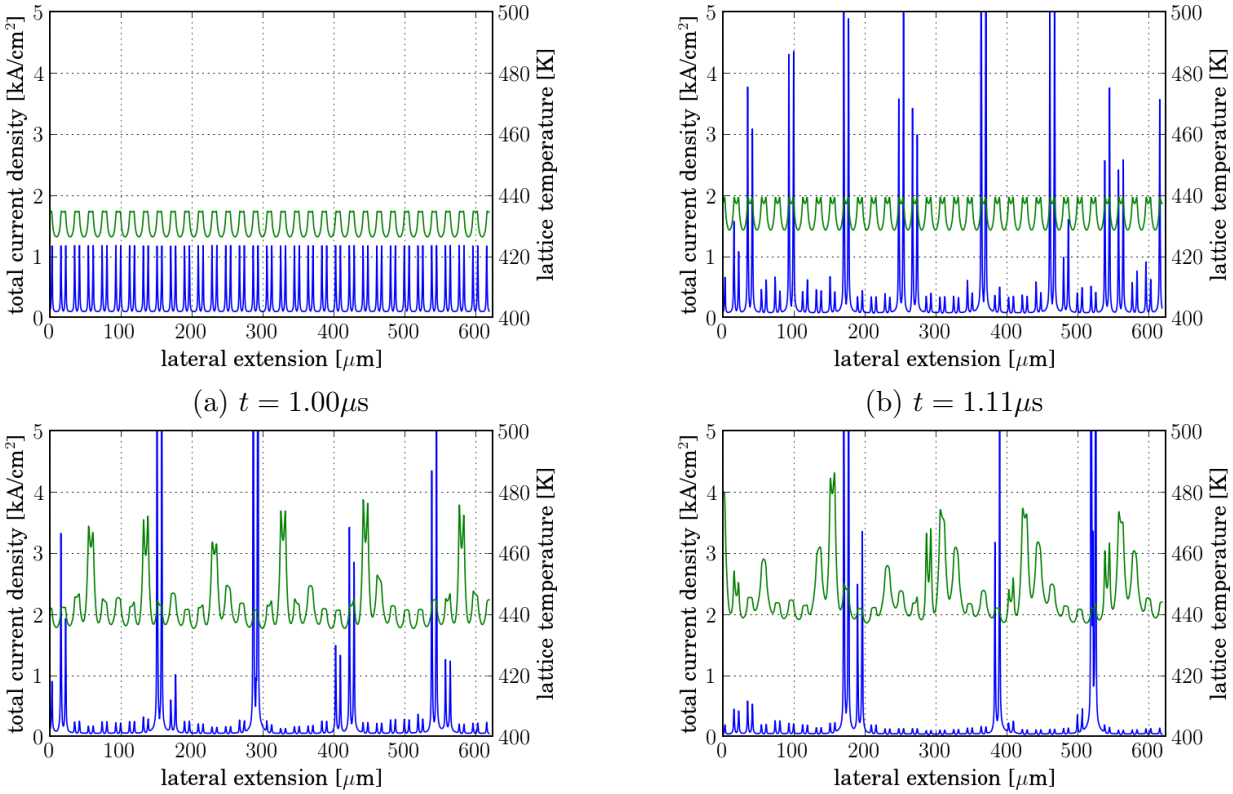

(a) $t = 1.00\mu$s

(b) $t = 1.11\mu$s

(c) $t = 1.46\mu$s

(d) $t = 1.63\mu$s

Figure 5.7: Gradient in temperature as driving force for movement of current filaments in stripe structures. Electro-thermally coupled simulations of a 64 cell structure in stripe symmetry at 4 different points in time during the turn-off process. The initial current density in this case amounts to 350A/cm^2.

in section 5.1, applied at the back-side of the device only, having a minor impact on the distribution of lattice temperature at the emitter side due to the large vertical extension of the device of 400μm. This thermal resistance at the collector contact is held constant as is the total area of the simulation structure, which facilitates comparability among structures with a different number of cells.

In simulations for identical structures with identical simulation parameters the current density distribution which forms during the turn-off process is the same, thus giving reproducible results. However, for a slightly changed initial current density, the distribution of current density is different which in turn leads to a different distribution in lattice temperature and, consequently, to different dynamics of the filaments (cf. Figs. 5.9 and 5.10). The influence of recombination heat on the temperature distribution can be neglected

since recombination processes mainly take place beneath the emitter contact in the contact hole between two trenches, which is remote from the regions where impact ionization and current filaments exist. In isothermal simulations, where the lattice temperature is held constant, current filaments show no dynamics at all (see Fig. 5.11).
At each point in time during the turn-off process current filaments are qualitatively the same concerned their constitution. Right from the nucleation of a filament, which always takes place at the bottom of a trench, the carriers are distributed inhomogeneously in lateral as well as in vertical direction. This leads to strong electric fields especially in lateral direction, which are located in a way that they focus holes coming from the collector side and de-focus electrons from the emitter side with respect to the center of the filament. A depiction of a typical current density distribution can be found in Figs. 5.8, which closely resembles the lateral distribution of the respective carriers since they move at their saturation velocities as a consequence of the high vertical component of the electric field. Qualitatively the constitution of a filament does not change in vertical direction as can be

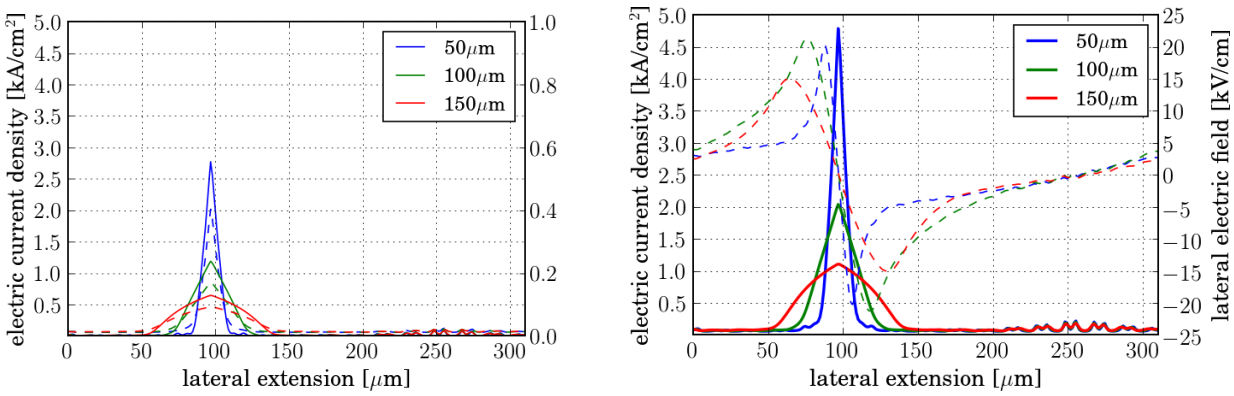

(a) (b)

Figure 5.8: (a) Constitution of a single current filament occurring during the turn-off process of a 32-cell stripe structure. The colours blue, green and red signify the vertical position of the lateral cut-lines. Solid lines give the electron current density whereas dashed lines give the hole current density. A spatially inhomogeneous distribution of carriers which in this case move at their respective saturation velocities is clearly visible. (b) The total electric current density (left y-axis) along the three different lateral cut-lines (color-coded solid lines) as well as the corresponding electrical field strength in lateral direction only. The inhomogeneous distribution of charge carriers gives rise to a strong electric field inside of the filament which exhibits a strong lateral as well as vertical component. Note also the wide range of the lateral electric field which can be viewed as a range of collection of holes from the electron-hole plasma.

seen in Fig. 5.8a. Inside most of the filament the electron current density exceeds the hole current density, only at the edges of the filament the hole current density is higher. This derives from the fact that holes basically move from the collector to the emitter side of the device not only inside a filament but at every lateral extension due to the orientation of the electric field. Electrons on the other hand can only move from the emitter to the collector side at every lateral extension they are generated due to impact ionization at the trench bottoms.

The constitution of a filament in lateral direction is qualitatively the same for every vertical extension up to the border between space-charge region and electron-hole plasma. There, the absolute value of the electric field gets lowered significantly by the excessive amount of equally distributed electrons and holes that form the plasma. However, the absolute value of the electric field does not drop to zero, leading to a weak electric field inside of the plasma in vertical as well as lateral direction directly underneath of a filament. These components cause the carriers inside of the plasma to move towards the filament. Therefore they are a fundamental part for the current filament dynamics as well as for the occurrence of latch-up since the hole current density at the emitter side is dependent on the amount of holes extracted from the plasma as well.

Quantitatively, the inhomogeneous distribution of charge carriers, which changes over time, strongly influences the range of the lateral component of the electric field. As can be seen in Fig. 5.8b the lateral range exceeds by far the lateral extension of a single simulation structure and can be as high as 350μm.

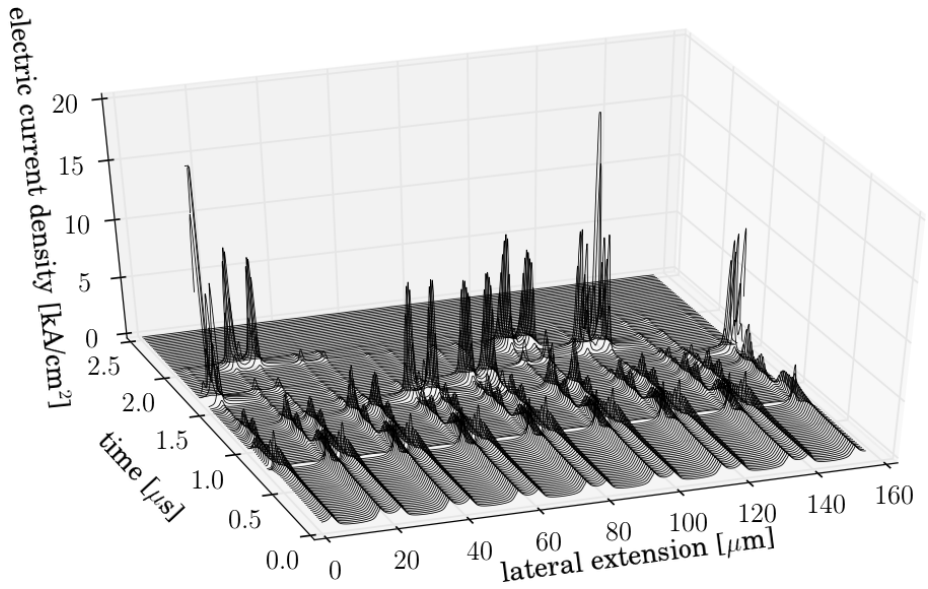

(a)

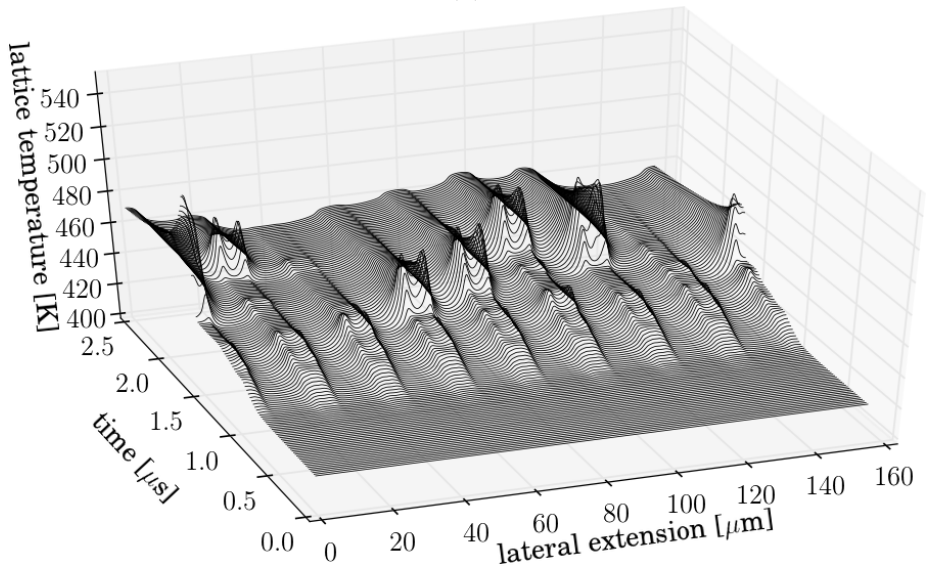

(b)

Figure 5.9: Transient electro-thermally coupled simulation of the turn-off process of a 16-cell stripe structure: consecutive lateral cut-lines directly beneath the trenches for several different points in time of (a) the electric current density and (b) the lattice temperature. The evolution and dynamics of moving current filaments is clearly visible. The initial current density is 400A/cm^2 and the turn-off time amounts to 2μs. The initially homogeneous temperature amounts to 423K. A rise in lattice temperature due to the evolution of moving current filaments is clearly visible. No latch-up occurs in this case.

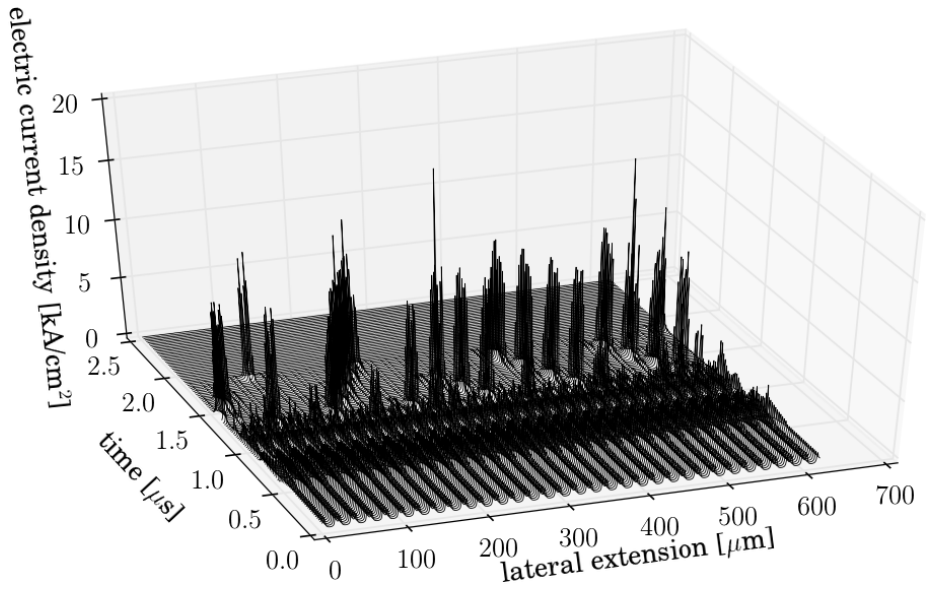

(a)

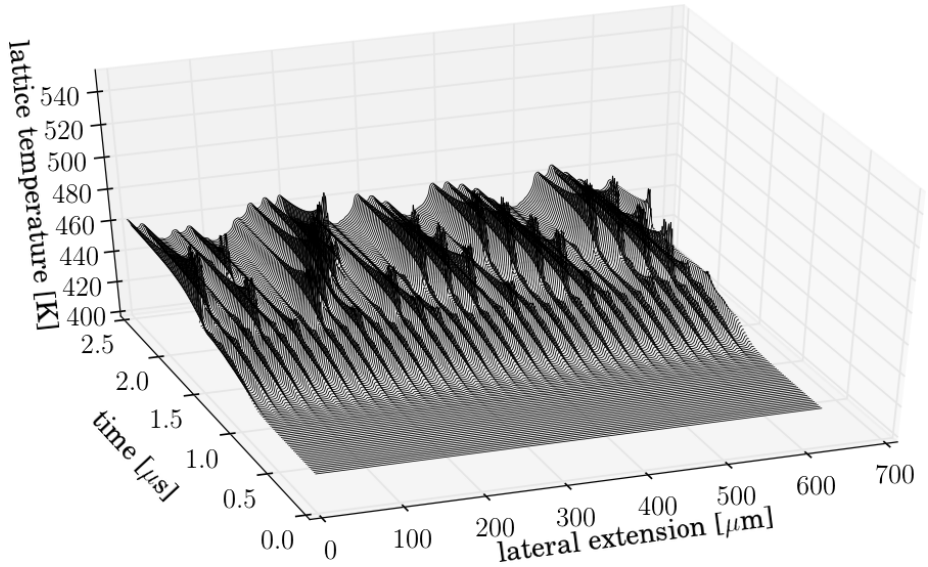

(b)

Figure 5.10: Series of lateral cut-lines directly beneath the trenches for a transient electro-thermally coupled simulation of the turn-off process of a 64-cell stripe structure. (a) depicts the electric current density and (b) the lattice temperature along the cut-lines. The initial current density amounts to 300A/cm^2 and the initially homogeneous lattice temperature to 423K. No latch-up occurs in this case.

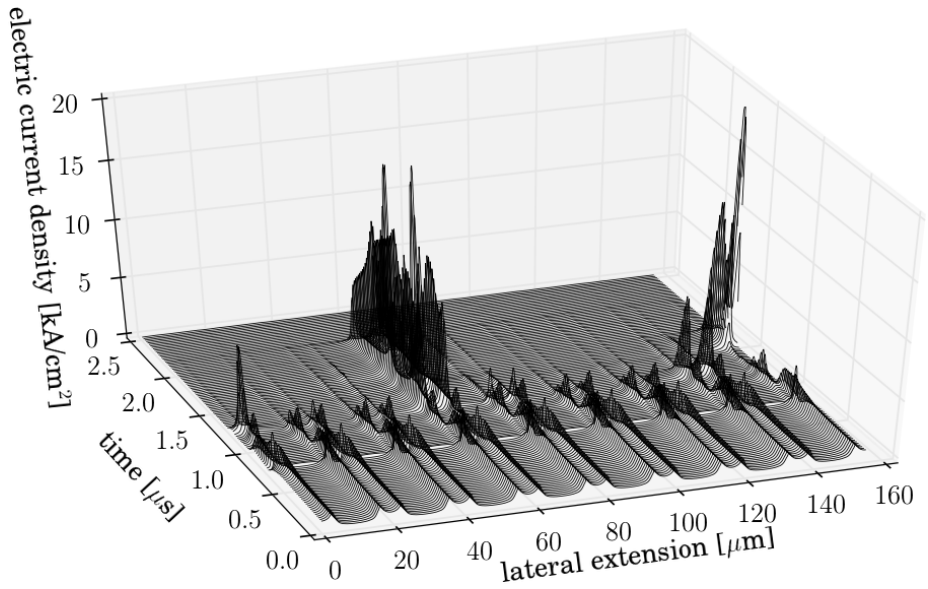

(a)

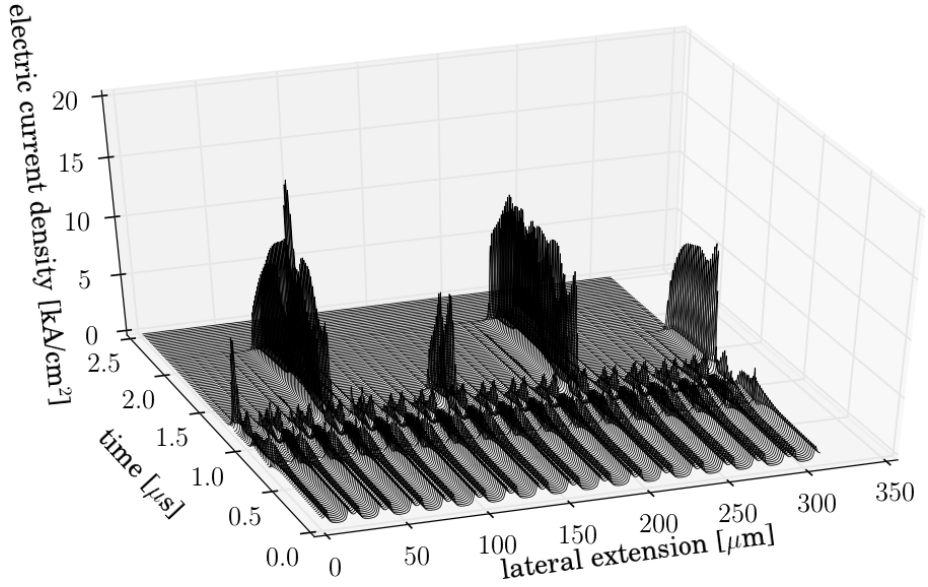

(b)

Figure 5.11: Electric current density beneath the trenches as a function of time for isothermal simulations. No moving current filaments occur in a 16-IGBT monolithic structure (a) and in a 32-IGBT monolithic structure (b) during turn-off. No latch-up occurs in both cases. The initial current density is 400A/cm^2 for (a) and 350A/cm^2 for (b).

5.6 Physical Processes Leading to Device Latch-Up

The existence of moving current filaments during the turn-off process does not inevitably cause the device to fail. In investigations it was found that non-destructive moving current filaments in electro-thermally coupled simulations of a 64-cell integrated IGBT structure in stripe geometry (cf. Fig. 5.13b) can attain a local current density of approximately 3kA/cm^2. This exceeds the density before turn-off by a factor of 10, without driving the device into the latch-up state. In integrated structures one can observe that all simultaneously existing current filaments are comparable in their current densities and, in the case of non-destructive filaments, remain at this level for a limited amount of time until the filaments' densities decrease as the overall current through the device approaches zero.
The edge of the safe-operating area is characterized by the occurrence of device latch-up, which is always preceded by the formation of (destructive) current filaments. These filaments have a slightly higher mean current density than non-destructive ones occurring just below the onset of latch-up. It was observed that in the course of device turn-off the mean current density in the existing filaments rises as the number of simultaneously existing filaments decreases. At one point during turn-off this can lead to device latch-up starting in a single IGBT cell. From there, latch-up spreads to the neighbouring cells.
A closer look at the mechanisms leading to the destruction of the IGBT due to device latch-up will be given in the following sub-section. In order to investigate the effect of device latch-up using the structures described, the usual (doping) measures against latch-up were not taken. The latch-up of IGBT cells is preceded by an injection of electrons at the emitter contact, i.e. from the source region to the body region (see Fig. 5.12a). The injection takes place after the MOS channels are closed and moving filaments exist in the device. (It is worth mentioning that during the turn-off process the gate voltage decreases continuously without rising, i.e. without opening the MOS-channels again.) At this time, an inhomogeneous current flow (which is visible in the currents flowing at the respective emitter contacts) arises, which consists of a significant amount of electron current (up to nearly 40% of the total current) in certain filaments. Looking at the electron current density at an arbitrary emitter contact as a function of time one can see that the electron current only becomes different from zero when it is above a threshold of hole current density. This leads to an injection of electrons into the device. A more detailed analysis of the electron and hole current peaks at the emitters reveals that the current peaks occur simultaneously (cf. Fig. 5.13b).

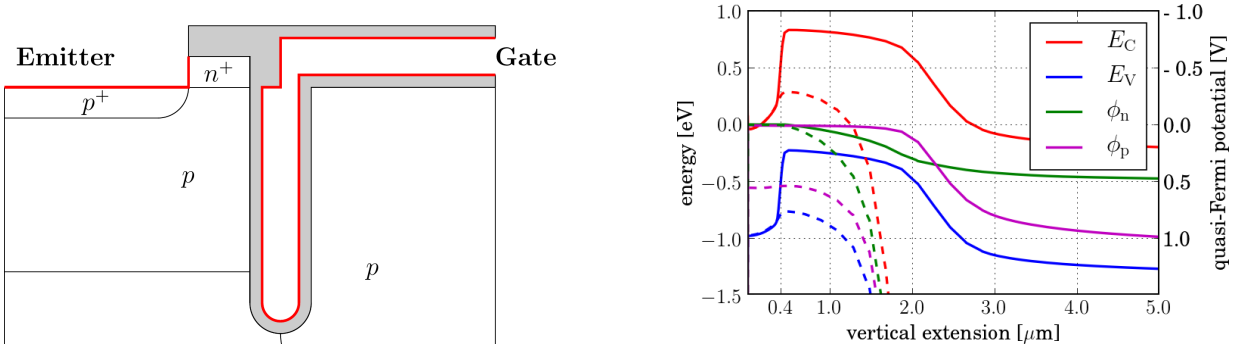

(a) (b)

Figure 5.12: Conduction band energy E_C, valence band energy E_V, electron quasi-Fermi level ϕ_n and hole quasi-Fermi level ϕ_p in a vertical, laterally central cut through the source-body *pn*-junction at two different time instances during turn-off: solid lines at $t = 0.00\mu$s, dashed lines at $t = 1.53\mu$s. The *pn*-junction is located at a vertical extension of 0.4μm in this plot. A schematic view of the cut-line through the trench-IGBT is given on the upper right-hand side: n-doped (p-doped) regions are depicted in red (green), the light blue line represents the emitter contact while the cut-line is given by the black line.

The threshold current density itself can be explained by a voltage drop at the source-body *pn*-junction occurring due to a highly increased number of holes moving laterally beneath the junction towards the emitter contact during turn-off. (Note that this junction is shorted rather effectively due to the cells' design.) A closer look at a vertical cut-line through the source-body *pn*-junction (Fig. 5.12a) as a function of time reveals a significant change in the dependencies of the band structure as well as the quasi-Fermi levels of the electrons and holes in the case of a moving current filament passing by (Fig. 5.12b). Initially, near the *pn*-junction the quasi-Fermi levels of electrons and holes are identical, whereas they differ significantly in the event of a moving current filament due to the excessive amount of holes flowing underneath the source. This forward biasing of the junction along with a still high collector-emitter voltage enables electrons from the source to pass the junction and to be emitted into the device. It is this electron current that, if it is high enough, causes the parasitic *npnp*-structure to latch, and eventually destroys the IGBT.
In Figs. 5.13, a different view of this effect is depicted: the electron current density at the emitter contact is plotted as a function of the respective hole current density using time as a parameter. From Fig. 5.13a the threshold current density can be read off to be around 1kA/cm^2 for this 16-cell structure, which is in agreement with the result for larger structures. (As can be expected, the threshold for electron injection is the same for each

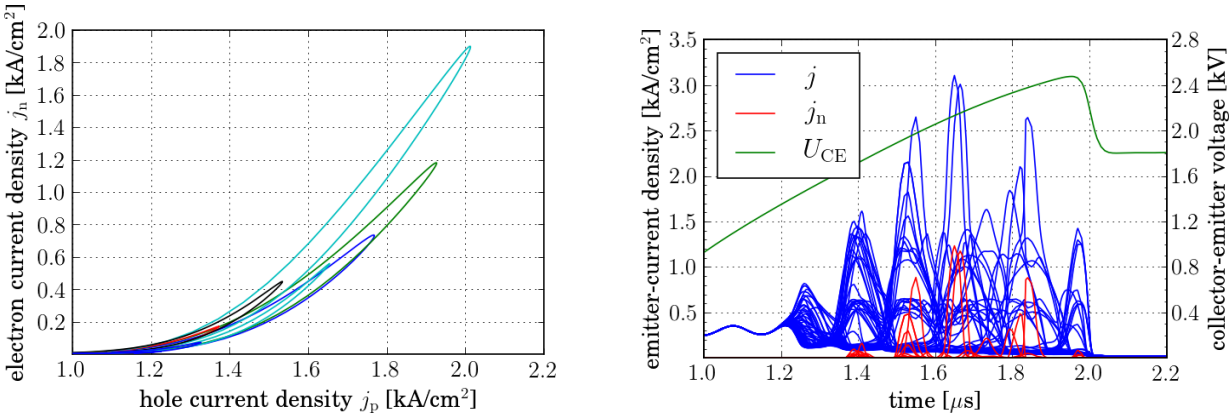

(a) (b)

Figure 5.13: (a) Electron current density as a function of hole current density for each (single cell's) emitter contact for a 16-IGBT integrated structure during the formation of moving current filaments during turn-off. These loops, which are a function of time, are run through in a counter-clockwise direction as time increases. The initial current density in this case is 400A/cm^2, which is slightly beneath the latch-up current density for a 16-cell structure. (b) Electric current densities j and electron current densities j_n at each (single cell's) emitter contact of a 64-IGBT integrated structure as a function of time (left y-axis) and the corresponding collector-emitter voltage U_{CE} (right y-axis). An injection of electrons during the appearance of (non-destructive) current filaments is clearly visible.

cell in a monolithically integrated simulation structure.)

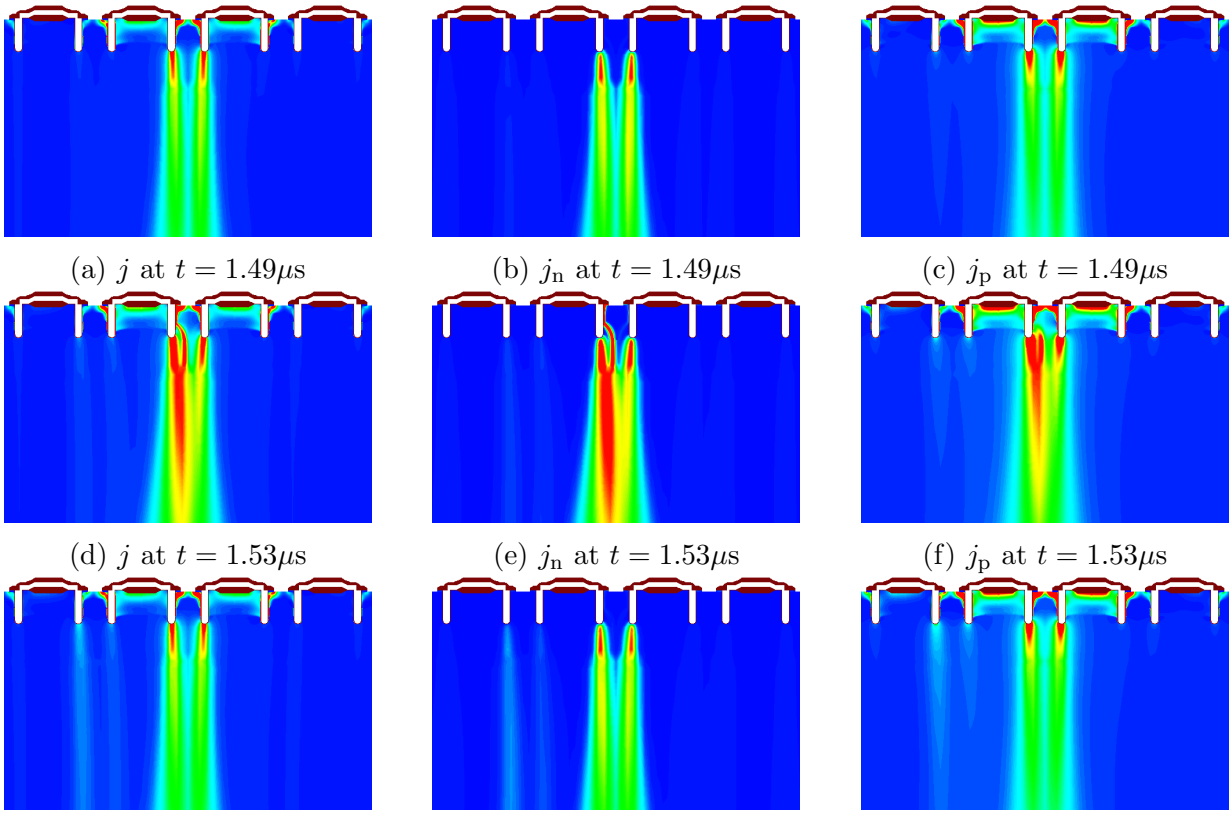

(a) j at $t = 1.49\mu$s (b) j_n at $t = 1.49\mu$s (c) j_p at $t = 1.49\mu$s

(d) j at $t = 1.53\mu$s (e) j_n at $t = 1.53\mu$s (f) j_p at $t = 1.53\mu$s

(g) j at $t = 1.57\mu$s (h) j_n at $t = 1.57\mu$s (i) j_p at $t = 1.57\mu$s

Figure 5.14: (a, d, g) total current density j, (b, e, h) electron current density j_n, (c, f, i) hole current density j_p at three different points in time (1.49μs, 1.53μs, 1.57μs) during the turn-off process at which an emitter-side injection of electrons into the device takes place. The figures are a detailed view of a single current filament in a 64 cell simulation structure using electro-thermally coupled simulations.

5.7 Limits of the Safe-Operating Area

As was already stated in section 5.6, the edge of the safe-operating area with respect to over-current turn-off is characterized by the occurrence of device latch-up, which in turn is always preceded by a filamentary current flow. Failure of the device is defined as the situation, when the entire current in the parallel circuit of the two highly asymmetrical IGBTs is taken over by the small (1%) structure. This definition applies to both electro-thermally coupled as well as isothermal calculations. In electro-thermally coupled simulations, however, this is usually preceded by a steep rise in lattice temperature up to the melting point of silicon. In the case of device failure, the constitution of a current filament changes

significantly due to the high injection of electrons from the emitter side, which leads to comparable densities of electrons and holes. Physically, latch-up of the IGBT is characterized by the formation of a stable plasma-channel which can be well distinguished from the filament state due to the high electric fields that are characteristic for filaments. A depiction of the formation of such a plasma-channel can be see in Fig. 5.16b. This process can be described as the turn-on of the parasitic thyristor inside of the IGBT. The current flow through the IGBT can no longer be controlled by the gate, leading to a steep increase in current densities which results in a rapid increase of lattice temperature and eventually to thermal destruction of the device. In isothermal calculations, the turn-on of the parasitic thyristor takes place in the same way, yet the formation of a plasma channel and the resulting high current densities do not lead to thermal runaway. This destruction mechanism is qualitatively the same for each lateral extension of the simulation structure. Yet, there are significant differences in what the initial current densities before the beginning of the turn-off process, which eventually lead to destruction of the IGBT. In Fig. 5.16a the case of latch-up of the same cell is depicted, showing a strong increase in both hole and electron current densities. The threshold current density remains the same in this case. Additionally, a second threshold current density at around $2\mathrm{kA/cm^2}$ exists. This derives from the latch-up of cells which are next to cells that are already in the latch-up state. In the case where the amount of electrons is too small to trigger latch-up, the slope of the electric field beneath the source is lowered due to the additional electrons coming from the emitter contact as was described in section 5.6. However, no stable (stationary) plasma channel forms and the decrease in slope of the electric field is limited to the duration of electron injection (cf. Fig. 5.13b).

Experimentally, the initial mean current density (i.e. the total current through the chip divided by the total active area of the chip) at which latch-up occurs in the course of the turn-off process, is significant. To this end, the limits of the safe-operating area, as they are discussed in this work, are quantitatively formulated with respect to this current density. In theoretical investigations, the initial current density that leads to device latch-up can only be determined to lie within a certain interval, since in transient turn-off simulations the result of a simulation can either be 'failed' or 'not-failed'. A current density which lies within this interval is then referred to as latch-up current density.

Hence, the lateral extension is a measure for how well a current filament fits inside the structure, since a filament itself has a fixed shape. The overall active area of the simulation structure is held constant, as was already mentioned in sub-section 5.1, to facilitate

comparison. Furthermore, a larger lateral extension of the simulation structure and consequently more IGBT cells give more possibilities for the current to redistribute inside the structure. For structures consisting of only a few cells, possibilities for redistribution of the current are rather limited. Symmetry breaking during the turn-off process along with large monolithically integrated structures are key for the simulation of latch-up. Without symmetry breaking, each cell behaves the same and no current crowding takes place. This would lead to a highly homogeneous (periodic) turn-off behaviour which in turn leads to a high latch-up current density. Moreover, in this case the latch-up current density would be independent of the lateral extension of the simulation structure.
As can be seen in Fig. 5.17 the latch-up current density exhibits a strong dependence on the lateral extension of the simulation structure. It was found that the latch-up current density strongly depends on the lateral extension of the simulation structure used, i.e. on the number of IGBT-cells that constitute the simulation structure. Although a limiting value of the latch-up current density is reached for large structures, it still over-estimates the robustness of the real IGBT chip (i.e. a chip with the usual measures against latch-up) by about a factor of 5, as shown by a comparison with experimental data. From a quantitative point of view this is clearly an unsatisfactory agreement as no predictive simulations are possible using the approach presented in this section. This suggests that the approach using stripe geometry is too crude an approximation to the real filament geometry and an alternative approach is needed. This approach will be presented in the next chapter.

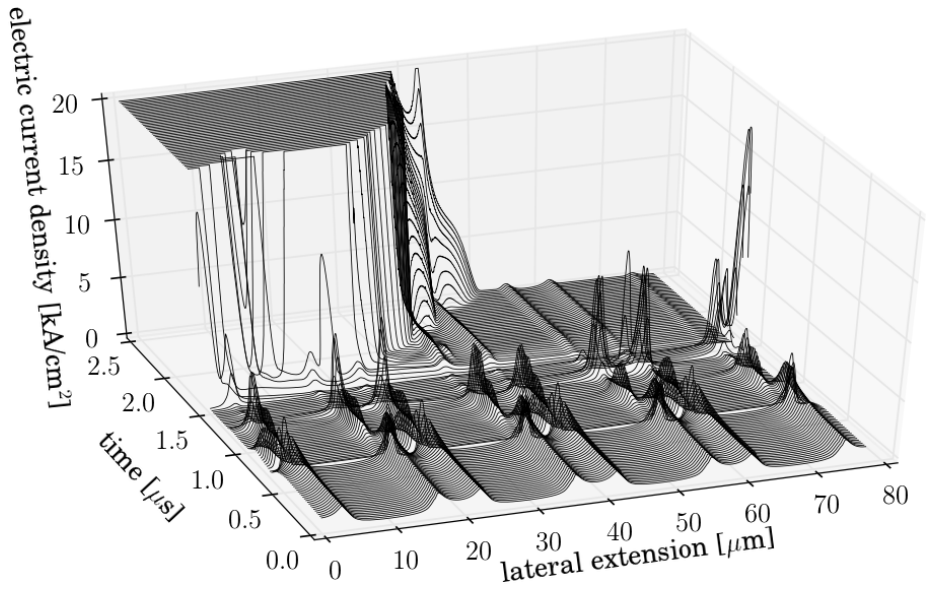

(a)

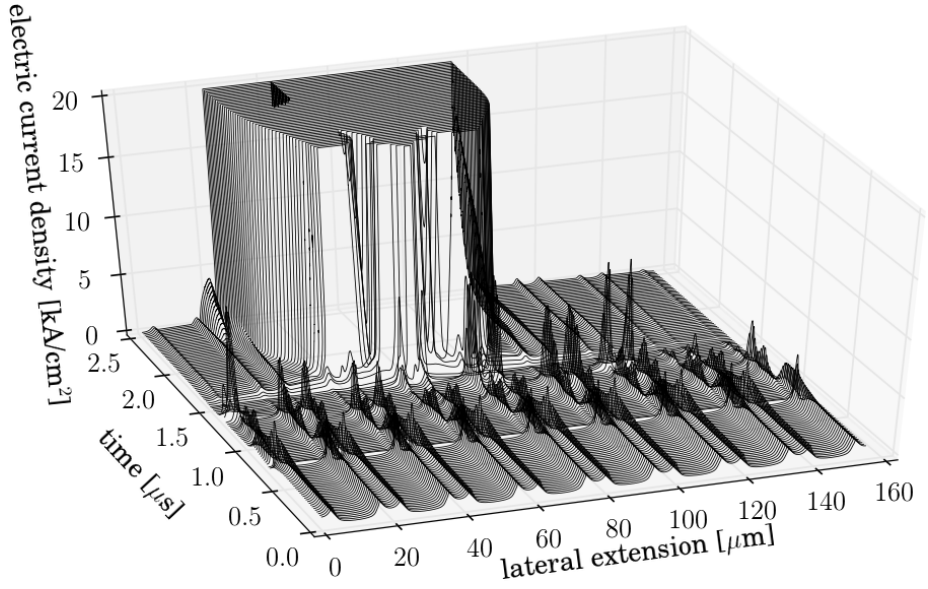

(b)

Figure 5.15: Electric current density beneath the trench cells as a function of time during the latch-up process in an integrated structure (a) consisting of 8 IGBT cells and (b) consisting of 16 IGBT cells. The latching of the cells is clearly visible. The initial current density amounts to 600A/cm^2 for (a) and 500A/cm^2 for (b).

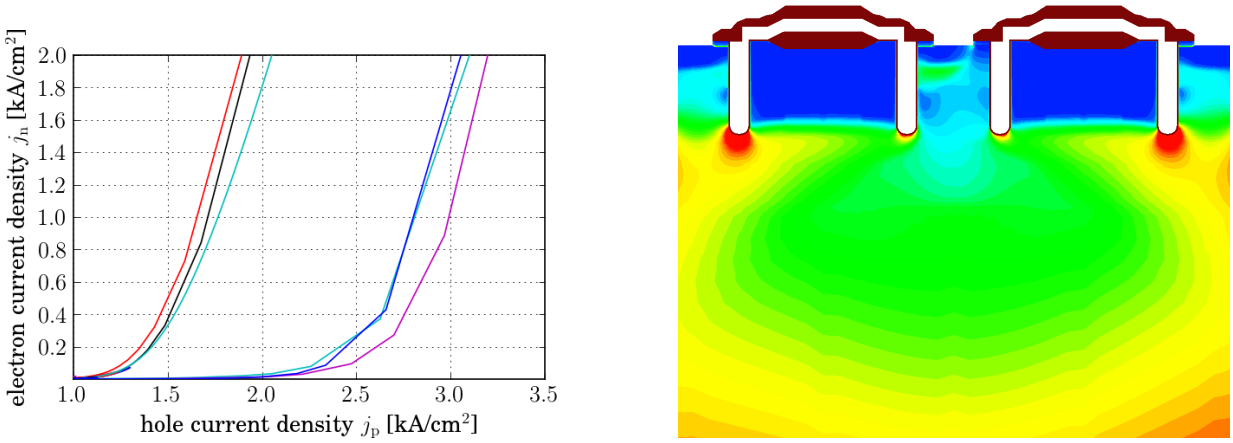

(a) (b)

Figure 5.16: (a) Electron current density as a function of hole current density for each (single cell's) emitter contact for a 16-IGBT integrated structure during latch-up (dashed lines), which occurs approximately at $t = 1.40\mu$s. The initial current density in this case is 500A/cm^2 , which is slightly above the latch-up current density for a 16-cell structure. (b) The strength of the electric field at the onset of device latch-up. A drop of field strength underneath the contact hole, which results in the formation of a plasma-channel, is clearly visible. This is a detailed view into the simulation structure of the situation depicted in (a).

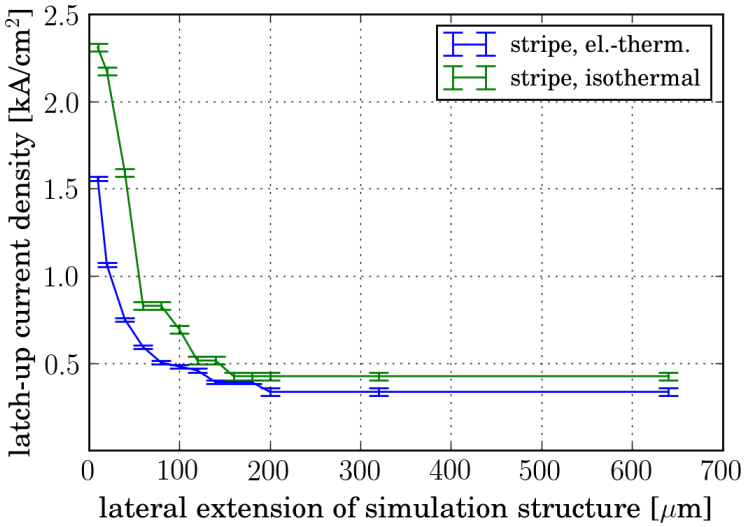

Figure 5.17: The latch-up current density as a function of the number of cells in an integrated structure for both isothermal and electro-thermally coupled simulations. The latch-up current density exhibits a strong dependence on the number of cells for structures consisting of only a few IGBT-cells and reaches a limiting value for structures consisting of a large number of cells.

5.8 Comparison of Isothermal and Electro-Thermally Coupled Simulations

If structures consist of a sufficiently large number of IGBT cells, i.e. if their lateral extension is large enough to entirely comprise a single current filament, the quantitative difference in the current densities leading to device latch-up are comparable for both types of simulations as can be seen in Fig. 5.17. Furthermore, the simulation approaches have in common that the injection of electrons from the source to the body region eventually leads to the latch-up of the *npnp*-structure. This is the failure mechanism which characterizes the limits of the safe-operating area. The number of co-existing filaments, the constitution of filaments, the lateral electric field and the extraction of holes from the plasma is in good agreement for the two types of simulation.
Qualitatively, however, a comparison of isothermal and electro-thermally coupled simulations of current filaments shows a substantial difference in the processes leading to destruction of the device: current filaments do not move in simulations with constant temperature, as a gradient in temperature is the driving force for triggering filament movement. Also the effect of a locally increased lattice temperature, which in turn increases the intrinsic carrier densities, is not taken into account in isothermal simulations.

6. Simulation of Transient Turn-Off Process: Cylindrical Geometry

As was discussed in the previous chapter, the approach using 2-dimensional Cartesian coordinates has several shortcomings regarding an exact approximation of real-chip current filaments. Since current filaments are inherently three-dimensional phenomena regardless of the chip topography, which can be stripe- or checkerboard-shaped, an alternative mapping of the real-chip IGBT cell topography to a quasi-3D simulation geometry is considered. In order to attain a computationally affordable approximation of 3D-filamentation effects that limit the SOA, the new approach extends the one described in chapter 5, by using large, monolithically integrated cell arrays as simulation domain in cylindrical cell geometry, resulting in cylindrical filaments. In this way a quasi-3D and, hence, more realistic approximation of the filamentary current flow is attained. Using this approach, the critical phenomena leading to a failure of the IGBT can then be analysed quantitatively.
Current inhomogeneities during over-current turn-off essentially limit the safe-operating area of high-voltage trench-IGBTs, because they may lead to device latch-up. Two-dimensional simulations of the turn-off process beyond the SOA based on 2D cross-sections of structures as simulation domain do not satisfactorily reproduce the data measured on three-dimensional chips. This is due to the fact that the 3D-nature of the filaments is not taken into account, leading to a considerable over-estimation of the threshold current density for latch-up limiting the safe-operating area. With a view to getting a better approximation of filamentary current flow in the real 3D chips, a cylindrical simulation geometry is introduced. This chapter is based on the work published in [41].

6.1 Simulation Approach

The simulation approach used here is the same as the one described in chapter 5 with the exception that the monolithically integrated structure (with 1% of the total active chip

area) exhibiting a filamentary current flow is modelled as a cylindrical structure. The external electrical circuit of the mixed-mode simulation with all its parameters such as, e. g. stray inductance, gate resistances and DC-link voltage, is left unchanged. It has to be emphasized that in this approach the structure exhibiting 99% of the total active area is left unchanged as well, i.e. that it is modelled as a single IGBT-cell in stripe geometry. This allows for a better comparison of the temporal behaviour of the turn-off process by itself, since the turn-off time of the parallel circuit of the two IGBTs is mainly governed by the large structure's turn-off time.
The generation of these cylindrical simulation structures and their mapping has already been described in detail in chapter 4. The use of such structures along with the results obtained for the 2D-Cartesian geometry allows for current filaments that are not bound to have a stripe-like shape but have a conical shape. This can lead to a quantitatively different behaviour of current filaments which, in turn, can lead to a different prediction of the limits of the safe-operating area with respect to over-current turn-off. Based on the results obtained from the previous chapter, it is expected that the limits predicted by these simulations reproduce measured data more accurately.

6.2 The Turn-Off Process: Isothermal Simulations

The turn-off time in cylindrical geometry is nearly the same as in stripe geometry as it is governed by the unchanged large structure. The main difference lies in the way the current density is distributed over the cylindrical simulation structure. Here, the possibilities for the current to redistribute and, hence, the shape a current filament can attain in this geometry, are fundamentally different, as a more pronounced focussing of current densities can take place.
For ease of comparison, the overall total active area of the simulation structures is held constant. Consequently, these structures differ from each other only by their number of individual cells as well as by their lateral extension. Both features were selected to on the one hand facilitate a more pronounced redistribution of the current densities and, on the other hand, provide a structure that is large enough to fully comprise a single current filament, regardless of the symmetry type of the simulation domain. In addition, homogeneous Neumann boundary conditions are applied along the edges of the structures, as was done in the case of stripe geometry. In cylindrical symmetry, the cells surrounding the innermost cell are used for generating a nearly homogeneous current density at the begin-

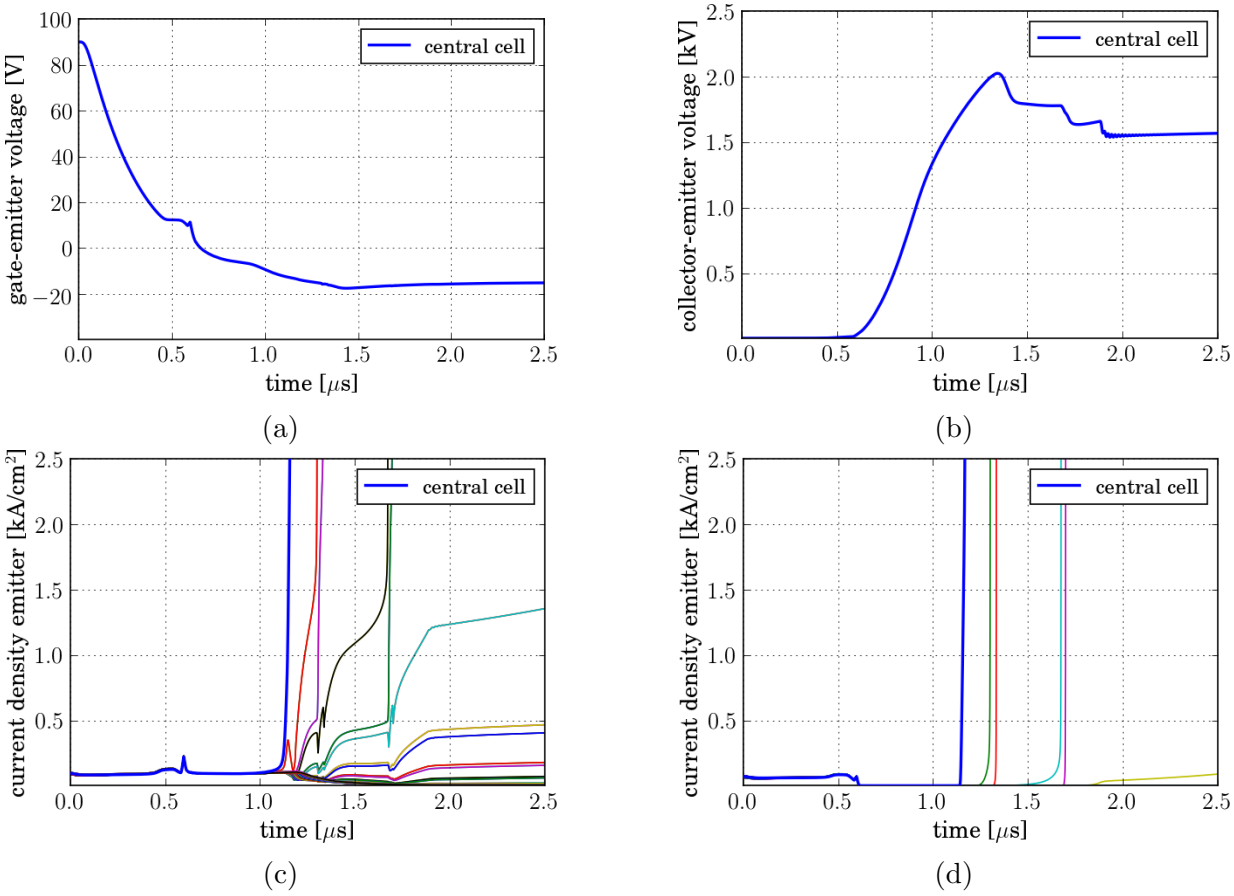

Figure 6.1: (a) gate-emitter voltage, (b) collector-emitter voltage, (c) electrical current densities at each emitter contact and (d) electron current densities at each emitter contact of a 32-cell integrated structure as a function of time. The innermost cell takes nearly the entire current shortly before device latch-up occurs. Note the homogeneous distribution of current densities at the emitter contacts until shortly before device latch-up.

ning of the turn-off process only. They play the role of hole extraction regions from the device after the closing of the MOS-channels (see Fig. 6.1a). In simulations in cylindrical symmetry considering multiple, physically connected IGBTs in a cell array, the innermost cell is assumed to be surrounded by neighbouring cells which, as approximation of the situation in the real chip, are represented by ring-shaped cells emulating the impact of the ambient on the central cell under investigation. This approach proves to be applicable to filamentary current flow during the turn-off process in real IGBT chips by determining that cell where a current filament gets 'trapped' due to slight asymmetries e.g. of the gate connection or of the actual temperature. This cell may be any arbitrary cell in the bulk of

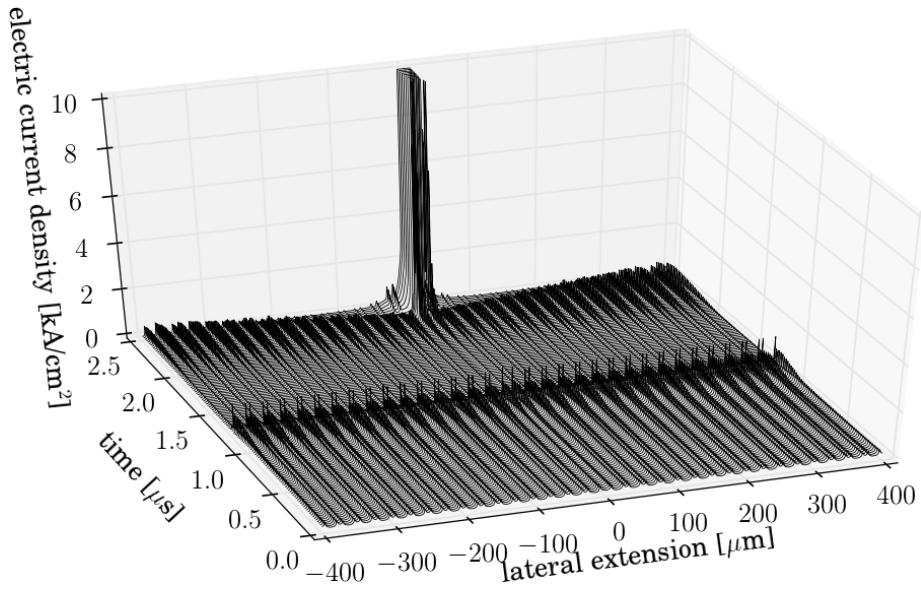

Figure 6.2: Current density along a lateral cut-line beneath the trenches as function of time for an isothermal simulation of a 32-cell integrated structure. Note that there is just one single current filament at each point in time, which does not move. The initial current density in this plot is 100A/cm^2 whereas the homogeneous lattice temperature throughout the entire simulation is 150°C. Note that the values for negative lateral extensions were obtained by mirroring the positive values, due to the simulation geometry used.

the chip. The center of the cell at which the current filament is eventually located defines the point where the axis of revolution of the cylindrical coordinate system is placed.
The basically two-dimensional shape of the filament is trapezoidal-like, in stripe and cylindrical geometry alike. The length of the short side is mainly determined by the distance between two adjacent trenches in stripe geometry and by the diameter of the circle described by the innermost trench-circle in cylindrical symmetry. These measures do not significantly differ from each other. At the lower side of the filament, i.e. at the border between space-charge region and electron-hole plasma, stripe-shaped filaments have an extension of about 100μm, whereas the central current filament has an extension of up to 400μm in cylindrical symmetry at the instant when latch-up sets on. Thus conical current filaments have, in conjunction with high vertical electric fields (which cause the carriers to move with saturation velocity), a large potential to extract holes from the electron-hole plasma. Due to a spatially inhomogeneous distribution of electrons and holes inside a filament, a strong and far ranging electric field in lateral direction exists, which focusses the flow of holes on their way to the emitter side and de-focusses the flow of electrons on

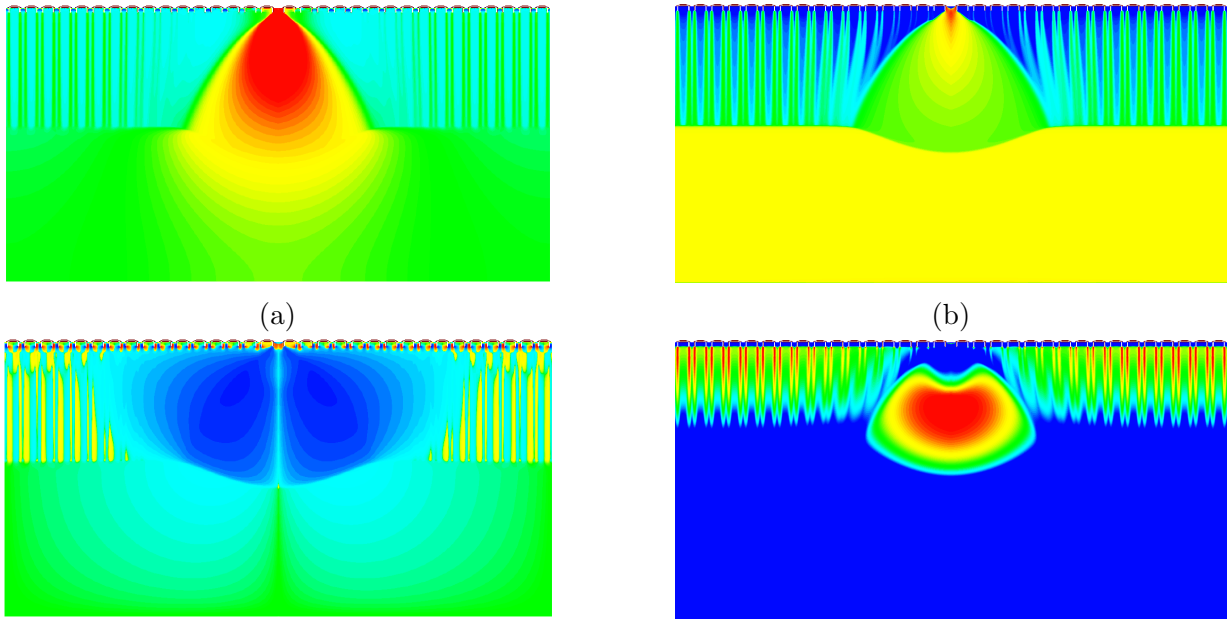

(a) (b) (c) (d)

Figure 6.3: (a) 2D plot of the electric current density 1.2μs after the begin of turn-off of a 32-cell cylindrical simulation structure. For clarity, the simulation structure is mirrored along the central vertical axis. Latch-up of the innermost cell is clearly visible (color scale: blue: 10A/cm^2, red: 5kA/cm^2). The initial current density amounts to 100A/cm^2.; (b) electron density; (c) 2D plot of the lateral component of the electric field at 1.2μs. Colour scheme: dark (light) blue: strong (weak) component pointing towards structure center, dark red (yellow): strong (weak) component pointing away from structure center, green: zero x-component. Note the wide range of the electric field in lateral direction which extends to nearly 250μm from the center. The color scheme in this plot was chosen to be logarithmic.; (d) impact ionization rate

their way to the collector side. As a result we obtain the trapezoidal shape of a filament in two dimensions. As can be seen in Fig. 6.3c, the lateral electric field inside the plasma region, just below the location of the filament, is non-zero, as is the vertical component. Due to the coordinate mapping used in the respective simulation approach, this may lead to fundamentally different current distributions at the emitter side and, consequently, to largely deviating predictions of the SOA limits of the device in case of stripe geometry.

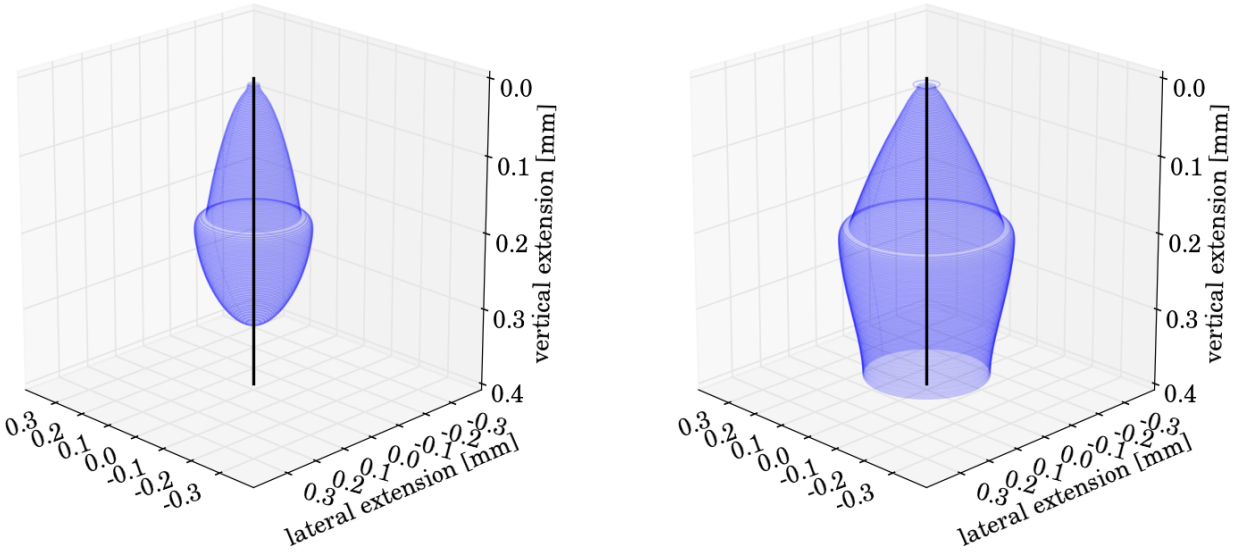

(a) $t = 1.20\mu$s

(b) $t = 1.25\mu$s

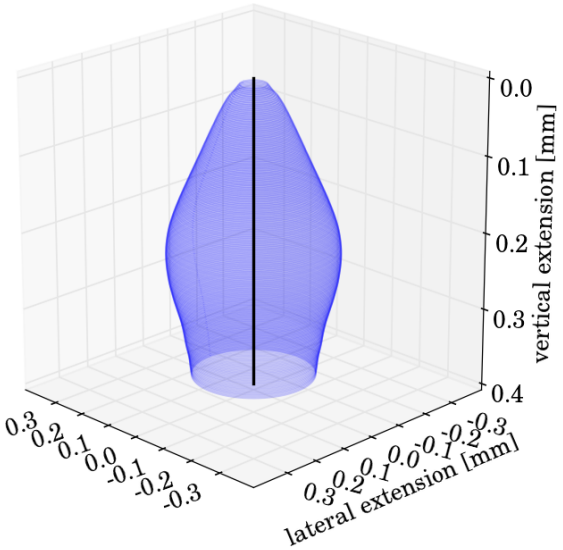

(c) $t = 1.40\mu$s

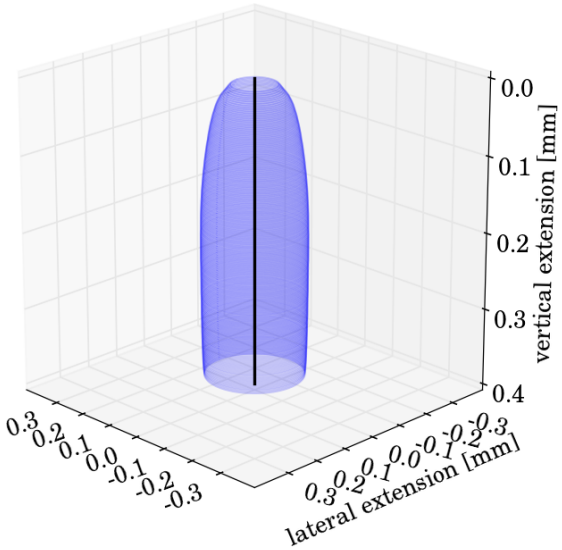

(d) $t = 2.50\mu$s

Figure 6.4: Shape of cylindrical current filaments around the axis of revolution (solid black line) obtained from isothermal simulations of a 32-cell cylindrical simulation structure at four different points in time during turn-off (cf. Fig. 6.3). The vertical extension of the simulation structure amounts to 400μm. The filament itself is defined as the region where the electric current density is above-average in this plot. See also Fig. 6.2.

6.3 Processes Leading to Device Latch-Up

The formation of a central current filament (Figs. 6.2) may subsequently lead to device failure, if a sufficiently large current density at the emitter side (Fig. 6.1c) is attained due to electron injection from the emitter side (Fig. 6.1d) and the formation of a plasma channel, (i.e. the turn-on of the parasitic thyristor). The threshold current density for emitter-side injection of electrons is roughly 20% larger in cylindrical geometry (1.2kA/cm^2 compared to 1.0kA/cm^2). This results from the geometry of the source-body *pn*-junction depending on the simulation symmetry. The excessive amount of holes that moves beneath the source during over-current turn-off causes a voltage drop at this *pn*-junction. In the case of stripe symmetry the *pn*-junction exhibits a rectangular shape and the condition for forward biasing is reached for a certain hole current density at the emitter contact. In cylindrical symmetry on the other hand, the *pn*-junction is ring-shaped, and the same hole current density causes a lower voltage drop since the focusing of holes is less pronounced. Consequently, a higher hole current density is needed in order to forward-bias the junction. This hole current density is substantially determined by the extension of the filament along the border between the space-charge region and the electron-hole plasma (Figs. 6.3a). This is due to its capability to extract holes from the plasma and focus them on their way to the emitter side. The lateral range of hole collection of the central current filament amounts to approximately 10 simulation cells, which corresponds to approximately 400μm, as it is visible from the shape of the time-dependent contact current densities: in the course of developing a high current density, the innermost cell collects holes from all adjacent concentrical cells up to where the lateral component of the electrical field (cf. Fig. 6.3c) is no longer strong enough to move the holes towards the center. This leads to a drop in the local current densities of the un-latched cells at the respective emitter contacts which is noticeable up to cell number 10 from the axis of revolution (note the drop in current densities at the emitter contacts in Fig. 6.1c between 1.10μs and 1.20μs). In addition, each time a non-central cell runs into latch-up the next-neighbour cell shows a drop in the local current density as well, which derives from the same mechanism as described above. Thus, in cylindrical symmetry, device failure due to latch-up occurs at considerably lower initial current densities, i.e. much closer to the measured data.

In order to fully take these physical effects into account, large simulation structures, i.e. structures with a large lateral extension, are needed. In turn, if the lateral extension is too small, i.e. if the structure used for the analysis is too small, these physical effects

are not reproduced satisfactorily and quantitatively sensible predictions of the SOA are not possible. The innermost cell always latches first, with the consequence that the IGBT structure would be destroyed if heating was taken into account. Destruction may then spread to the adjacent cells as well.
The time span between the beginning of turn-off and the formation of a plasma channel strongly depends on how close the initial current density before turn-off lies above the latch-up current density: the more the critical current density is exceeded, the faster latch-up occurs. In any case, latch-up does not occur before the gate-emitter voltages have fallen below the threshold voltage of the MOS-channels.

6.4 The Turn-Off Process: Electro-Thermally Coupled Simulations

In order to investigate temperature effects on the qualitative behaviour of current densities during the turn-off process, as well as on the quantitative behaviour regarding the limits of the SOA, electro-thermal coupling is taken into account. The set-up for simulations is, apart from the self consistent calculations, identical to the isothermal one described in the previous section.
Looking at the results presented for electro-thermally coupled simulations in stripe geometry it is reasonable to assume that thermal effects due to local heating and the presence of temperature gradients have an impact on the temporal behaviour of the current filaments. Despite the fact that thermal effects play an important role, it is worth emphasizing that the time-scales for thermal processes are much longer than those for electrical processes. Universally speaking, increased lattice temperatures cause an increased effective intrinsic density, i.e. more free carriers are present inside of the device which in turn favours latch-up. As can be seen in Figs. 6.5, current filaments clearly exhibit movement according to a gradient in temperature, which in turn causes a more homogeneous heating at the front side of the device as would be the case without filament movement. Yet, just as in the case of isothermal simulations in cylindrical geometry, physically meaningful simulation results of device destruction exist only if the central cell latches first. This is the case in each simulation that is presented in this work as the gate-resistance of the innermost cell was chosen to be slightly different from those of the other cells. The main goal of this approach is to determine the quantitative differences with regard to the safe-operating area as a function of the geometry of a current filament. To this end, the initial current density

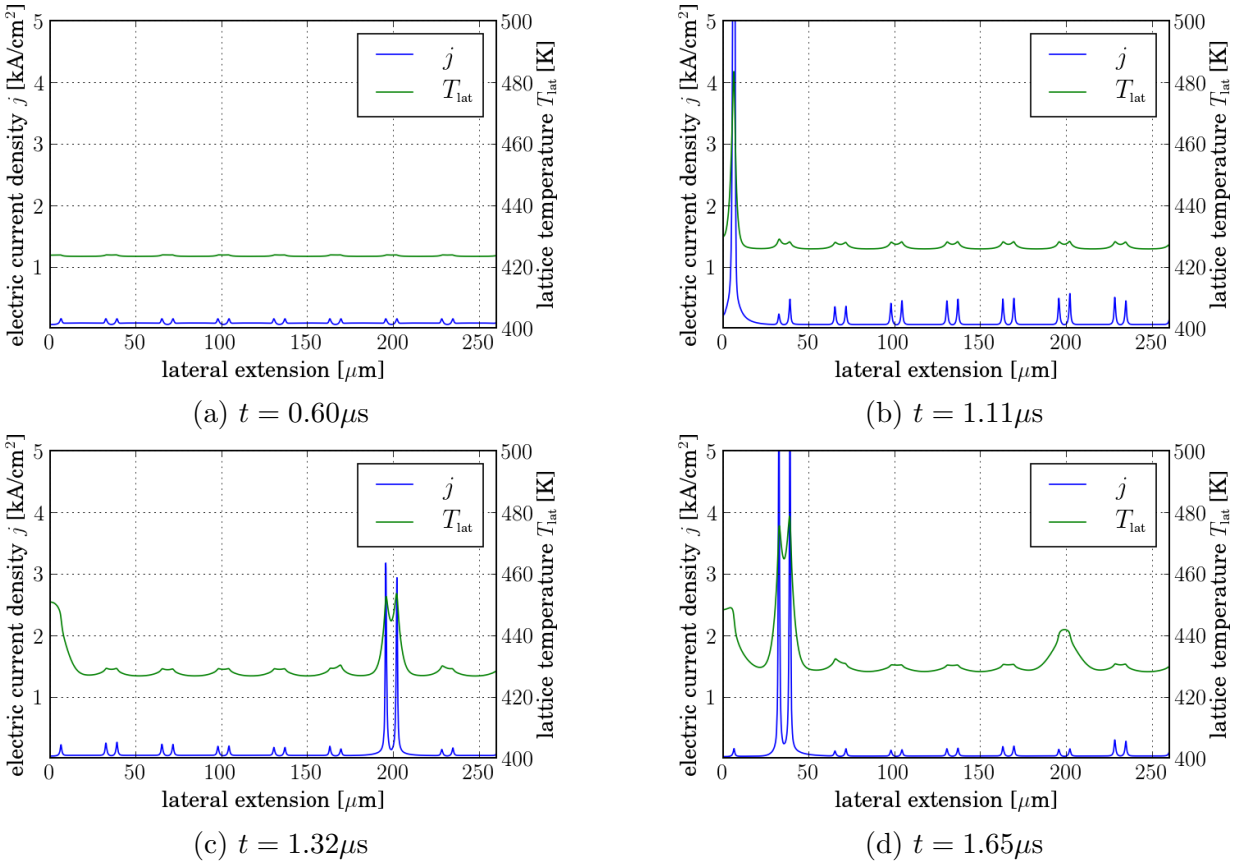

(a) $t = 0.60\mu$s

(b) $t = 1.11\mu$s

(c) $t = 1.32\mu$s

(d) $t = 1.65\mu$s

Figure 6.5: Gradient in temperature as driving force for movement of current filaments in cylindrical structures. Electro-thermally coupled simulations of a 16 cell monolithically integrated structure in cylindrical symmetry for four different points in time. The initial current density in this case amounts to 82A/cm^2. The IGBT turns off, thus no device latch-up occurs.

$j_{\mathrm{init}} = j(t = t_0)$, is increased stepwise until the device runs into latch-up. The threshold then being somewhere in the interval between the highest current density at which no latch-up occurs and the lowest current density at which latch-up occurs.

In order to verify measurement results, the mapping procedure stated in chapter 4 was applied to the IGBT-chip which was the device under test in the experiments. It is worth mentioning that the initial current density as well as the initially homogeneous lattice temperature can be controlled and measured in experiments and can be chosen accordingly in simulations. This significantly facilitates the comparison between theory and experiment. For the specific device under test, measurements delivered a latch-up threshold current density j_{lup} of 100A/cm^2 $< j_{\mathrm{lup}} <$ 110A/cm^2. Simulation results for j_{lup} give

$108\text{A/cm}^2 < j_{\text{lup}} < 117\text{A/cm}^2$ as can be seen in Figs. 6.6, thus giving a relative error of at most 17%. This is clearly closer to measured data than simulations using 2D-Cartesian coordinates and is likely to be within the deviations among a set of IGBT-chips. Since the exact movement of current filaments in electro-thermally coupled calculations depends on the exact local lattice temperatures, slight variations of the initial current densities before turn-off can lead to variations in current filament movement as local heating solely depends on the position of current filaments and the local heating they generate due to Joule heat (cf. chapter 2). Furthermore the self-limiting nature of impact ionization due to its negative temperature coefficient sets in earlier for higher current densities, thus changing the dynamics of the filaments. This can have a minor effect on the exact threshold for latch-up compared with the effect geometry has on this threshold as the position of a filament can influence the amount of electrons injected from the emitter side as a precursor to latch-up. This effect can be seen in Figs. 6.6 as well. To account for this effect, the latch-up threshold was determined in a way that at the approximate position of the threshold, several turn-off simulations with slightly varying initial current densities were conducted in order to get a more precise view of the impact this effect has on the limits of the safe-operating area. It is worth mentioning that this effect does occur for larger simulation structures only, since there only, current inhomogeneities can redistribute themselves in different ways. The simulation results obtained in these investigations are shown in Figs. 6.8.

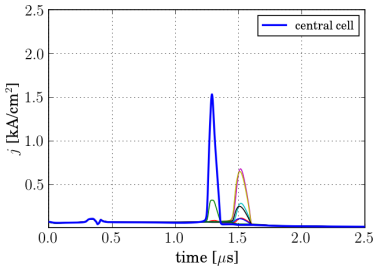

(a) $j_{\mathrm{E}}^{(i)}(t)$, $j_{\mathrm{init}} = 63\mathrm{A/cm}^2$

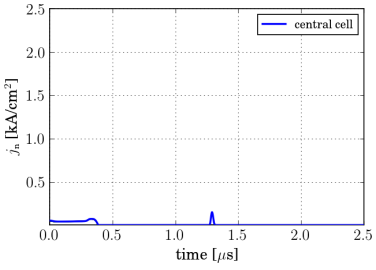

(b) $j_{\mathrm{E,n}}^{(i)}(t)$, $j_{\mathrm{init}} = 63\mathrm{A/cm}^2$

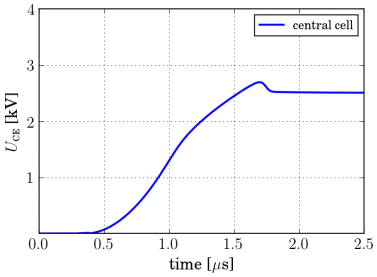

(c) $U_{\mathrm{CE}}(t)$, $j_{\mathrm{init}} = 63\mathrm{A/cm}^2$

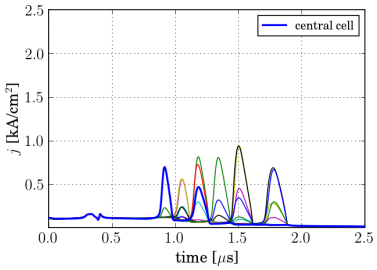

(d) $j_{\mathrm{E}}^{(i)}(t)$, $j_{\mathrm{init}} = 108\mathrm{A/cm}^2$

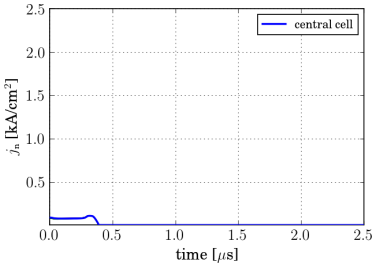

(e) $j_{\mathrm{E,n}}^{(i)}(t)$, $j_{\mathrm{init}} = 108\mathrm{A/cm}^2$

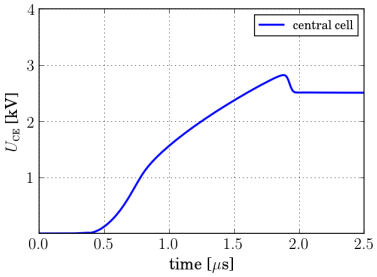

(f) $U_{\mathrm{CE}}(t)$, $j_{\mathrm{init}} = 108\mathrm{A/cm}^2$

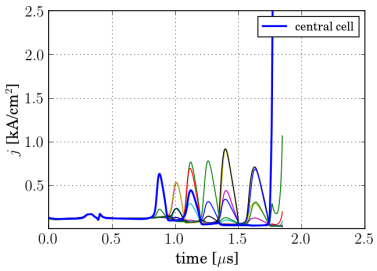

(g) $j_{\mathrm{E}}^{(i)}(t)$, $j_{\mathrm{init}} = 117\mathrm{A/cm}^2$

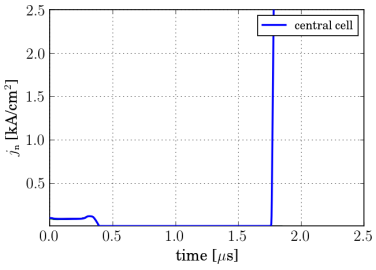

(h) $j_{\mathrm{E,n}}^{(i)}(t)$, $j_{\mathrm{init}} = 117\mathrm{A/cm}^2$

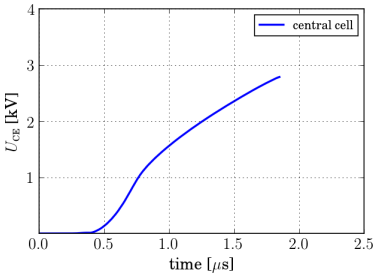

(i) $U_{\mathrm{CE}}(t)$, $j_{\mathrm{init}} = 117\mathrm{A/cm}^2$

Figure 6.6: Turn-off process of 16-cell IGBT structure in cylindrical geometry and for electro-thermally coupled simulations. The initially homogeneous current density before turn-off, j_{init}, is increased in the simulation in order to determine the threshold for device latch-up. Note the considerably different filamentation (a, d, g) and emitter-side electron injection (b, e, h) behaviour. The threshold for latch-up is between $j_{\mathrm{init}} = 108\mathrm{A/cm}^2$ and $j_{\mathrm{init}} = 117\mathrm{A/cm}^2$.

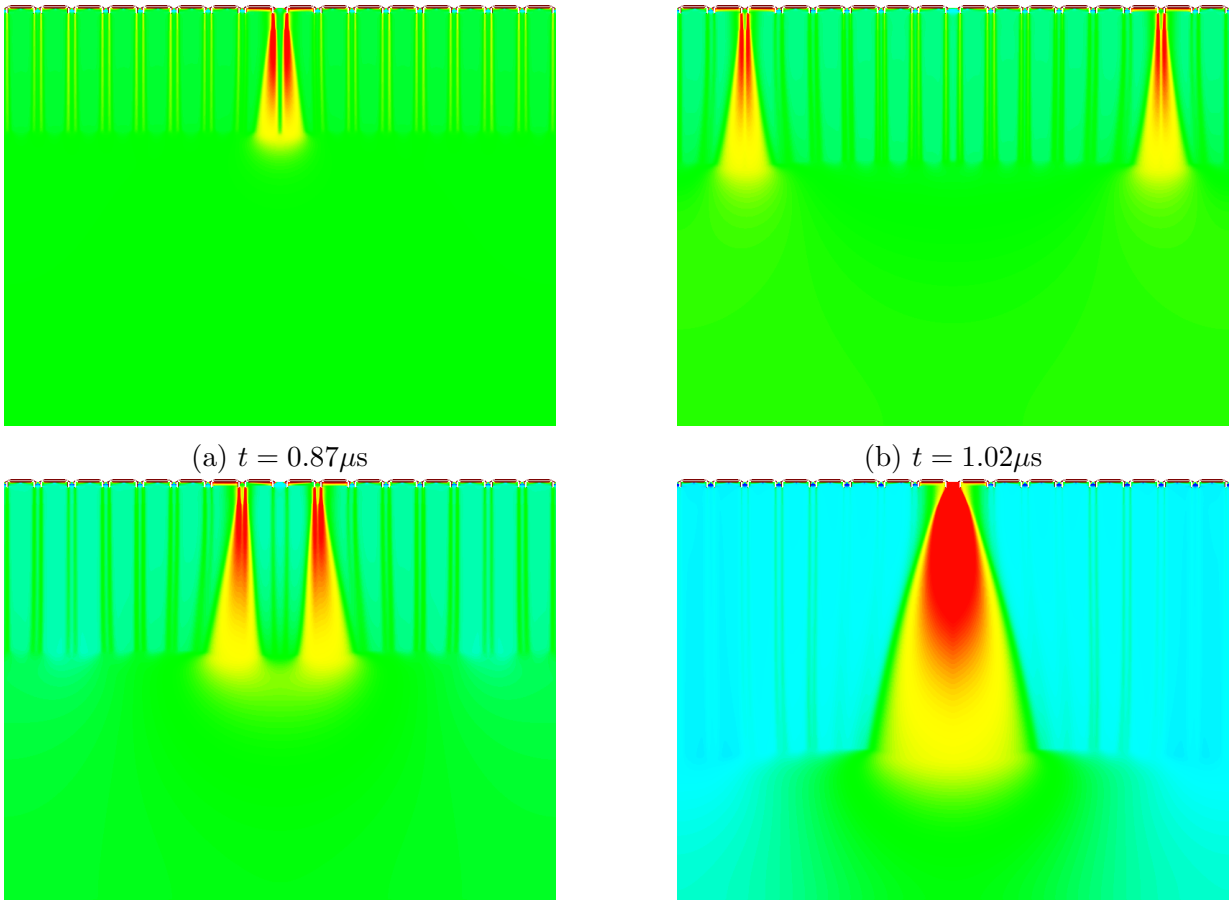

(a) $t = 0.87\mu$s (b) $t = 1.02\mu$s

(c) $t = 1.11\mu$s (d) $t = 1.80\mu$s

Figure 6.7: Contour plot of the electrical current density during turn-off of a 16-cell structure in cylindrical geometry for electro-thermally coupled simulations at four different points in time. The initial current density in this case amounts to $j_{\text{init}} = 117\text{A/cm}^2$. The current densities and respective collector-emitter voltage of this turn-off process are depicted in Figs. 6.6g,6.6h and 6.6i.

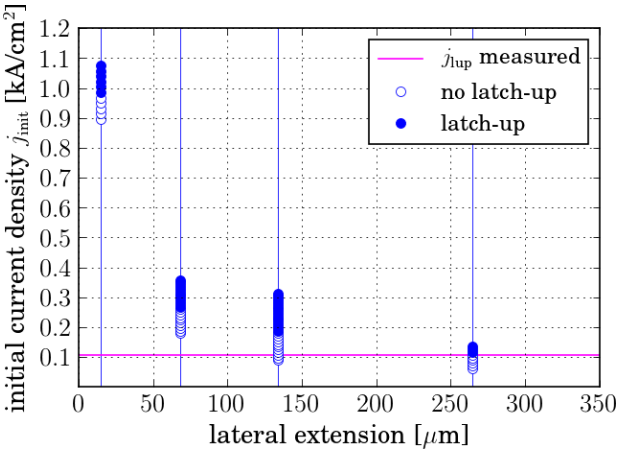

Figure 6.8: Several turn-off simulations of structures ($l_{\mathrm{tr}} = 5.4\mu$m) with different vertical extensions (different number of cells in a monolithically integrated structure, here: 1, 4, 8 and 16 cells). Latch-up is depicted by solid blue dot, whereas no latch-up is depicted by blue circle. The latch-up current densities therefore are located between dots and circles. In this case, the latch-up current densities are unambiguous as can be seen in the plot.

6.5 Variation of Cell Geometry

For a further quantitative analysis of the threshold for device latch-up with regard to an increased robustness of the IGBT, the simulation approach using cylindrical geometry is extended to a geometrical cell geometry variation. More precisely, the relative distance Δl between the pn-junction of the floating p-region, the n^--base and the trench-bottom is increased. This is done in a way that leaves the floating p-region unchanged, i.e. the region is located like for a cell with a trench depth of $l_{\mathrm{tr}} = 5.4\mu\mathrm{m}$, and the trench depth itself is increased by $1\mu\mathrm{m}$. All other measures defining the IGBT such as the overall geometry, doping profiles and active area, are left unchanged. This analysis is motivated by the

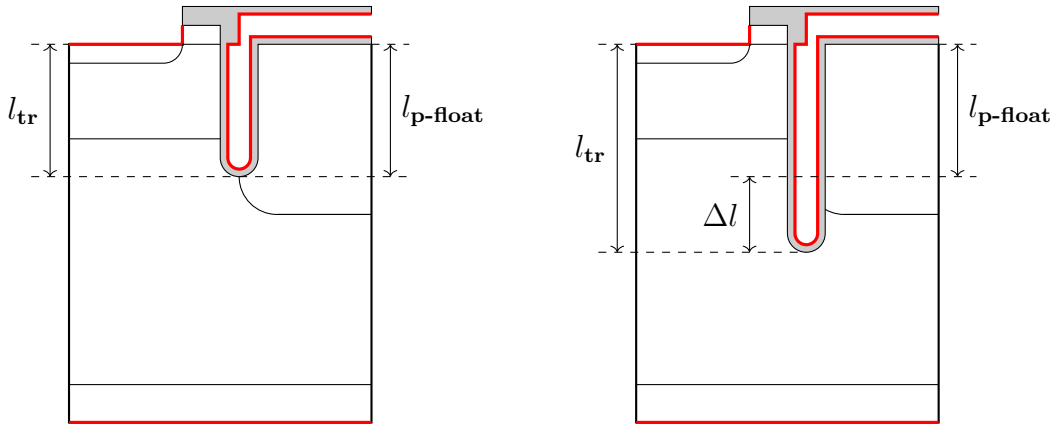

Figure 6.9: Schematic view of (a) Shallow Trench. (b) Deep Trench. $\Delta l \equiv l_{\mathrm{tr}} - l_{\mathrm{p\text{-}float}}$, p-float doping is left unchanged by the trench depth variation. The relative distance between trench-bottom and the p-float doping is increased from $\Delta l = 0\mu\mathrm{m}$ to $\Delta l = +1\mu\mathrm{m}$.

experimental evidence that the limits of the safe-operating area are shifted towards higher current densities for larger Δl. Quantitative simulations of this geometry change reveal an increased latch-up threshold, thus suggesting an improved ruggedness of the device with respect to over-current turn-off situations. It was found that the filamentation behaviour of the device significantly changes for cells with $l_{\mathrm{tr}} = 6.4\mu\mathrm{m}$, i.e. for $\Delta l = +1\mu\mathrm{m}$. One obvious difference being that the development of current inhomogeneities takes place later in the turn-off process, the process thus remains homogeneous for a longer period of time. A physical explanation for this behaviour can be found the fact that an increased Δl leads to higher field-peaks at the bottom of the trenches which causes the onset of impact ionization at lower collector-emitter voltages (impact ionization being dependent on the electric field strength and the local lattice temperature only, cf. chapter 2). Additionally, the impact

ionization is located more sharply beneath each trench bottom alike, giving the turn-off process a higher degree of homogeneity for a certain amount of time until the symmetry is broken. After this, the gradients in temperature force the current filaments to move. (A more detailed explanation of this physical effect is given in the following chapter using a different simulation approach which facilitates the comparison of different geometries.)
It was found in simulations that the limits of the safe-operating area exhibit a high sensitivity on this distance. This means that only a minor change of Δl, which could well be within the tolerances of the fabrication process, can significantly increase or lower the latch-up threshold. The latch-up current density as a function of Δl alongside a comparison with measurement is depicted in Fig. 6.11. As can be seen, the difference between simulation and measurement is larger as in the case that was previously discussed.
For completeness, simulations intended as reference simulations where l_{tr} is increased and the depth of the floating p-region is increased by the same amount, thus leaving Δl unchanged, showed no differences in the latch-up threshold. Hence the relative distance Δl between these two is the relevant measure and the trench-depth itself is not the cause for an increased robustness.

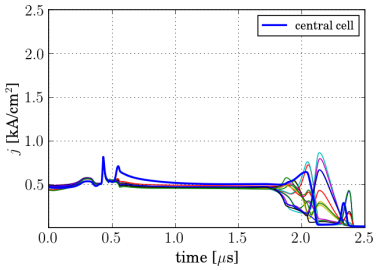

(a) $j_{\mathrm{E}}^{(i)}(t)$, $j_{\mathrm{init}} = 450\mathrm{A/cm}^2$

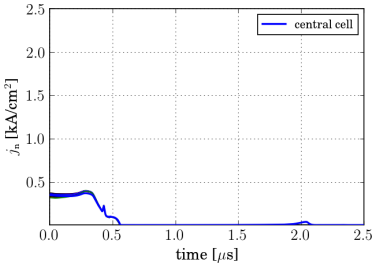

(b) $j_{\mathrm{E,n}}^{(i)}(t)$, $j_{\mathrm{init}} = 450\mathrm{A/cm}^2$

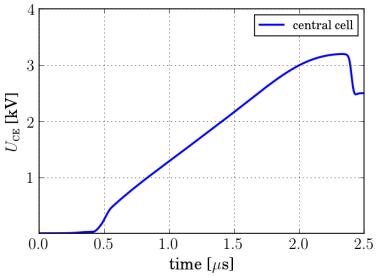

(c) $U_{\mathrm{CE}}(t)$, $j_{\mathrm{init}} = 450\mathrm{A/cm}^2$

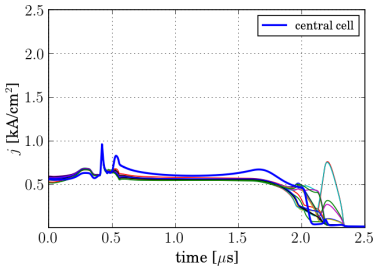

(d) $j_{\mathrm{E}}^{(i)}(t)$, $j_{\mathrm{init}} = 540\mathrm{A/cm}^2$

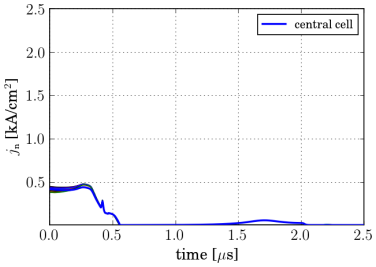

(e) $j_{\mathrm{E,n}}^{(i)}(t)$, $j_{\mathrm{init}} = 540\mathrm{A/cm}^2$

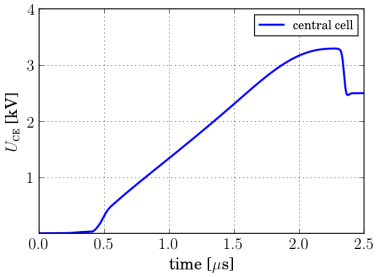

(f) $U_{\mathrm{CE}}(t)$, $j_{\mathrm{init}} = 540\mathrm{A/cm}^2$

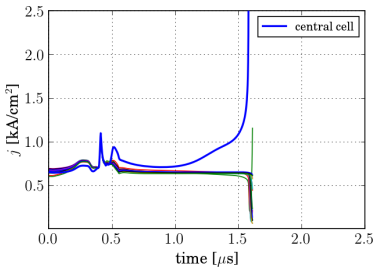

(g) $j_{\mathrm{E}}^{(i)}(t)$, $j_{\mathrm{init}} = 630\mathrm{A/cm}^2$

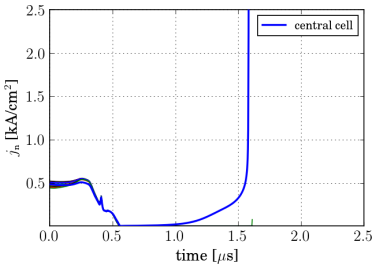

(h) $j_{\mathrm{E,n}}^{(i)}(t)$, $j_{\mathrm{init}} = 630\mathrm{A/cm}^2$

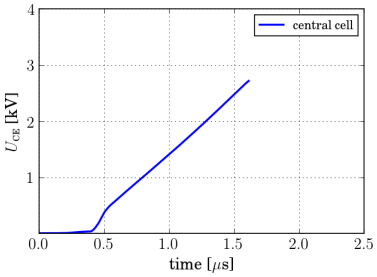

(i) $U_{\mathrm{CE}}(t)$, $j_{\mathrm{init}} = 630\mathrm{A/cm}^2$

Figure 6.10: Turn-off process of 16-cell IGBT structure in cylindrical geometry and for electro-thermally coupled simulations with increased trench-depth of 6.4μm. The initially homogeneous current density before turn-off, j_{init} is increased in order to determine the threshold for device latch-up. Note the considerably prolonged homogeneous turn-off (a, d, g). The emitter-side electron injection (b, e, h) is not especially pronounced. The threshold for latch-up is between $j_{\mathrm{init}} = 540\mathrm{A/cm}^2$ and $j_{\mathrm{init}} = 630\mathrm{A/cm}^2$ and thus considerably higher than for the structure with a trench-depth of 5.4μm.

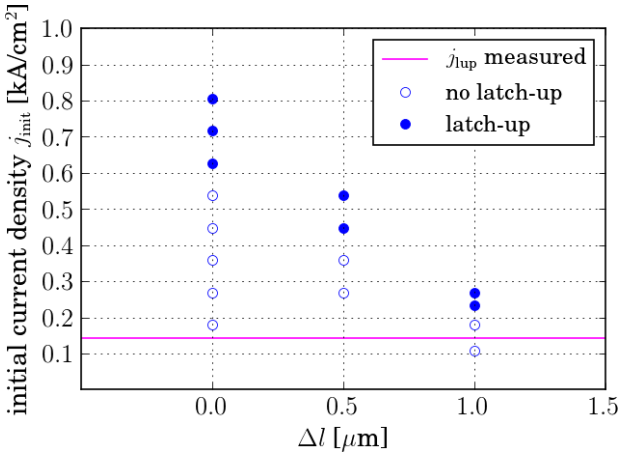

Figure 6.11: Several turn-off simulations of a 16-cell cylindrical simulation structure with a trench-depth of 6.4μm as a function of the relative distance Δl between the p-float region and the trench bottom. A decrease in the latch-up current density with increasing Δl is clearly visible.

7. Static Characteristics

So far, the temporal behaviour of physical processes during device turn-off was investigated using transient turn-off simulations. It is however possible to gain further insight into current filaments, their physical properties and their safe-operating area by looking at the static characteristics of IGBTs. This is possible because the transient behaviour can be approximated by a series of static characteristics of several auxiliary simulation structures which differ only in their vertical extensions. This approach has the additional advantage of being more time efficient than the transient turn-off simulations described earlier.
The simulation method which is described in this chapter aims at reproducing the device behaviour during turn-off which is relevant for the formation of current filaments and the subsequent latching of the device, i.e. determining the rim of the safe-operating area. To this end, a situation where the MOS-channels are already closed and physical processes like the onset of impact ionization, device snap-back as well as the emitter-side injection of electrons is considered. What is more, these critical phenomena can be investigated as a function of the vertical extension of current filaments, independent of their geometrical shape, giving more insight into the qualitative as well as quantitative differences in the physical effects arising from different filament geometries.
As is known from literature, current filaments are non-linear phenomena which occur if a device is in a non-stable state, i.e. a state in which the static characteristics exhibit a negative slope, which in turn corresponds to a negative differential resistivity. In all cases presented in this thesis, the current instabilities are 'S'-shaped, which is commonly referred to as 'current-controlled' instabilities. Additionally, regions in the static characteristic exhibiting a positive slope indicate stable states of the device.
This chapter is structured as follows: An overview of the simulation approach this chapter is based on is given, preceded by a detailed physical interpretation of the current constituents resulting in the static characteristics. Special emphasis is put on the obvious differences in the characteristics which arise due to a variation of the trench depth, i.e. a variation of the relative distance between the trench bottom and the floating p-region, as was already

discussed in the previous chapter. Furthermore, a comparison of the characteristics of structures with cylindrical geometry as well as those of 2D-Cartesian geometry is given. This simulation approach is partially based on the one given in [42] and [43].

7.1 Simulation Approach

The physical processes occurring during device turn-off can, to a certain extent, be replaced by a series of static IV-characteristics with a modified structure: the start of the static characteristics is when the MOS-channels are already closed and the space-charge region has already developed and exhibits a vertical extension of about 100μm. At this point, electric fields can develop which are locally high enough to cause impact ionization and electron injection from the emitter side which are prerequisites for the latching of the IGBT.
In the case presented here these static characteristics have, a typical 'S'-shaped characteristic which can have a branch of negative differential resistivity. In this voltage range, the device is in an unstable state. In order to reach a stable state different regions will form inside the device which are characterized by high and low current densities. Inside this voltage range the IGBT forms current filaments.
In order to reproduce the extraction of the electron-hole plasma region during device turn-off, this region is replaced by a p^+-emitter. The extraction of the plasma is modelled with different distances between the front side of the device and the emitter p-doping. The vertical depth of the emitter p-doping itself is $l_{\mathrm{em}} = 10\mu$m, after that the structure is cut-off. This approach opens the possibility to compare physical quantities of current filaments at identical vertical extensions of the current filaments in different simulation geometries. Additionally, a further approximation of the real structure can be made by leaving out cells that do not play a significant role during the turn-off or in the case of static characteristics by simply replacing them with a p-body doping that is laterally constant. As opposed to the transient simulations described in previous chapters now no initially homogeneous current density has to be created using this approach. The emitter contact spans the entire lateral extension and hence allows the holes to leave the device at the front side. (The collector contact is left unchanged, covering the entire lateral range of the back-side.) A schematic depiction of such an auxiliary simulation structure is given in Fig. 7.1. An advantage of this approach is that it can be applied to both 2D-Cartesian and cylindrical geometries, enabling a direct comparison of the two geometries. The dimensioning of the

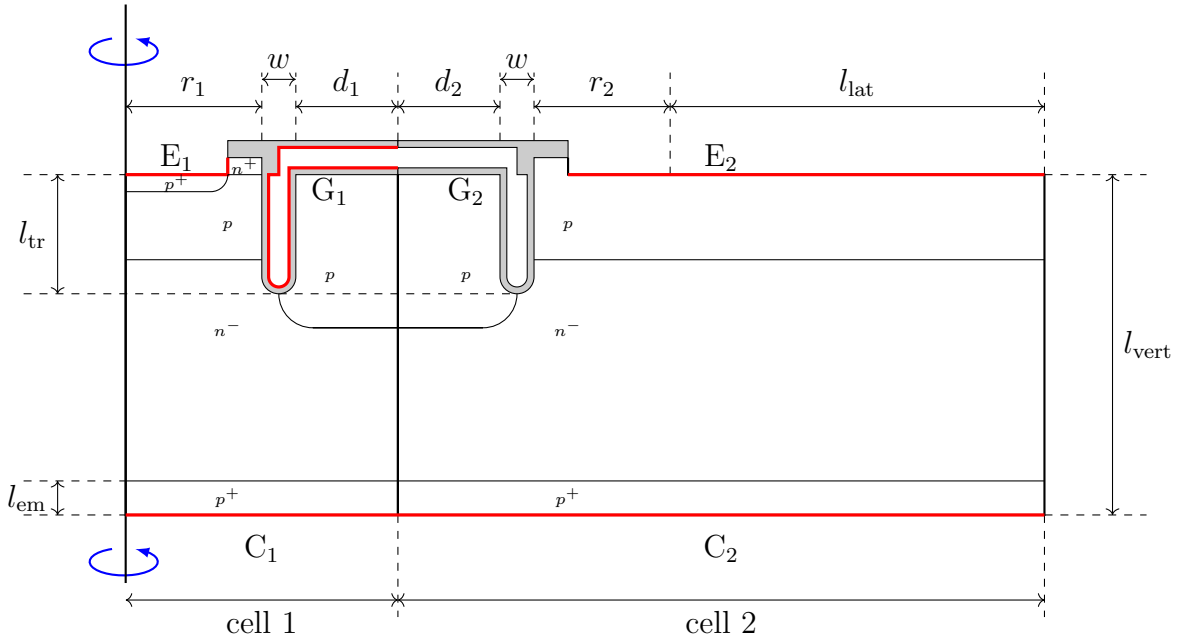

Figure 7.1: l_{lat} additional lateral extension of the simulation structure in order to create space for the current filament, l_{vert} vertical extension of the simulation structure which is increased stepwise in order to investigate the physical features of a current filament as a function of its length. It is important to note, that an increase of the simulation structure in vertical direction effectively means an increase in vertical direction of the base layer. All other doping profiles remain unchanged. l_{tr} depth of the trench. The axis of revolution is located at the left edge of the simulation structure. Note that the gate contact as well as the n^+-source and the p^+-doping have been removed, respectively, from the second cell.

cell measures follows the approach given in chapter 4. A study of current filamentation and latch-up as a function of the lateral extension of the simulation structure, as was mentioned above, can now be made, enabling a more detailed numerical analysis of these physical phenomena. (The variation of the lateral extension of the simulation structure can also be used to measure how well a single current filament fits inside a simulation structure. This particular topic was discussed at length in the previous chapter it will not be mentioned again here.) From a practical point of view, the simulation of static characteristics is considerably faster and therefore gives results much faster.

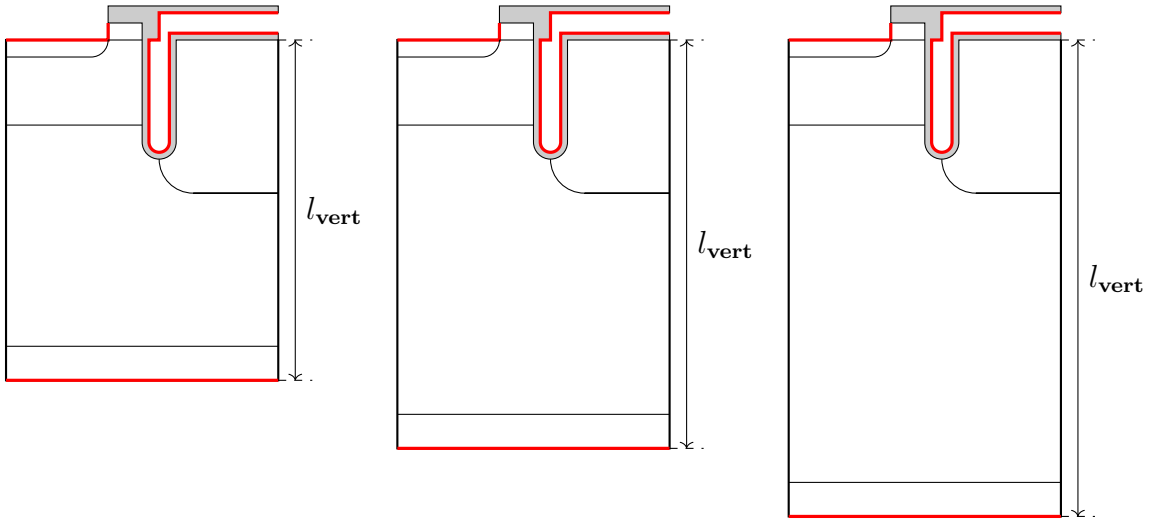

Figure 7.2: Examples for simulation structures (central cell only) with different vertical extensions used for investigating the static characteristics. Note that the base layer only is enlarged in vertical direction whereas the basic geometry and doping, respectively, are left unchanged, especially l_{em} is left unchanged. The resulting vertical extension of a filament l_{f} consequently is given by $l_{\mathrm{f}} = l_{\mathrm{vert}} - l_{\mathrm{tr}} - l_{\mathrm{em}}$ which for simulation structures with large vertical extensions can be approximated by $l_{\mathrm{f}} = l_{\mathrm{vert}}$.

7.2 Simulation of Static Characteristics in Cylindrical Geometry

The approach using static characteristics was applied to all structural variations in order to determine its influence on the safe-operating area of the IGBT. As can be seen in Fig. 7.3, the trench depth has a significant influence on the IV-curve as well as the robustness of the device. This is due to a considerably different shape of the electric field inside the device, which is strongly dependent on the shape of the trench and the relative position of the trench bottom to the p-float doping beneath the oxide layer. A closer inspection of the IV-characteristics shows different distributions of regions with negative differential resistivity for cells with different trench depths as well as a strong difference in the snap-back voltages U_{SB} for the same vertical extension of the simulation structure. On the contrary, the threshold in hole current density at the emitter contact has a very weak dependency on the trench depth and the vertical extension of the simulation structure. The relative difference in the threshold current density lie in the range of a few percent at most. (The threshold current density for electron injection in this work is defined as

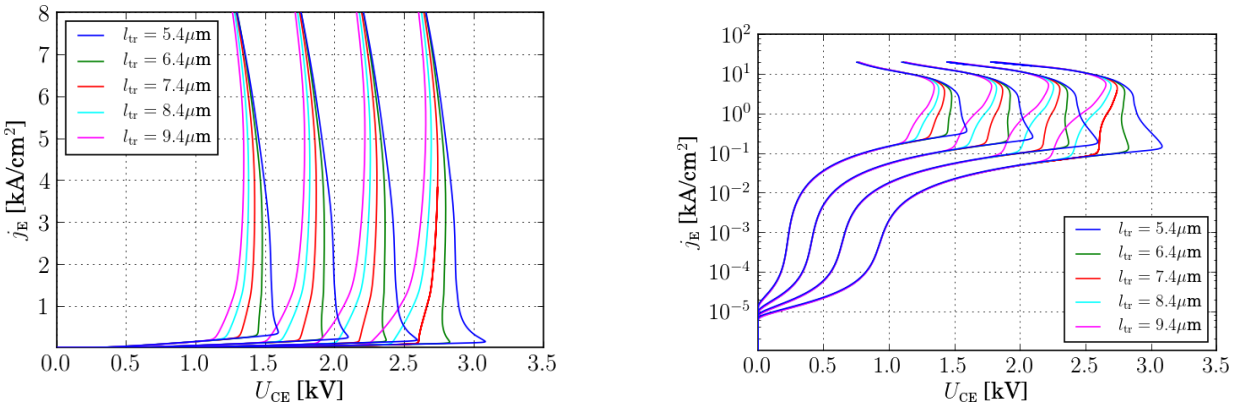

(a) (b)

Figure 7.3: (a) Linear representation. (b) Logarithmic representation of IV-curve for trench depth (l_{tr}) variation for 5.4μm, 6.4μm, 7.4μm, 8.4μm and 9.4μm for four different (150μm, 200μm, 250μm and 300μm) vertical extensions of the simulation structure. Note that the different values for l_{tr} correspond to Δl values of 0μm, 1μm, 2μm, 3μm and 4μm as introduced in the previous chapter.

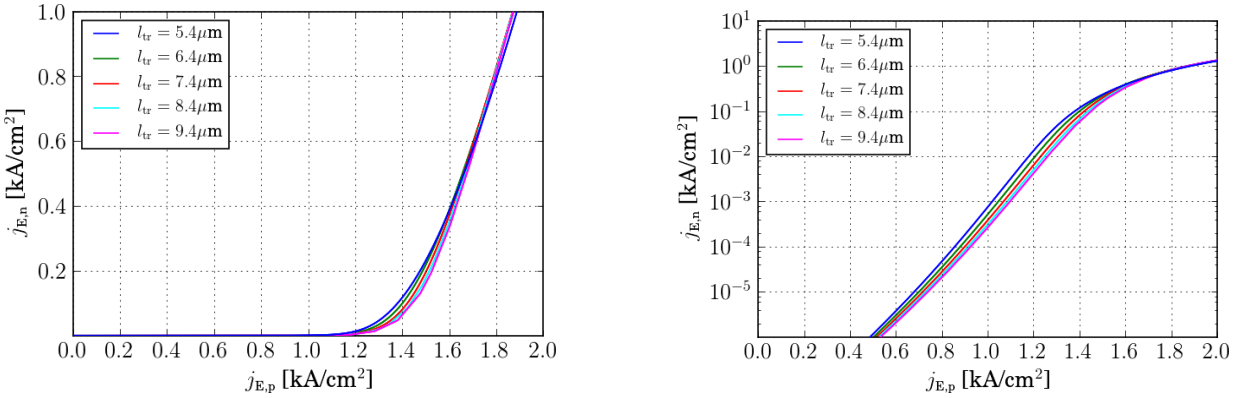

(a) (b)

Figure 7.4: (a) Linear representation and (b) logarithmic representation of electron current density at the central emitter contact as a function of the hole current density at the same emitter contact for 5.4μm, 6.4μm, 7.4μm, 8.4μm and 9.4μm for 150μm vertical extensions of the simulation structure. Note that the different values for l_{tr} correspond to Δl values of 0μm, 1μm, 2μm, 3μm and 4μm as introduced in the previous chapter.

the value of the hole current density at the emitter contact at which the electron current density at the same emitter contact becomes significantly different from zero.) A linear as well as a logarithmic plot for the electron current density as a function of the hole current density at the central emitter of the cylindrical auxiliary simulation structure for all five

different trench depths is depicted in Fig. 7.4.
A physical interpretation of the impact of these changes to the static characteristics of the IGBT will be discussed in the following section with a focus on exploring probable changes to the limits of the SOA. First, the differences in the electrical field distribution, lateral and vertical component, respectively, will be investigated as they govern the carrier dynamics, especially the impact ionization at the trench bottoms. Second, the regions inside the static characteristics that exhibit a negative differential resistivity are analysed, especially what causes the IV-curve to be negative. Furthermore, the point at which the snap-back occurs as well as the electron injection from the emitter side and to what amount the total current density at the emitter side consists of electrons will be investigated. These dependencies are analysed with respect to the variations in the cell geometry, aiming at a better understanding of the dependency of current filamentation and latch-up on the cell geometry and thus a possibility to optimize the chip against this failure mechanism.
From a simulation point of view the characteristics are obtained by a voltage ramp up to the snap-back voltage followed by a current ramp, which is often referred to as boundary condition switching. Furthermore, in all simulations of static characteristics the lattice temperature is held constant at 423K.

7.3 Physical Interpretation of Static Characteristics

In order to obtain more insight into the physical processes behind the characteristics, constituents of the current at the emitter contact are investigated as a first step. The basic constituents are the electron (hole) current at the collector contact $I_{\mathrm{C,n}}$ ($I_{\mathrm{C,p}}$), as well as the electron (hole) current at the emitter contact$I_{\mathrm{E,n}}$ ($I_{\mathrm{E,p}}$) which add up to the total currents I_{C} and I_{E} at the electrical contacts. From these components an effective generation recombination hole current $I_{\mathrm{GR,p}}$ can be deduced by

$$I_{\mathrm{GR,p}} = I_{\mathrm{E,p}} - I_{\mathrm{C,p}} \tag{7.1}$$

giving the number of holes generated by impact ionization inside of the device, which is equal to the number of electrons generated by impact ionization inside of the device. Looking at these constituents, three different current constituents can be distinguished,

which are

$$I_{\mathrm{E}} = \begin{cases} I_{\mathrm{C,p}} & \text{for } 0 \leq I \leq I_{\mathrm{ii}} \\ I_{\mathrm{C,p}} + I_{\mathrm{GR,p}} & \text{for } I_{\mathrm{ii}} < I \leq I_{\mathrm{e-inj}} \\ I_{\mathrm{C,p}} + I_{\mathrm{GR,p}} + I_{\mathrm{E,n}} & \text{for } I > I_{\mathrm{e-inj}} \end{cases} \tag{7.2}$$

depending on the total contact current. An illustration of these components is given in Fig. 7.5. Note that $I_{\mathrm{GR,p}}$ can attain negative values if recombination processes outnumber

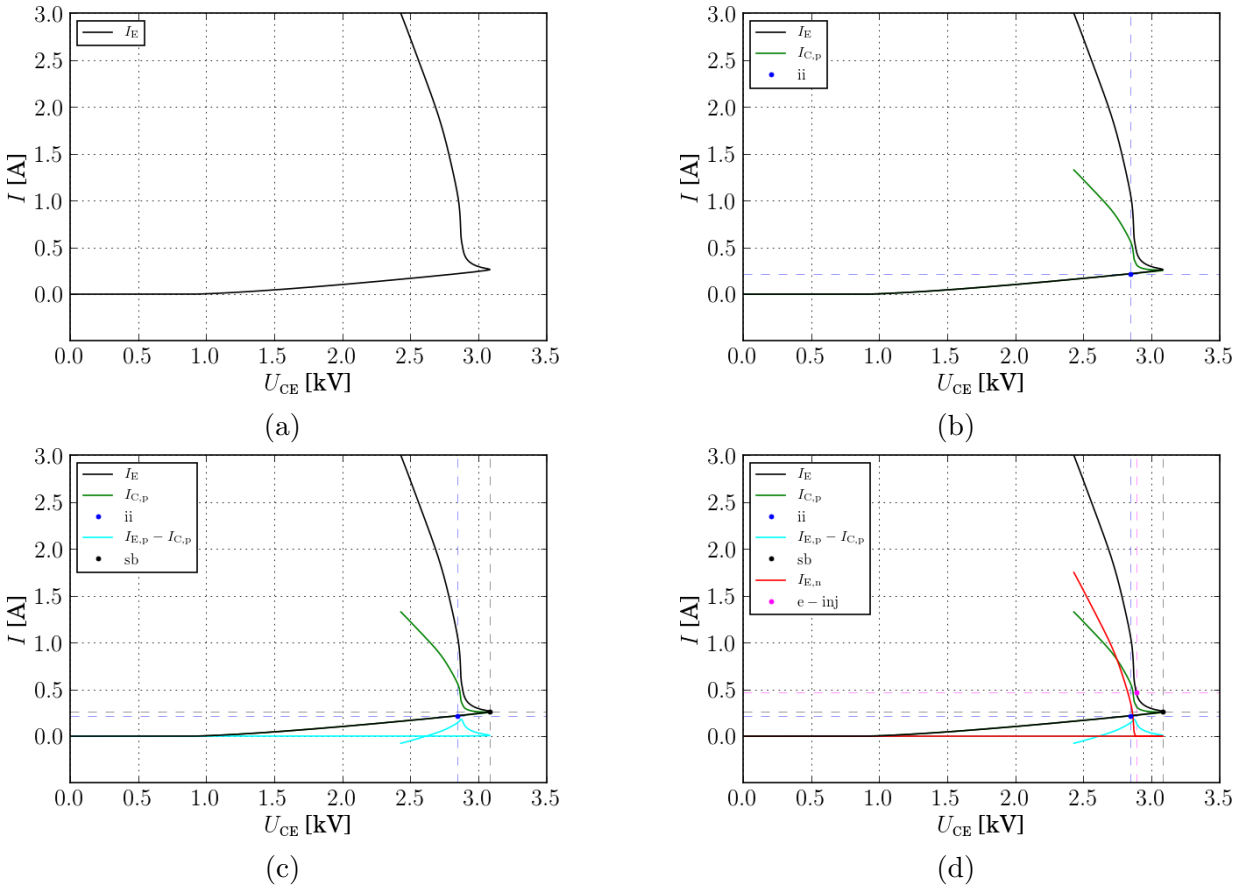

Figure 7.5: Static IV-characteristics of a cylindrical simulation structure with $l_{\mathrm{tr}} = 5.4\mu\mathrm{m}$ ($\Delta l = 0\mu\mathrm{m}$) and a vertical extension of $l_{\mathrm{vert}} = 310\mu\mathrm{m}$ at constant homogeneous lattice temperature of $T = 423\mathrm{K}$. The total emitter current is given as a function of the collector-emitter voltage. The active area of the simulation structure was chosen to be 1% of the total area of a single IGBT chip and thus corresponds to the active area of the small structure in the turn-off simulations presented in the previous chapter.

generation processes, for example in the situation shown in Fig. 7.5.

For each Δl the qualitative physical behaviour is the same. Quantitatively however, the characteristics change significantly, as can be seen in Fig. 7.6.

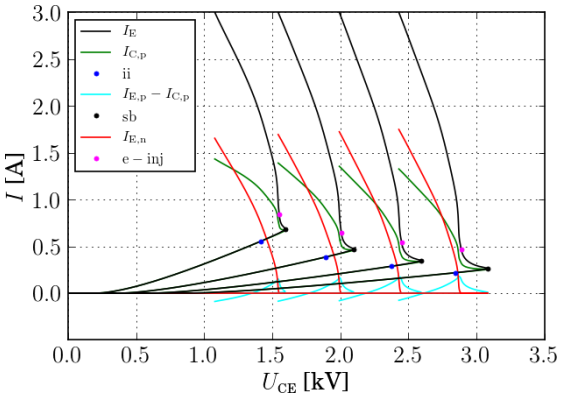

(a) $l_{tr} = 5.4\mu$m ($\Delta l = 0\mu$m)

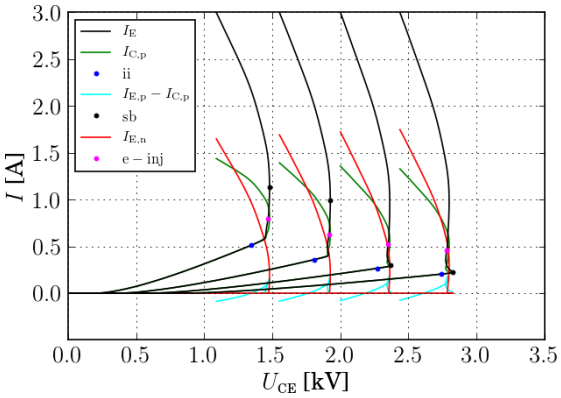

(b) $l_{tr} = 6.4\mu$m ($\Delta l = 1\mu$m)

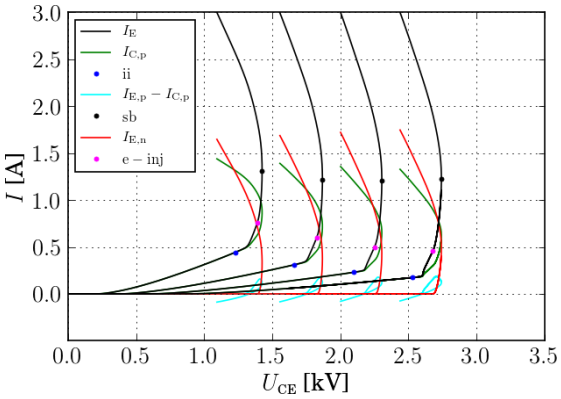

(c) $l_{tr} = 7.4\mu$m ($\Delta l = 2\mu$m)

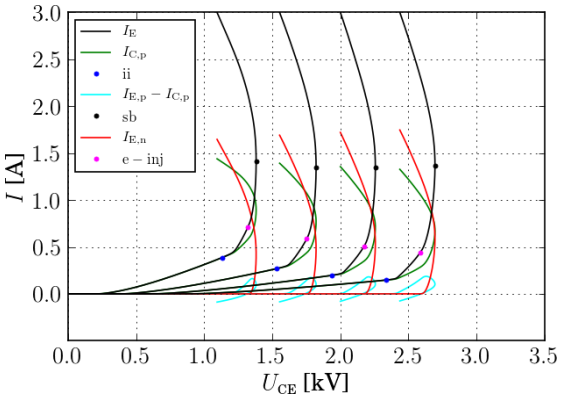

(d) $l_{tr} = 8.4\mu$m ($\Delta l = 3\mu$m)

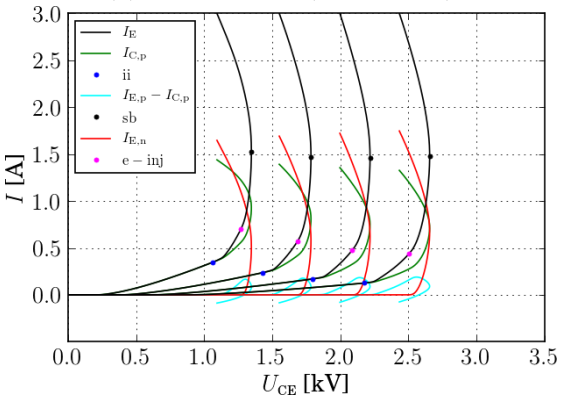

(e) $l_{tr} = 9.4\mu$m ($\Delta l = 4\mu$m)

Figure 7.6: Composition of the emitter current I_E at the central cell for five different trench-depths (a)-(e) for four different vertical extensions of $l_{vert} = 150, 200, 250, 300\mu$m each, along with significant points in the static characteristics. Onset of impact ionization (ii), point of snap-back (sb), onset of emitter-side injection of electrons (e-inj.). Note that the term $I_{E,p} - I_{C,p}$ gives the hole current at the emitter deriving from generation/recombination processes (net generation) inside of the device.

The first part of the static characteristics, as introduced in equation 7.2, spans over a rather large voltage range and the entire current at the emitter consists of holes injected from the collector side. It is qualitatively the same for all Δl and all vertical extensions of the simulation structure as it derives from the electric field inside of the device: the *pn*-junction located at the back-side of the device is forward biased and holes can enter the device and move towards the emitter contact. As the electric field strength, i.e. the voltage that can be supported by the device, depends on the vertical extension of the simulation structure as can be seen in Fig. 7.6. At a given collector-emitter voltage, simulation structures with a smaller vertical extension exhibit higher field strengths at the back-side, leading to higher hole current densities at the collector side and, consequently, at the emitter side. Taking into account the local doping (n^-) as well as the holes injected from the collector side, the voltage drop U_{AB} between two points A and B along a vertical cut through the IGBT in y-direction (vertical direction) is given by

$$U_{AB} = \frac{1}{\varepsilon} \int_A^B \mathrm{d}y \int_0^y \mathrm{d}\xi \left(p(\xi) - n(\xi) + N_\mathrm{D}^+(\xi) \right) \tag{7.3}$$

No electrons are generated in this part of the characteristics, i.e. $n = 0$, meaning that the entire voltage is sustained by the holes injected from the collector side. The voltage ramp causes the electric field to build up and more holes are injected from the collector side. At one point, the electric field strength is high enough to generate electron-hole pairs at the trench bottoms, impact ionization sets in. At this point in the characteristics, the hole current at the emitter and the hole current at the collector become different from each other. The additional current component due to carrier pair generation becomes different from zero.

The second part of the static characteristics, as introduced in equation 7.2, takes the current component due to impact ionization at the trench bottoms into account. An additional current component at the emitter is formed by holes from the impact ionization and holes from the back-side due to injection after electron absorption in addition to hole injection due to electric field alone. The electrons from the injection at the trench-bottoms cause the electric field to drop in this region, which is the well-known effect of field bending. In this region the carrier generation rate is larger than the carrier recombination rate and generation processes set in more pronounced (slope is higher) for structures with smaller vertical extensions (for equal trench depths). However, with higher vertical extension, the total amount of generation processes is higher. As the hole current density at the emitter

side rises it eventually surpasses the threshold value for electron injection from the emitter side. This is a necessary precursor to device latch-up and important for determining the safe-operating area. A more detailed look at the localization of the impact-ionization

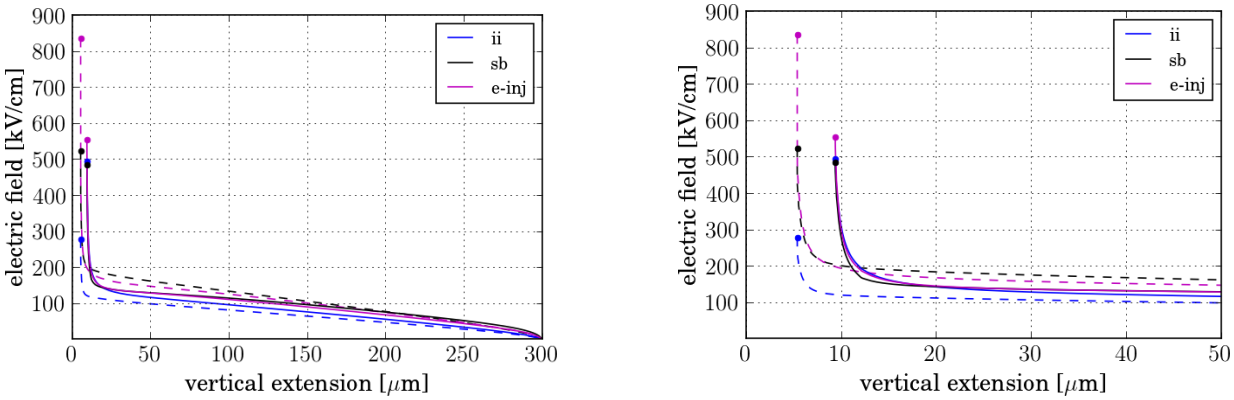

Figure 7.7: Electric field in vertical cutline through the middle of the trench at the beginning of impact ionization (blue) as well as at the beginning of emitter side injection of electrons (red) for a deep trench (solid lines) as well as for a shallow trench (dashed lines).

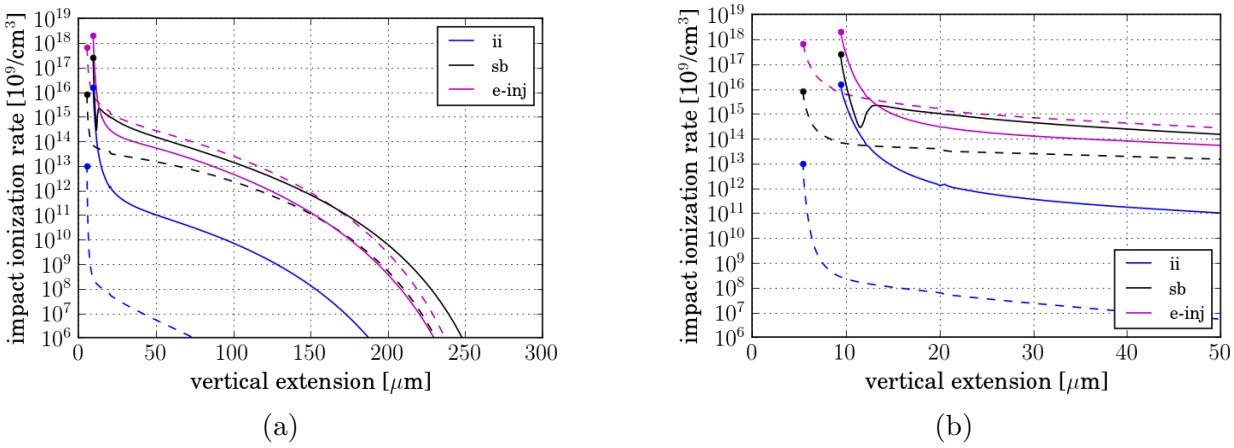

Figure 7.8: Impact ionization rate along a vertical cutline through the middle of the trench in a cylindrical structure at the beginning of impact ionization (blue) as well as at the beginning of emitter side injection of electrons (red) for a deep trench (solid lines) as well as for a shallow trench (dashed lines) (a) over the entire simulation structure and (b) at the front side of the simulation structure with vertical extension of 310μm.

regions shows, that the vertical extension of these regions significantly depends on the geometry of the trench and thus Δl, as is shown in Figs. 7.7 and 7.9, respectively. With increasing Δl, the trench bottom lies increasingly inside the base layer and thus the electric

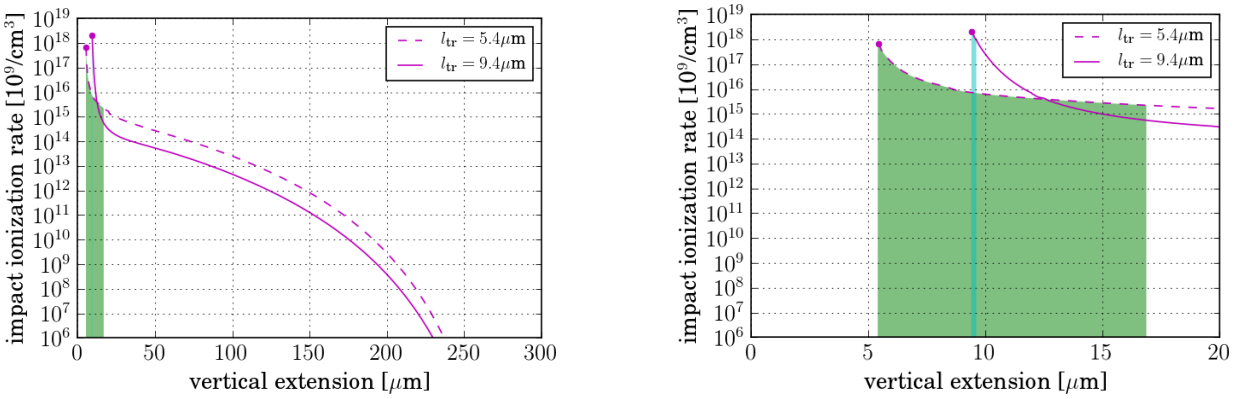

(a) (b)

Figure 7.9: (a) Comparison of integral impact ionization rates along vertical cutlines through the simulation structure at the onset of emitter side injection of electrons for trench depths of 5.4μm and 9.4μm (i.e. $\Delta l = 0\mu$m and $\Delta l = 4\mu$m), respectively. The cyan and green coloured areas beneath the curves have the same area, thus giving a 1-dimensional estimate of the vertical extension of the region in which electron-hole pair generation takes place. The reference area chosen in this picture derives from integration of the impact ionization rate of the 9.4μm structure between vertical extensions of 9.4μm and 10.4μm, i.e. 1μm beneath the trench bottom. Figure (b) gives a close-up view of (a) for small vertical extensions only. From this comparison it is clearly visible that pair generation generation is much more pronounced in the case of a deep trench, i.e. for larger Δl.

field is more pronounced in this region, leading to a sharply localized peak in impact-ionization. This in turn leads to generation processes at smaller collector-emitter voltages which results in visibly different static characteristics. Especially the regions which exhibit a negative differential resistivity are reduced with increasing Δl, as can be seen in Figs. 7.6 and which will be discussed in more detail in the next section.

Very high field peaks develop at the trench bottom for structures with a deep trench due to the large relative distance between the trench bottom and the *p*-float region. Hence, a large percentage of the overall impact ionization rate along a vertical cutline through the device is located at the trench bottom, whereas in simulation structures with a minimal relative distance between trench bottom and *p*-float region, a less pronounced peak in electrical field strength results and, consequently, a larger extension of regions with impact ionization, as can be seen in Fig. 7.9.

The next part in the static characteristics is the one where electron injection from the emitter side becomes relevant. Here the source-body *pn*-junction becomes forward biased

due to an excessive amount of holes beneath the source. In addition to high hole density beneath the contact hole, a high electron density builds up leading to an overall high injection of carriers. This high carrier concentration favours Auger recombination especially inside and beneath the source as well as within the region of high electron current density. Electron injection, as opposed to hole injection, flattens the electric field which is clearly visible along a vertical cutline through the device as can be seen in Fig. 7.7. Due to the external voltage ramp, more holes have to be delivered in order for the collector-emitter voltage to rise. Subsequently the snap-back voltage is reached. At this point in the simulation boundary condition switching takes place, i.e. instead of a voltage ramp a current ramp is conducted. The amount of electron current rises considerably and the electrical field strength decreases because of the high amount of injected electrons, hence the collector-emitter voltage and thus the impact-ionization rate decrease considerably. This results in the formation of a stable plasma channel along the vertical direction of the device underneath a trench. The development of a plasma channel is equivalent to device latch-up and consequently equivalent to device failure.

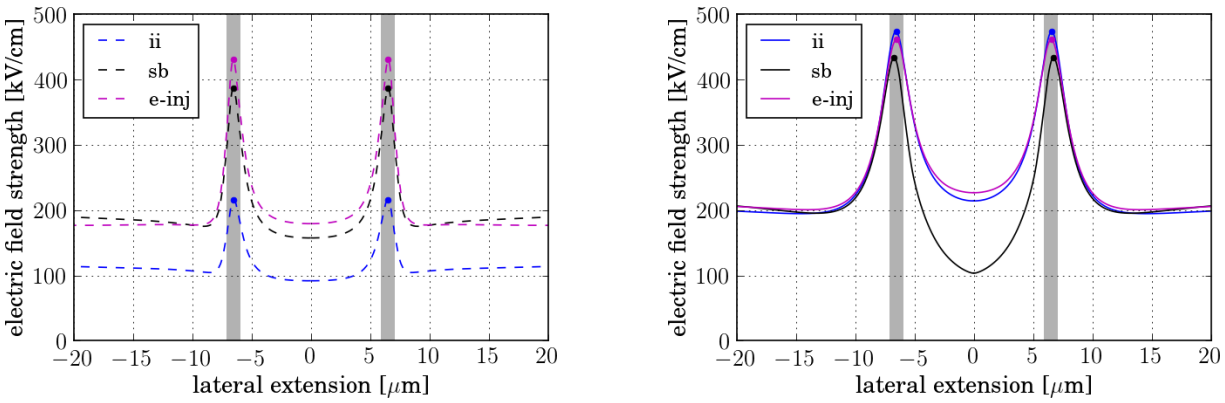

Figure 7.10: Electric field strength as a function of the lateral extension of the simulation structure at three different points in the static characteristics: at the onset of impact ionization (ii), at the snap-back voltage (sb) as well as at the onset of emitter-side injection of electrons (e-inj) for a simulation structures with (a) $l_{\mathrm{tr}} = 5.4\mu\mathrm{m}$ (i.e. $\Delta l = 0\mu\mathrm{m}$) and with (b) $l_{\mathrm{tr}} = 9.4\mu\mathrm{m}$ (i.e. $\Delta l = 4\mu\mathrm{m}$). The vertical extension of the structures amount to $l_{\mathrm{vert}} = 300\mu\mathrm{m}$ in both cases.

7.3.1 Current Densities at Central Emitter Contact

So far, the goal was to discriminate between the different current components existing at all emitter contacts so only the total current there was considered. For a physical description of the static characteristics the electrical current density at the central emitter contact only gives insight into the physical processes and moreover, it constitutes a better quantity for the comparison of these simulations with the transient turn-off simulations. The current density can be inhomogeneously distributed over the lateral extension of the device, as was already mentioned in the previous chapters. From the design of the auxiliary simulation structure, the cell of interest is the innermost cell in accordance with the turn-off simulations using cylindrical symmetry. The active areas, i.e. the measures of the geometry are chosen to be the same as in the transient turn-off simulations, which facilitates the quantitative comparisons between these two approaches.
Within the static characteristics regions with negative differential resistivity are of special interest as these regions characterise operating conditions in which the IGBT is in an unstable state. In such an operating region the device has a tendency to generate current filaments. Universally speaking, there are regions with increased current density and regions with reduced current density inside of the device. These inhomogeneities strongly depend on the geometry of the simulation structure as was already mentioned earlier in this chapter, as physical effects like impact ionization, carrier recombination and the emitter-side injection of electrons can change the characteristics. As was already shown in Fig. 7.4, the threshold in hole current density at the central emitter contact is not changed by the geometrical variations. As can be seen in Figs. 7.11 and especially in Figs. 7.12, a variation of Δl significantly determines whether a certain point in the static characteristics lies within a region of negative differential resistivity or not. In general, the higher the value for Δl, the more stable the device is, i.e. the less regions with negative differential resistivity arise, as Figs. 7.11 suggest. This is in agreement with the results obtained by transient turn-off simulations where it was found, that with increasing Δl the current flow becomes less inhomogeneous and thus the threshold for device latch-up increases significantly. This is due to the fact that the generation of electrons due to impact-ionization sets in at an overall lower collector-emitter voltage which causes the electrical current density at the central emitter to have a non-negative slope. The variation of Δl does not change the current densities at which impact-ionization and emitter-side injection of electrons, respectively, takes place, as can be seen in Fig. 7.11f. The current density at which snap-back of the device occurs, however, is affected substantially by a variation of Δl.

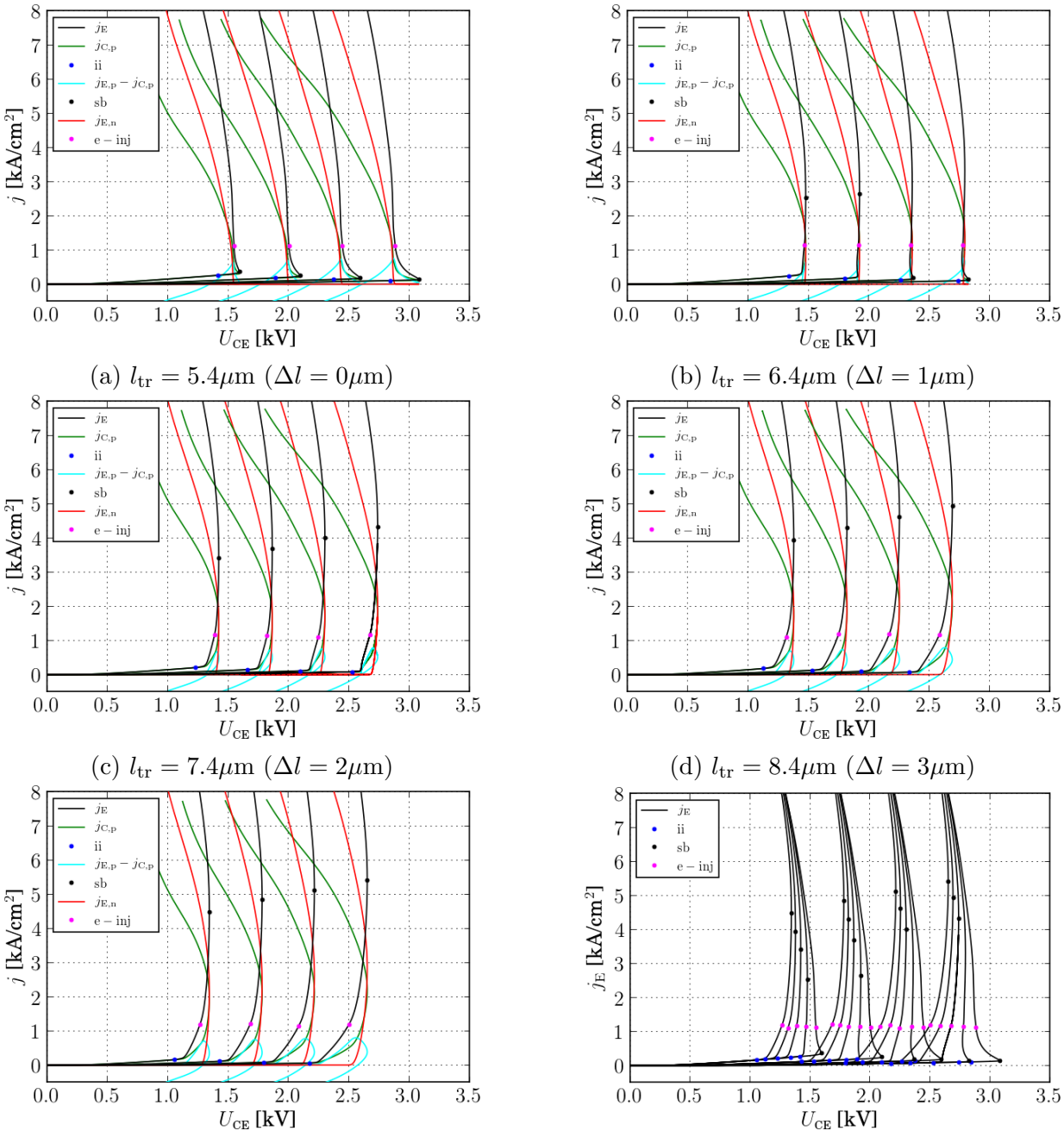

(a) $l_{tr} = 5.4\mu m$ ($\Delta l = 0\mu m$)

(b) $l_{tr} = 6.4\mu m$ ($\Delta l = 1\mu m$)

(c) $l_{tr} = 7.4\mu m$ ($\Delta l = 2\mu m$)

(d) $l_{tr} = 8.4\mu m$ ($\Delta l = 3\mu m$)

(e) $l_{tr} = 9.4\mu m$ ($\Delta l = 4\mu m$)

(f)

Figure 7.11: Cylindrical structure. Current densities at the central emitter contact as a function of the collector-emitter voltage. Each diagram shows characteristics of four different vertical extensions of the current filaments: 150μm, 200μm, 250μm and 300μm. Furthermore, the vertical extension of the trench l_{tr}, is increased from 5.4μm to 9.4μm in steps of 1μm, c.f. (a)-(e). The composition of the total current density at the emitter contact is shown along with significant points within the static characteristics. As can be seen, the vertical extension of the trench has a considerable influence on the characteristics. Note that the threshold for the emitter-side injection of electrons does not change. See Figs. 7.4 as well.

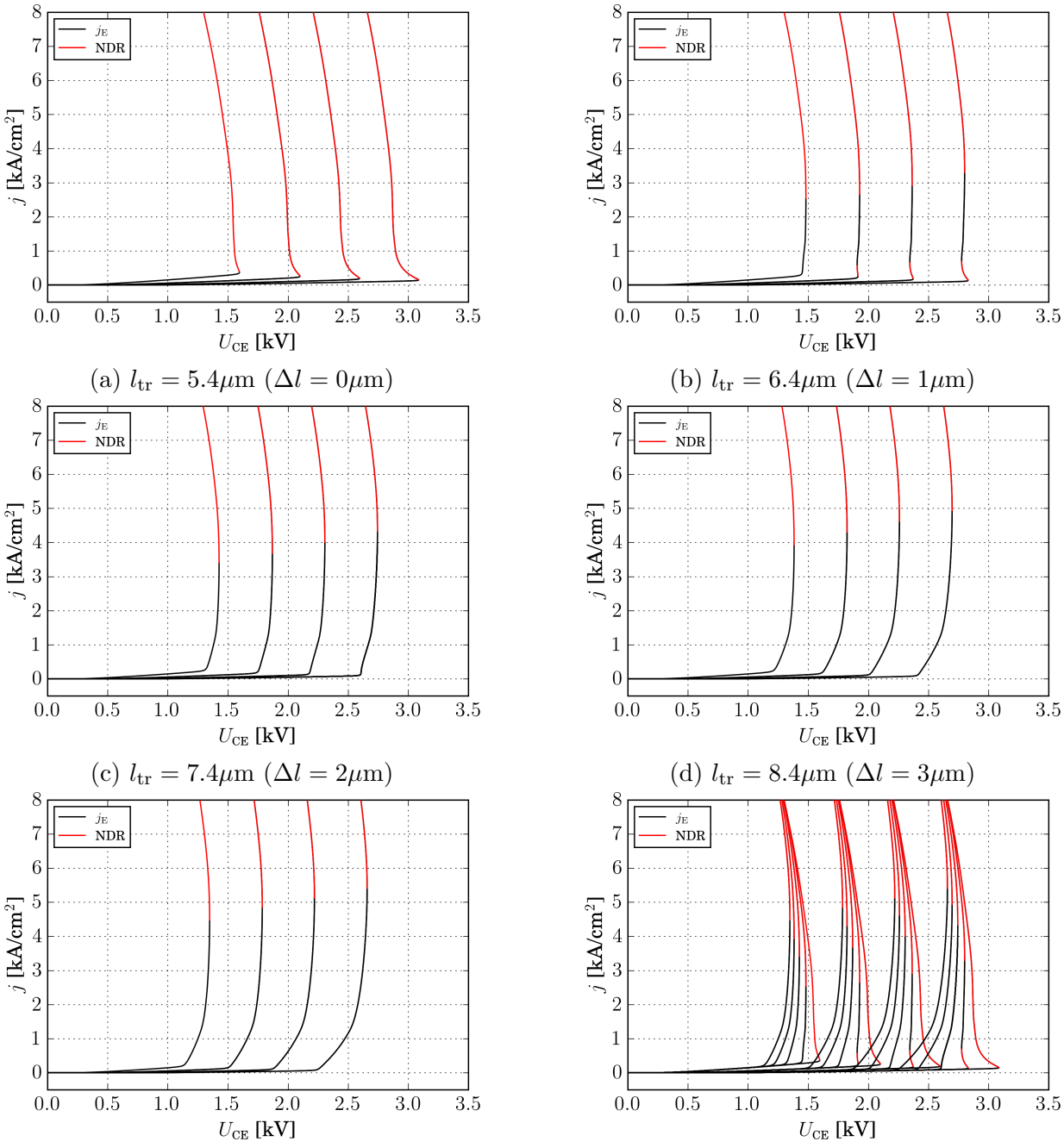

(a) $l_{tr} = 5.4\mu m$ ($\Delta l = 0\mu m$)

(b) $l_{tr} = 6.4\mu m$ ($\Delta l = 1\mu m$)

(c) $l_{tr} = 7.4\mu m$ ($\Delta l = 2\mu m$)

(d) $l_{tr} = 8.4\mu m$ ($\Delta l = 3\mu m$)

(e) $l_{tr} = 9.4\mu m$ ($\Delta l = 4\mu m$)

(f) $l_{tr} = 5.4, 6.4, 7.4, 8.4$ and $9.4\mu m$

Figure 7.12: Current densities at the central emitter contact as a function of the collector-emitter voltage. Each diagram shows characteristics of four different vertical extensions of the current filaments: 150μm, 200μm, 250μm and 300μm. Furthermore, the vertical extension of the trench l_{tr}, is increased from 5.4μm to 9.4μm in steps of 1μm, c.f. (a)-(e). Regions exhibiting negative differential resistivity are displayed in red. A strong dependence on the trench-depth is clearly visible. (f) gives a direct comparison of the scenarios depicted in (a)-(e). (cf. Figs. 7.11.)

(a) (b)

Figure 7.13: Close-up view of the front side of the device depicting (a) the electric current density shortly before device latch-up and (b) the corresponding Auger recombination rate. The emitter-side injection of electrons as well as the increased carrier recombination rates due to the high carrier densities alongside the line of injection are clearly visible.

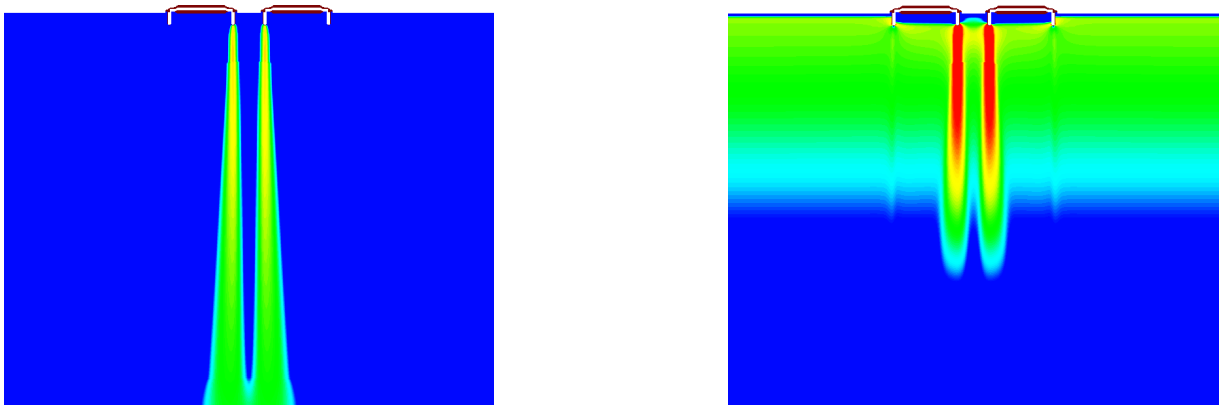

(a) (b)

Figure 7.14: (a) Absolute value of electron current density and (b) impact ionization rate of a 5.4μm trench-depth structure at the point of snap-back. The collector-emitter voltage in this case amounts to 1.59kV and the total electric current density amounts to 0.44kA/cm^2. The vertical extension of the simulation structure depicted here is 150μm. Note that the collector-emitter voltage attains its maximum value at this point.

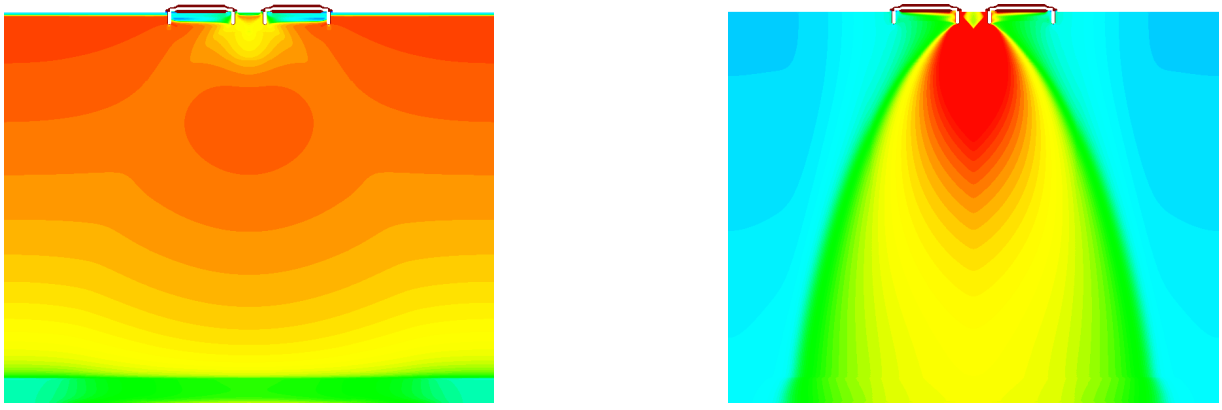

(a) (b)

Figure 7.15: (a) Electric field strength and (b) total electrical current density at the same point in the static characteristics of a 5.4μm trench-depth structure in the latch-up state. The vertical extension of the simulation structure depicted here is 150μm. The formation of a plasma channel characterizing the latching of the device along with a region of high current density are clearly visible.

7.4 Simulation of Static Characteristics in Stripe Geometry

In order to compare the influence of the overall filament geometry on the static characteristics, the same calculations as presented above where conducted in 2D-Cartesian geometry. In Figs. 7.16 the electric current density at the cell of interest in the auxiliary simulation structure is depicted as a function of the collector-emitter voltage. The results show that the geometry itself does not affect the characteristics qualitatively: the physical effects and the current density constituents at the emitter contact deriving from them are the same. The collector-emitter voltages at which the respective effects set in differ by a few percent only.

Quantitatively however, big differences are present as can be seen in a direct comparison given in Figs. 7.17. While the current densities at the onset of impact ionization are fairly close to each other in both geometries, the current densities at the onset of emitter-side injection of electrons and snap-back differ considerably from each other. Here, the influence of filament-geometry becomes especially obvious as the focussing of carriers is much more pronounced in cylindrical geometry, as was already described earlier.

Concerning the qualitative differences which arise due to the variation of Δl, simulations using 2D-Cartesian geometry reproduce the results obtained by using cylindrical geometry, especially for regions with negative differential conductivities. From this it can be concluded that a variation of Δl within a range of a few micrometers does not result in different physical effects.

As can be shown by additional calculations, increasing the trench-depth and the p-float doping by the same amount (on the range of a few micrometers), thus leaving their relative distance towards each other $\Delta l = 0$, change the static behaviour of the IGBT insignificantly only.

It has to be pointed out that this approach does not account for physical effects of self-heating and therefore local temperature inhomogeneities and an increased effective intrinsic carrier density as the calculations are isothermal and not self-consistent. The restrictions this poses on the overall analysis of the limits of the safe-operating area are subject to the next chapter.

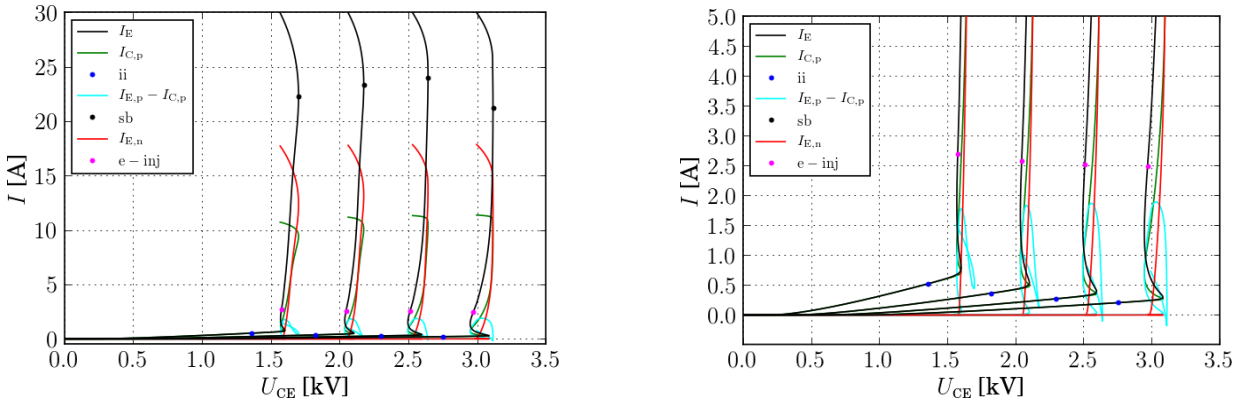

(a) (b)

Figure 7.16: Static characteristics of a simulation structure in stripe geometry with $l_{tr} = 5.4\mu$m and vertical extensions of $l_{vert} = 150, 200, 250, 300\mu$m in (a) full view and (b) in a more detailed view of smaller current densities. Note the significant quantitative differences to the simulation structures in cylindrical geometry.

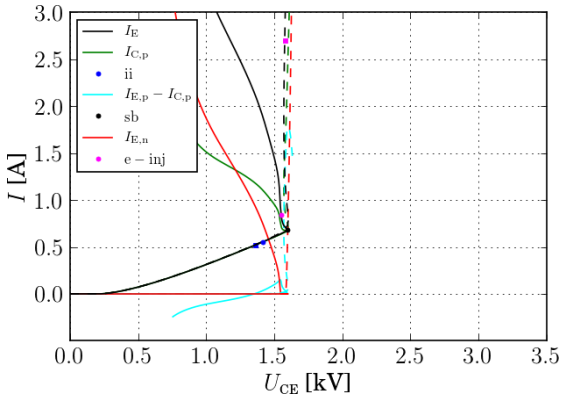

(a) $l_{tr} = 5.4\mu$m ($\Delta l = 0\mu$m), $l_{vert} = 150\mu$m

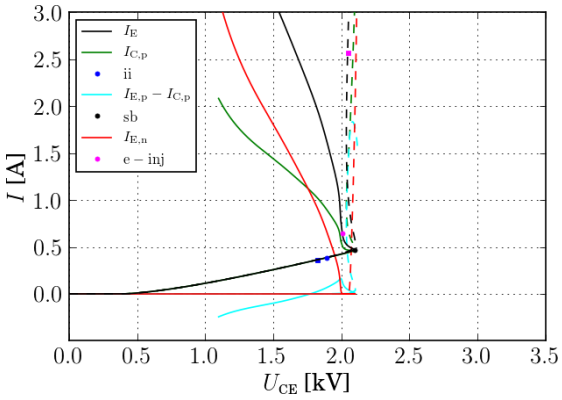

(b) $l_{tr} = 5.4\mu$m ($\Delta l = 0\mu$m), $l_{vert} = 200\mu$m

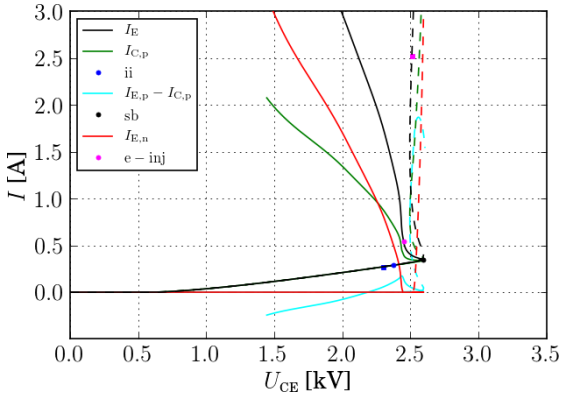

(c) $l_{tr} = 5.4\mu$m ($\Delta l = 0\mu$m), $l_{vert} = 250\mu$m

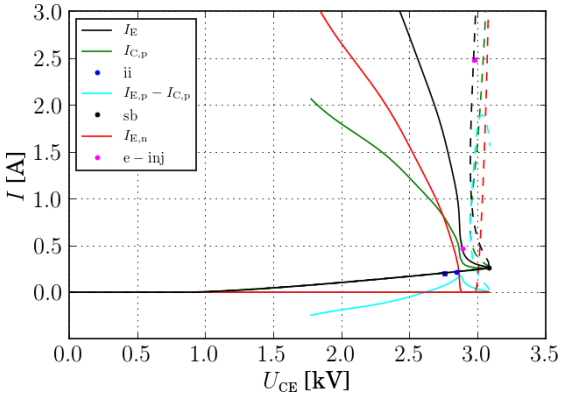

(d) $l_{tr} = 5.4\mu$m ($\Delta l = 0\mu$m), $l_{vert} = 300\mu$m

Figure 7.17: Direct comparison of static characteristics of cylindrical (solid lines) and stripe (dashed lines) geometry for different vertical extensions (a) $l_{vert} = 150\mu$m (b) $l_{vert} = 200\mu$m (c) $l_{vert} = 250\mu$m and (d) $l_{vert} = 300\mu$m. Besides the quantitative differences, the qualitative behaviour does not exhibit a significant dependency on the geometry, as the voltages at which impact ionization, electron injection as well as snap-back occur are comparable (cf. Figs. 7.16).

8. Comparison of Transient Turn-Off Simulations and Static Characteristics

This chapter aims at comparing the approaches of transient turn-off simulations (cf. chapters 5 and 6) and static characteristics (cf. chapter 7) with respect to their differences from a physical point of view. The geometry of the simulation structure as well as the impact of geometrical variations in the trench depth, i.e. Δl, itself play a minor role in this chapter as their influence on the safe-operating area was already discussed in detail. Furthermore, both approaches are applicable to any simulation geometry.
This chapter will be structured as follows: starting from the initial physical situation that is common to both approaches a direct comparison of the predictions of the safe-operating area will be given. This is followed by a discussion about the shortcomings of either approach.

8.1 Differences of Approaches

As opposed to the transient turn-off simulations the approach using static characteristics makes use of auxiliary simulation structures which feature the innermost cells only. As has already been mentioned in the previous chapter, this does not make a significant difference as the cells surrounding the innermost cell play a minor role only. In turn-off simulations, the use of an auxiliary structure is not applicable due to the fact that an initially homogeneous current density inside of the device can not be achieved therein. The replacement of electron-hole plasma by p-emitter doping in static simulations, which basically determines the vertical extension of the current filament is a significant difference between the both approaches, yet the physical situation both aim to reproduce is the same. The step-wise increasing of the vertical extension of the simulation structure imitates the extension of the space-charge region as a function of time. A depiction of the same situation in tran-

sient turn-off simulations and static characteristics is given in Figs. 8.1. Here the vertical extension of the current filament(s), i.e. the vertical extension of the space-charge region, is depicted for those points in time corresponding to the vertical extension of the auxiliary simulation structures.

The focus of a comparison of these approaches is to determine regions where current filaments can occur, i.e. the regions which have a negative differential conductivity. A comparison of the collector current as a function of the collector-emitter voltage in the static characteristics and the corresponding temporal behaviour of the collector emitter voltage is given in Figs. 8.2. The movement of current filaments itself does not play a significant role what the limits of the safe-operating area is concerned, as was discussed in chapter 5. In the static characteristics, the rate of change of all physical quantities with respect to time is zero. In a snapshot during transient turn-off this situation is not reached, but the behaviours are the same for long enough times in case the collector current, the collector-emitter voltage and the gate-emitter voltage are fixed at the point the snapshot is taken.

Considering this, one obvious difference between the two approaches is the distribution of lattice temperatures. Not only is the lattice temperature in the static characteristics fixed at 423K, but it is not possible to simulate an inhomogeneous lattice temperature distribution. This shortcoming becomes more relevant the more the lattice temperature distribution is inhomogeneous. This is the case with increasing time since the beginning of turn-off. Therefore one can expect larger discrepancies between the approaches for larger vertical extensions of the current filaments. Additionally physical quantities that exhibit a dependency on lattice temperature are affected by this as well, such as the impact ionization beneath the trenches. Here, the local increase in lattice temperature is especially pronounced.

Another difference which makes a comparison of both approaches more sophisticated is the fact, that in transient turn-off simulations current filaments are not bound to be located at the central emitter contact at all times except for the point of latch-up. This suggest, that the predictions made by the two different approaches may deviate for other times but are the same if the device runs into latch-up.

The influence of a locally inhomogeneous lattice temperature on the limits of the safe-operating area can only be approximated in self-consistent electro-thermally coupled transient turn-off simulations as static characteristics assume isothermal conditions only. An obvious qualitative difference arising from an inhomogeneous lattice temperature distribu-

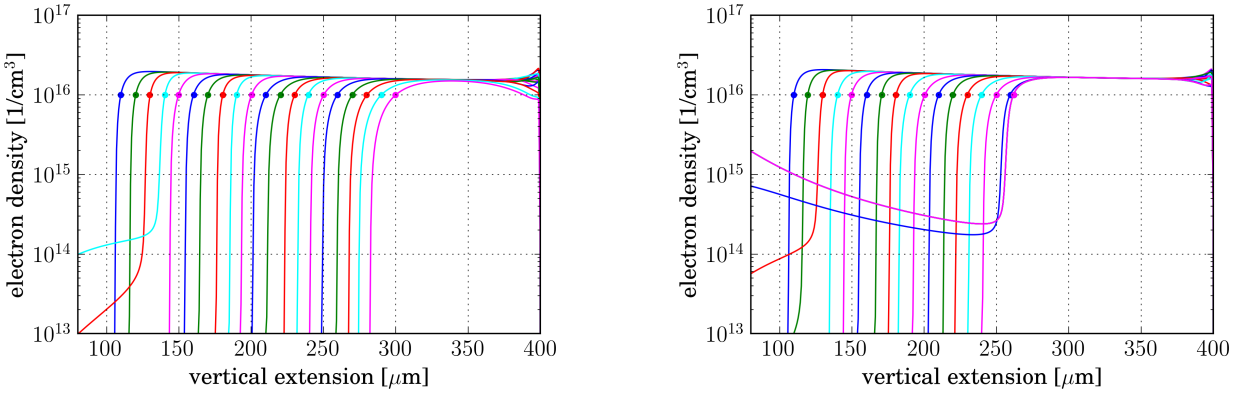

(a) (b)

Figure 8.1: Vertical extension of the electron-hole plasma as a function of time during the turn-off process of a 5.4μm trench structure. The beginning of the electron hole plasma marks the vertical extension of the space-charge region and thus the vertical extension of the current filament. The situations depicted here correspond to the series of static characteristics, i.e. to those situations where the vertical extensions of the current filaments matches the vertical extensions of the simulation structures in the static case. (a) shows a turn-off process from an initial current density of 100A/cm^2 for times between 0.8μs to 2.2μs. (b) shows a turn-off process from an initial current density of 110A/cm^2 for times between 0.8μs to 1.8μs, where the device runs into latch-up. The simulation structure is the same for both situations.

tion is the rise of moving current filaments, which themselves do not significantly influence the threshold for latch-up. However, as the time-scales for thermal processes are are much longer than the time-scales for electrical processes, a rise in lattice temperature results from a rise in current densities. This rise itself, i.e. a very high rate of change of current density with respect to time as theoretical investigations suggest, can be fast enough to lead to destruction by thermal runaway before filaments start to move.

As introduced in the previous chapter, this approach assumes a p-emitter that has no dependence on the lateral extension of the device. Thus a slightly non-rectangular shape of the electron-hole plasma as it occurs in the transient turn-off simulations is not taken care of. This has only little influence on the current density components at the contacts.

8.2 Comparison of Current Densities

A comparison of the same physical situation using the two different approaches for the simulation of the turn-off process within and beyond the safe-operating area of a cylindrical

structure with trench depth of 5.4μm will now be given. This structure was chosen as the limits of the safe-operating area as predicted by transient turn-off simulations are in good agreement with measurement results, cf. chapter 6. Here, the current densities at the central emitter contact versus the corresponding collector-emitter voltage using time as a parameter is used for the comparison. Figs. 8.2 show the constitution of the current densities at the central emitter contacts. Especially in the case of device latch-up a comparison can be made, showing the current densities as well as the vertical extension of the current filament and the corresponding collector-emitter voltage at which destruction of the device takes place. For completeness, as has already been introduced, the active areas are the same in both cases.

Fig. 8.3 depicts a comparison of the significant points which were introduced in the previous chapter for the total current through the simulation structures in both approaches along with the regions of negative differential conductivity. Here, the filamentary current flow through the structure where the static characteristics exhibit a negative slope is especially visible.

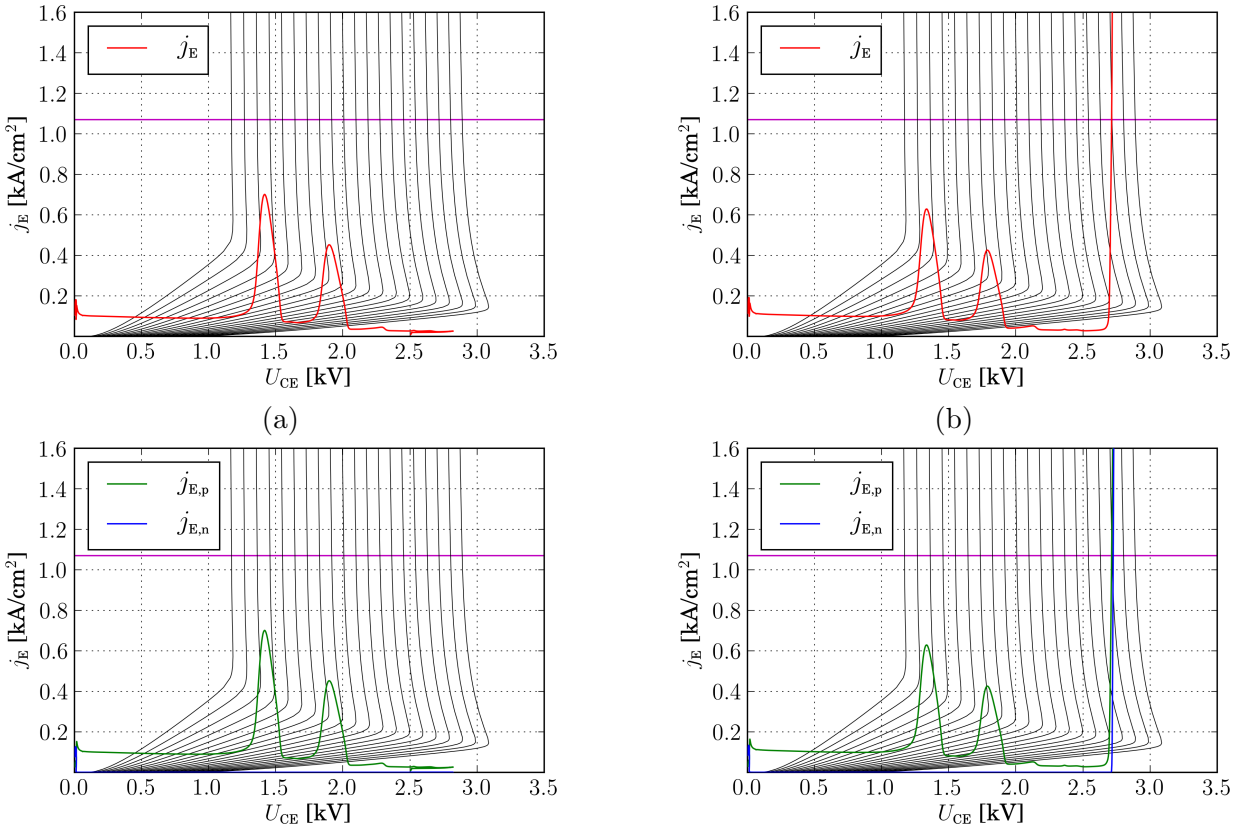

Figure 8.2: Comparison of the static characteristics of a 5.4μm trench-depth structure for various vertical extensions of the simulation structure with the transient characteristics of the collector-emitter voltage. (a) depicts the device turn-off from an initial current density of 100A/cm^2 which does not result in a destruction of the device. (b) depicts turn-off from an initial current density of 110A/cm^2 which does result in a destruction of the device due to latch-up. (c) and (d) depict the current densities at the central emitter contact for electrons and holes, respectively, of the same process. Here, the pink line indicates the threshold in hole current density for the emitter side injection of electrons. In (c) no emitter-side injection of electrons at the central emitter takes place as the threshold is never surpassed. In (d), however, the threshold is surpassed and the subsequent injection of electrons leads to latch-up of the device. The static characteristics for filament lengths of 110μm to 300μm in steps of 10μm are identical for (a)-(d). The filament length at the point of latch-up amounts to around 280μm, which is in good agreement with Fig. 8.1b.

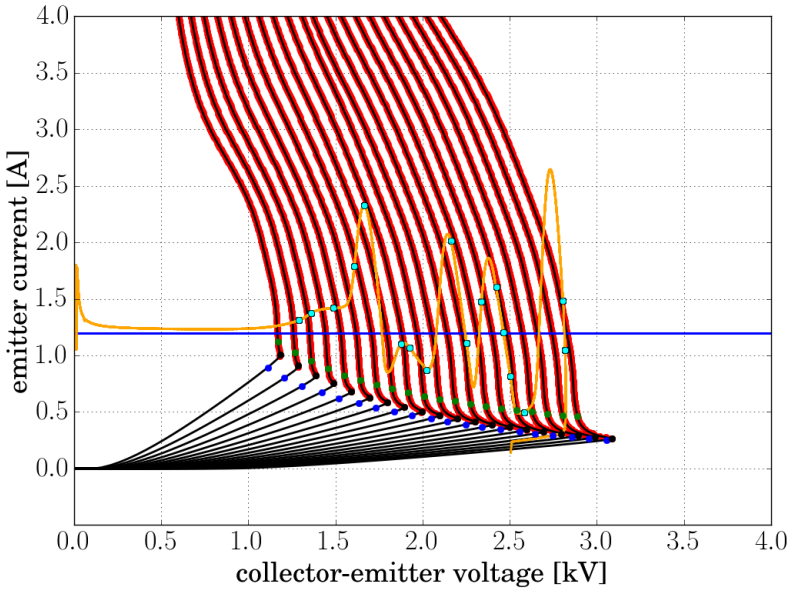

Figure 8.3: Direct comparison of static characteristics (solid black lines) for several vertical extensions and the transient turn-off behaviour $U_{\mathrm{CE}}(t)$ (solid orange line) of a simulation structure with 5.4μm trench-depth in cylindrical geometry. Marked in red are the regions exhibiting a negative differential conductivity, whereas the solid blue line indicates the threshold in current density at the emitter contact at which latch-up occurs. The blue points indicate the onset of impact-ionization, the black dots the snap-back and the green dots the onset of emitter-side injection of electrons. The points indicate the electrical current densities and the respective collector emitter voltages in the transient process at a vertical extension of the space-charge region which corresponds to the vertical extension of the simulation structure in the static characteristics. The DC-link voltage in this case amounts to 2.5kV.

8.3 Shortcomings of Both Approaches

In this section, the shortcomings of both approaches, the transient turn-off simulation as well as the simulation of the static characteristics with respect to the real experimental situation will be discussed. Common to both approaches is the approximation of the chip geometry itself, meaning that they are no fully 3D simulations of the self-consistent turn-off behaviour of the real chip. The transient turn-off simulations as well as the simulation of a series of static characteristics approximate this real 3D-structure by using a cylindrical geometry which basically assumes a rotationally invariant shape of the current filament with respect to the vertical central axis of the IGBT, i.e. the axis of revolution. Judged by the results obtained for the limits of the safe-operating area, this approach reproduces experimental results fairly good as opposed to the results obtained by simulations using a 2D-Cartesian geometry.
In the static characteristic of simulation structure's single instance (at a fixed vertical extension of a current filament) the temporal behaviour is not considered as the characteristics are stationary. This, along with the isothermal conditions, is a major shortcoming of this approach. However, the entire approach using a series of static characteristics (with a step-wise increase of vertical extension of the current filament) replicates the temporal behaviour to some extent.

9. Conclusion and Outlook

As the results presented in this work suggest, the geometrical shape of current filaments have a strong influence on the threshold for device latch-up and as such, on a quantitatively correct modeling of the safe-operating area. Therefore, the exact geometrical shape of filaments, as they occur inside a multi-cell array, has to be simulated. This can only be done by taking into account the exact geometric shape including doping profiles and trench geometry of a part of the IGBT chip, which, in turn, has to be chosen large enough to fully comprise at least one single current filament. Moreover, these numerical simulations have to be self-consistent and transient with highly resolved time-stepping to give a high-fidelity visualization of turn-off and to allow for a detailed analysis of it. In particular, the underlying physical effects such as impact-ionization triggered by high electric field peaks and the strong injection of charge carriers resulting from it must be properly modeled.
The simulations presented in this work yield an approximate description of the real three-dimensional situation inside IGBT cells and the three-dimensional shape of current filaments resulting from it. These approximations rely, in one way or another, on assumptions concerning the spatial symmetry of current filaments, which significantly reduces the complexity of the calculations and, therefore, the computational expense to obtain reliable results. As the geometrical shape of a current filament has a significant influence on the latch-up threshold, special attention has to be paid to those regions within a cell where in consequence of the cell design very high electric field peaks may build up. This phenomenon cannot be covered by either a stripe or a cylindrical geometry, because they occur primarily in the "corners" of a trench, where high electric field peaks and a strong carrier injection caused by the high curvature of the cell boundary can potentially exist simultaneously. A full numerical analysis and theoretical description of these effects is left to future research in this field.

Publications

Töchterle, C., Pfirsch, F., Sandow, C., Wachutka, G.:
"*Analysis of the Latch-up Process and Current Filamentation in High-Voltage Trench-IGBT Cell Arrays*",
International Conference on the Simulation of Semiconductor Processes and Devices (SISPAD), pp. 296-299, (2013), Glasgow, UK

Töchterle, C., Pfirsch, F., Sandow, C., Wachutka, G.:
"*Evolution of Current Filaments Limiting the Safe-Operating Area of High-Voltage Trench-IGBTs*",
International Symposium on Power Semiconductor Devices and ICs (ISPSD), pp. 135-138, (2014), Waikoloa, USA

Sandow, C., Baburske, R., Niedernostheide, F.-J., Pfirsch, F., Töchterle, C.:
"*Exploring the Limits of the Safe Operation Area of Power Semiconductor Devices*",
International Conference on the Simulation of Semiconductor Processes and Devices (SISPAD), pp. 49-52, (2014), Yokohama, Japan

Töchterle, C., Pfirsch, F., Sandow, C., Wachutka, G.:
"*Influence of Quasi-3D Filament Geometry on the Latch-Up Threshold of High-Voltage Trench-IGBTs*",
International Conference on the Simulation of Semiconductor Processes and Devices (SISPAD), pp. 177-180, (2016), Nuremberg, Germany

Acknowledgements

I would like to express my appreciation to Dr. Frank Pfirsch at Infineon Technologies AG (Neubiberg) for his valuable and much appreciated work supervising my research leading to this thesis as well as for numerous technical discussions, critical questions and feedback, physical insights, new ideas and encouragement for pursuing new approaches.

I am also thankful to Prof. Dr. Gerhard Wachutka at the Technical University of Munich for giving me the opportunity to work and pursue my research at the chair for Physics of Electrotechnology.

I would like to extend my sincere thanks to Prof. Dr. Alessio Gagliardi at the Technical University of Munich, Dr. Marc Tornow at the Technical University of Munich and Prof. Dr.-Ing. Josef Lutz at the Technical University of Chemnitz for being part of the committee and for reviewing this thesis.

Special thanks go to Dr.-Ing. Franz Wittmann, Dr. Gabriele Schrag and Kathryn Clark at the Technical University of Munich for supporting me during my time at the TUM.

I would also like to express my sincere thanks to the team at Infineon Technologies AG (Neubiberg), namely Dr. Christian Sandow, Dr. Franz-Josef Niedernostheide, Dr. Alexander Philippou, Dr. Vera van Treek and Dr. Maria Cotorogea for their support, numerous technical discussions and valuable input.

Bibliography

[1] S. Linder. *Power Semiconductors*. EPFL Press, Lausanne, 2006.

[2] Infineon Technologies AG. *Technical Information IGBT Module FZ1500R33HL3*, 2010. Rev. 2.4.

[3] P. Rose. *Simulationsuntersuchungen zu instabilen Zuständen von IGBTs*. PhD thesis, University of Bremen, 2003.

[4] S. Milady. *Spatial and temporal instabilites in high voltage power devices*. PhD thesis, University of Bremen, 2010.

[5] A. Müller-Dauch. *Simulationsuntersuchungen zur Grenzbelastbarkeit von IGBTs im Abschaltvorgang*. PhD thesis, University of Bremen, 2010.

[6] J. Oetjen, R. Jungblut, U. Kuhlmann, J. Arkenau, and R. Sittig. Current filamentation in bipolar power devices during dynamic avalanche breakdown. *Solid-State Electronics*, 44(1):117–123, 2000.

[7] T. Shoji, M. Ishiko, T. Fukami, T. Ueta, and K. Hamada. Investigations on current filamentation of IGBTs under unclamped inductive switching conditions. In *Power Semiconductor Devices an IC's*, pages 227–230, 2005.

[8] T. Raker, H.-P. Felsl, F.-J. Niedernostheide, F. Pfirsch, and H.-J. Schulze. Limits of Strongly Punch-Through Designed IGBTs. In *23rd International Symposium on Power Semiconductor Devices and ICs*, number c, pages 100–103. Ieee, May 2011.

[9] A. Schenk. *Advanced Physical Models for Silicon Device Simulation*. Springer, Wien, 1998.

[10] D. Schröder. *Leistungselektronische Bauelemente*. Springer, Berlin Heidelberg, 2006.

[11] Synopsys Inc. *Synopsys Sentaurus Device User Guide, version G.2012-SP2.*

[12] National Institute of Standards and Technology. www.nist.gov. Accessed: December 2016.

[13] L. Huldt, N.G. Nilsson, and K.G. Svantesson. The temperature dependence of band-to-band Auger recombination in silicon. *Applied Physics Letters*, 35(10):776–777, 1979.

[14] W. Lochmann and A. Haug. Phonon-Assisted Auger Recombination in Si with Direct Calculation of the Overlap Integrals. *Solid State Communications*, 35(7):553–556, 1980.

[15] R. Häcker and A. Hangleiter. Intrinsic upper limits of the carrier lifetime in silicon. *Journal of Applied Physics*, 75(11):7570–7572, 1994.

[16] A.G. Chynoweth. Ionization Rates for Electrons and Holes in Silicon. *Physical Review*, 109(5):1537–1540, 1958.

[17] R. Van Overstraeten and H. De Man. Measurement of the ionization rates in diffused silicon p-n junctions. *Solid-State Electronics*, 13(5):583–608, May 1970.

[18] W. Shockley and W.T. Read Jr. Statistics of the Recombinations of Holes and Electrons. *Physical Review*, 87(5):835–842, 1952.

[19] R.N. Hall. Electron-Hole Recombination in Germanium. *Physical Review*, 87:387, 1952.

[20] J.G. Fossum and D.S. Lee. A Physical Model for the Dependence of Carrier Lifetime on Doping Density in Nondegenerate Silicon. *Solid-State Electronics*, 25(8):741–747, 1982.

[21] J.G. Fossum, R.P. Mertens, D.S. Lee, and J.F. Nijs. Carrier Recombination and Lifetime in Highly Doped Silicon. *Solid-State Electronics*, 26(6):569–576, 1983.

[22] H. Goebel and I .C. Hoffmann. Full Dynamic Power Diode Model Including Temperature Behavior for Use in Circuit Simulators. In *ISPSD*, number 1, pages 130–135, 1992.

[23] D.M. Caughey and R.E. Thomas. Carrier mobilities in Silicon Empirically Related to Doping and Field. *Proceedings of IEEE*, 55(12):2192–2193, 1967.

[24] C. Canali, G. Majni, R. Minder, and G. Ottaviani. Electron and Hole Drift Velocity Measurements in Silicon and Their Empirical Relation to Electric Field and Temperature. *IEEE Transactions on Electron Devices*, pages 1045–1047, 1975.

[25] C. Lombardi, S. Manzini, A. Saporito, and M. Vanzi. A physically based mobility model for numerical simulation of nonplanar devices. *IEEE Transactions On Computer-Aided Design*, 7(11):1164–1171, 1988.

[26] D.B.M. Klaassen. A unified mobility model for device simulation - I. Model equations and concentration dependence. *Solid-State Electronics*, 35(7):953–959, 1992.

[27] D.B.M. Klaassen, J.W. Slotboom, and H.C. de Graaff. Unified apparent bandgap narrowing in n- and p-type silicon. *Solid-State Electronics*, 35(2):125–129, February 1992.

[28] G. Masetti, M. Severi, and S. Solmi. Modeling of Carrier Mobility Against Carrier Concentration in Arsenic-, Phosphorus-, and Boron-lhped Silicon. *IEEE Transactions on Electron Devices*, 30(7):764–769, 1983.

[29] J.W. Slotboom and H.C. de Graaf. Measurements of Bandgap Narrowing in Si Bipolar Transistors. *Solid-State Electronics*, 19(10):857–862, 1976.

[30] J.W. Slotboom and H.C. de Graaf. Bandgap Narrowing in Silicon Bipolar Transistors. *IEEE Transactions on Electron Devices*, ED-24(8):1123–1125, 1977.

[31] J.W. Slotboom. The pn-Product in Silicon. *Solid-State Electronics*, 20(4):279–283, April 1977.

[32] L. Onsager. Reciprocal Relations in Irreversible Processes I. *Physical Review*, 37:405–426, 1931.

[33] L. Onsager. Reciprocal Relations in Irreversible Processes II. *Physical Review*, 38:2265–2279, 1931.

[34] S. Rudin, G. Wachutka, and H. Baltes. Thermal effects in magnetic microsensor modeling. *Sensors and Actuators A*, 25-27:731–735, 1991.

[35] G.K. Wachutka. Rigorous Thermodynamic Treatment of Heat Generation and Conduction in Semiconductor Device Modeling. *IEEE Transactions On Computer-Aided Design*, 9(11):1141–1149, 1990.

[36] Python Software Foundation. *Python Language Reference, version 2.7.12*.

[37] P. Rose, D. Silber, A. Porst, and F. Pfirsch. Investigations on the Stability of Dynamic Avalanche in IGBTs. In *Power Semiconductor Devices an IC's*, pages 165–168, 2002.

[38] A. Müller, F. Pfirsch, and D. Silber. Trench IGBT behaviour near to latch-up conditions. In *Proceedings of 17th International Symposium on Power Semiconductor Devices and ICs*, pages 255–258, 2005.

[39] A. Müller-Dauch, F. Pfirsch, M. Pfaffenlehner, and D. Silber. Source Side Thermal Runaway of Trench IGBTs , Dependence on Design Aspects. In *18th International Symposium on Power Semiconductor Devices and ICs*, pages 1–4, 2006.

[40] C. Toechterle, F. Pfirsch, C. Sandow, and G. Wachutka. Analysis of the Latch-up Process and Current Filamentation in High-Voltage Trench-IGBT Cell Arrays. In *Proc. of SISPAD*, pages 296–299, Glasgow (UK), 2013.

[41] C. Toechterle, F. Pfirsch, C. Sandow, and G. Wachutka. Influence of quasi-3D filament geometry on the latch-up threshold of high-voltage trench-IGBTs. In *Proc. of SISPAD*, pages 177 – 180, Nuremberg (GER), 2016.

[42] R. Baburske, F.-J. Niedernostheide, J. Lutz, H.-J. Schulze, E. Falck, and J. G. Bauer. Cathode-Side Current Filaments in High-Voltage Power Diodes Beyond the SOA Limit. *IEEE Transactions on Electron Devices*, 60(7):2308–2317, 2013.

[43] C. Sandow, R. Baburske, V. van Treek, F.-J. Niedernostheide, H.-P. Felsl, and M. Cotorogea. Predictive half-cell simulations of filament formation during IGBT turn-off. In *2015 IEEE 27th International Symposium on Power Semiconductor Devices & IC's (ISPSD)*, pages 97–100, 2015.